# Development of Micro Pixel Chamber and Systematic Study on the Electrode Structure

Tsutomu Nagayoshi

Department of Physics, Faculty of Science, Kyoto University
*Kitashirakawa Oiwake-cho, Sakyo-ku, Kyoto, 606-8502, Japan*
nagayosi@cr.scphys.kyoto-u.ac.jp

This thesis was submitted to the Department of Physics,
Graduate School of Science, Kyoto University
on January 6, 2004
in partial fulfillment of the requirements
for the degree of Doctor of Science in physics.

**Abstract**

We have developed a novel gaseous two-dimensional imaging detector "Micro Pixel Chamber ($\mu$-PIC)" based on Printed Circuit Board (PCB) technology. The problem of gas gain non-uniformity was overcome by a new manufacturing technique. The uniformity of gas gain within 7% was achieved in the whole detection area of $10 \times 10\text{cm}^2$. The maximum gas gain of more then $10^4$ was obtained without any other intermediate gas multipliers. Long term stability of over 1000 hours was also attained with the gas gain of 6000. Further improvement of the electrode structure was investigated based on the three-dimensional simulation using GARFIELD and MAXWELL. Consequently, we found that the gas gain of more than $10^5$ would be expected for a $\mu$-PIC having a 150$\mu$m thick substrate. A fast data acquisition system was also developed for the time-resolved readout. The signals of 512 channels from the $\mu$-PIC are encoded to the position information using Field Programmable Gate Arrays (FPGAs) with a clock of 20 or 40MHz. The data taking rate of 7MHz was attained for real X-ray events. The two-dimensional spatial resolution of 120$\mu$m was achieved using this DAQ system. The proton tracks were successfully detected with the three-dimensional sampling interval of 2.6mm. The tracking resolution of 260$\mu$m was obtained. For the future applications, several foundamental experiments were performed: X-ray polarimetry, X-ray crystallography, MeV gamma-ray imaging, and neutron detection.

# Contents

# List of Figures

# List of Tables

# Chapter 1

# Introduction

Gas detectors are one of the radiation detectors most widely used since the beginning of particle physics. The proportional chamber which consists of a thin anode wire and a cathode tube is a well-known gas detector. It became the basis of all gas detectors such as MultiWire Proportional Chambers (MWPCs), Drift Chambers, or Time Projection Chambers (TPCs). In particular, MWPCs are the first gas detector having two-dimensional position sensitivity and energy spectrometry. Because of the repulsive force between anode wires, the electrode pitch of the MWPCs is restricted to about 1mm. This limit of the wire pitch determines the spatial resolution. The Micro-Pattern Gas Detectors (MPGDs) were proposed in order to exceed the limit of MWPCs.

The history of MPGDs is traced back to the invention of the Micro-Strip Gas Chamber (MSGC) by A. Oed in 1988 [1]. A principle of the operation of an MSGC is same as a conventional proportional gas chamber. The main feature of an MSGC is the structure of the electrodes. Instead of wires in MWPCs, an MSGC has very narrowly spaced electrodes made on a thin substrate. Hence, an MSGC has several excellent features: fine position resolution ($\sim 100\mu$m) and high rate capacity ($\sim 10^6$cps) [2]. Since 1992, we had developed a two-dimensional MSGC and used for X-ray crystallography and solution X-ray scattering experiments [3]. However, there still remained a serious problem of discharges, which caused a critical damages on the electrodes of MSGCs. Because of this problem, the gas gain of an MSGC was restricted to several hundreds. Although MSGC was a quite promising detector for many application, such as high energy experiments,

X-ray crystallography, and X-ray astrophysics, there were only a few examples except neutron imaging experiments [4] that achieved the the practical use of MSGCs.

Until now, many efforts have been made to avoid discharges and to obtain a high gas gain. One solution is a use of an intermediate gas multiplier. The capillary plate [5, 6], the Gas Electron Multiplier (GEM) [7], and the Micromesh Gaseous Structure (MICROMEGAS) [8] are classified to this category. In these detectors, a floating structure is set above the readout electrodes such as an MWPC or an MSGC. Drift electrons are multiplied by the strong electric field applied between the electrodes. Now, GEM and MICROMEGAS are widely studied for various applications, e.g. a Cherenkov light imager [9], a tracking device for a high energy experiment [10], and a dark matter detector [11]. Although the attainable gas gain of single GEM or capillary plate was less than 1000, a high gas gain was obtained by multiple GEMs or capillary plates mounted in the same gas volume. Our group had developed a hybrid MSGC combined with two-step capillary plates [12]. The gas gain of $5 \times 10^3$ was achieved, which was much higher than that of a stand-alone MSGC. A gas gain more than $10^6$ was obtained with the quadruple-GEM detector, which was intended to be applied to a gaseous photomultiplier (gas PMT) [13]. However, these floating electrode structures make detectors too complicated to develop large area detectors.

The other solution to obtain a high gas gain is a use of a pixel type electrode. A very strong electric field is made around the anode electrode, which is rapidly weakened with the distance from the anode. Then the gas gain becomes higher than that of the strip electrode for the same electrode pitch and the same applied voltage. The first gas detector which has a pixel electrode was the Gaseous Pixel Chamber [14]. However, usually this detector is not categorized into micro-pattern detectors, because of its wide electrode pitch ($\sim$1cm). The Micro Dot detector (MDOT) [15] is the first micro-pattern detector which has a pixel electrode structure. Since MDOTs were manufactured using an integral circuit (IC) technology on a silicon wafer, it was difficult to make a large area detector.

The manufacturing technologies of MSGCs and MDOTs were based on IC technology. Therefore, the detection area was restricted within a 10cm square. In order to extend the detection area, an alternative manufacturing technique was required. That is the Printed Circuit Board (PCB) technology, which provides us mechanical robustness as well as the

large detection area. Several types of MPGDs have been developed based on the PCB technology, e.g. the Micro-Groove detector [16], the Micro-Well detector [17, 18], the Micro-Wire detector [19] etc. The manufacturing technologies of these detectors are the same as GEM. The signal was read out by strip electrodes, then the achieved gas gain was several thousands. The structure and manufacturing technologies for these detectors are summarized in Table 1.1.

| Name | Electrode | Technology | Electrode pitch | thickness |
|---|---|---|---|---|
| MSGC | Strip | IC | 200$\mu$m | 20$\mu$m |
| GEM | Mesh | PCB | 140$\mu$m* | 50$\mu$m |
| MICROMEGAS | Mesh | Electroforming | 25$\mu$m* | 3$\mu$m |
| MDOT | Pixel | IC | 200$\mu$m | 5$\mu$m |
| Micro-Groove | Strip | PCB | 200$\mu$m | 50$\mu$m |
| Micro-Well | Strip | PCB | 120$\mu$m | 50$\mu$m |
| Micro-Wire | Strip | PCB | 100$\mu$m | 50$\mu$m |
| $\mu$-PIC | Pixel | PCB | 400$\mu$m | 100$\mu$m |

* Pitch of the mesh.

Table 1.1: Summary of the Micro-Pattern Gas Detectors.

The Micro Pixel Chamber ($\mu$-PIC) is one of the Micro-Pattern gas detectors which has a pixel electrode structure. We have developed the $\mu$-PIC using PCB technology. The electrode structure of the $\mu$-PIC is similar to the MDOT detector; pixel anodes are surrounded by the cathode rings. However, the manufacturing process is quite different. At first, a $\mu$-PIC has a thick substrate of 100$\mu$m, which is an essential point to ensure the higher gas gain. In addition, the PCB technology allows us to have a large detection area up to $30 \times 30\text{cm}^2$. Our $\mu$-PIC has following features:

1. pixel electrodes,
2. large detection area,
3. thicker substrate than MDOT detectors,

4. robustness against discharges,

5. mass productivity.

At first, we made a prototype of the $\mu$-PIC having the detection area of $3 \times 3\text{cm}^2$ [20, 21, 22] in 1999. Now, large area $\mu$-PICs with the detection area of $10 \times 10\text{cm}^2$ become available through several improvements both of the manufacturing process and the electrode structure. The $\mu$-PIC with a detection area of $30 \times 30\text{cm}^2$ is now being developed.

In general, MPGDs have a capability of high counting rate up to $10^6$cps. In order to obtain the performance effectively, a multi-channel digital readout electronics with fast operation speed is preferred. The former data acquisition (DAQ) system was developed based on this concept for the two-dimensional MSGC [2] which has 1024 readout electrodes. This DAQ system consisted of 16 amplifier-discriminator boards, 4 position encoding modules, and a memory module. Event-by-event position encoding became possible by a pipeline processing method. The basic concept of the new DAQ system for $\mu$-PICs is similar to that for MSGCs. Hence, it consists of amplifier-discriminator boards, position encoding module, and memory module. In contrast to the DAQ of MSGCs, the position encoding was processed in one board with a system clock of several ten MHz. A simple DAQ system was realized by Field Programmable Gate Arrays (FPGAs). The data acquisition logic is suitably rewritable for various purposes.

There are many applications of the $\mu$-PIC. In X-ray imaging, X-ray crystallography, solution scattering, and X-ray polarimetry are major applications of $\mu$-PIC. A Time Projection Chamber for charged particle tracking with fine position resolution based on $\mu$-PIC, which is named "$\mu$-TPC", is another application. The $\mu$-TPC is a promising detector for gamma-ray imaging using tracks of recoil electrons due to Compton scattering, thermal neutron imaging, and dark matter search experiments.

Especially for gamma-ray imaging, the $\mu$-TPC needs to detect minimum ionizing particles such as electrons of sub-MeV energy region. Hence, the required gas gain for a $\mu$-TPC is more than $10^4$. In order to realize a high gas gain and stability simultaneously, the electrode structure have to be improved. The optimization of the electrode structure of $\mu$-PIC have been carried out via a computer simulation.

In this thesis, I describe the development of $\mu$-PICs, the optimization of the electrode structure, the data acquisition system, and several applications of the $\mu$-PIC. In chap-

ter 2 and 3, the principle of operation and basic concept of MPGDs are described. The manufacture of $\mu$-PICs and the electrode structure is presented in chapter 4. The DAQ system of $\mu$-PIC and its performance is described in chapter 5. In chapter 6, I present the basic performances of the $\mu$-PIC. Chapter 7 is devoted to the attempt for the optimization of the electrode structure. In chapter 8 X-ray and charged particle imaging properties are discussed. Several preliminary experiments for applications of $\mu$-PIC are presented in chapter 9. Finally, I present the summary and conclusion in chapter 10.

# Chapter 2

# Physical process of gas multiplication in $\mu$-PIC

In principle, the operation process of the $\mu$-PIC is same as that of a proportional wire chamber. In this chapter, the physical process of gas multiplication is described.

## 2.1 Drift and diffusion of primary electrons in gas

When a charged particle passes through the gas volume, it loses the kinetic energy by the Coulomb interaction with the electrons of the gas atoms. Then electron and ion pairs are released along the path of the incident charged particle. The cluster of an electron-ion pair is called a "electron cloud". The energy loss per unit length ($\mathrm{d}E/\mathrm{d}x$) is an intrinsic value for a gas and also a function of the energy of the incident particle. When the kinetic energy of the incident particle is similar to or over the mass of the particle, $\mathrm{d}E/\mathrm{d}x$ becomes minimum of typically several keV/cm in atmospheric pressure. The length $x$ is often replaced with the column density which is a product of length and density in order to deal the energy loss independently of the medium. In this term, the energy loss is expressed in the unit of $\mathrm{MeV}/(\mathrm{g}\cdot\mathrm{cm}^2)$. Fig. 2.1 shows the energy loss of various particles in the unit of $\mathrm{MeV}/(\mathrm{g}\cdot\mathrm{cm}^2)$. The minimum energy loss is roughly the equal value for many particles with the unit charge. Then the charged particles of which energy exceeds the mass of the particle are called "Minimum Ionizing Particles (MIPs)".

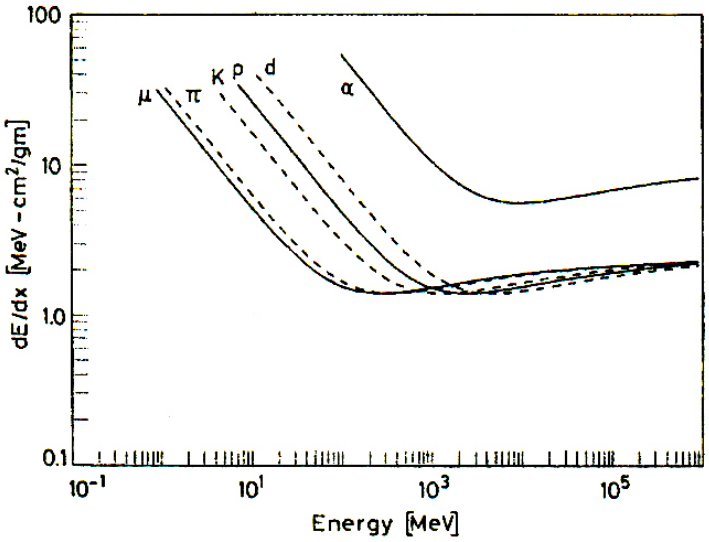


Figure 2.1: Energy loss of various particles in MeV/(g · cm$^2$) [23].

The total number of electron-ion pairs $n_{\mathrm{T}}$ released by a charged particle is

$$n_{\mathrm{T}} = \frac{\Delta E}{W}, \tag{2.1}$$

where $\Delta E$ is the total energy loss in the gas volume, and $W$ is the average energy to produce one electron-ion pair, or "W-value". The W-value is typically 20-30eV. On the other hand, photons such as X-rays or gamma-rays interact with a gas atom via a photoelectric absorption, a Compton scattering, or a pair production, and emit the primary electrons, which also ionize gas atoms and release electron cloud as the following equation (2.1).

A generated electron cloud is drifted toward the anode electrode in an electric field applied in the gas volume while a cluster of positive ions moves to the drift electrode. The drift velocity of ions $w$ is proportional to the strength of the electric field $E$ and inversely proportional to the gas pressure $p$, i.e. $w = \mu E(p_0/p)$, where $p_0$ means the atmospheric pressure (760Torr). The constant parameter $\mu$ is called "mobility" of ions, which is intrinsic to each gas. The value of $\mu$ for argon gas is 1.7cm$^2$/(s · V). The dependences of $w$ on $E$ and $p$ can be represented by the reduced parameter $E/p$ which is called "reduced electric field".

On the other hand, the drift velocity of electrons can not be expressed as a simple function like that of ions. Therefore experimental data (e.g. Ref. [24]) or results of a simulation is used. The drift velocity of electron is experimentally known to be order of 1cm/$\mu$s, which is 1000 times faster than that of ions of $\sim$ 1cm/ms. In general, the drift velocity of electrons increases in proportional to the reduced electric field $E/p$ while the electric field is not so strong ($\lesssim$500V/cm). In a strong electric field, the drift velocity is almost saturated (see Fig. 2.5).

During the drift in the gas, the cluster of electrons or ions is gradually diffused due to the multiple scattering. The diffusion of electrons along a given direction $x$ is described by Gaussian distribution. Usually, the scale of the diffusion is described as the standard deviation at 1cm drift length. A typical size of the diffusion becomes the order of 100$\mu$m. In an X-ray imaging detector having a drift length of a few mm, the diffusion is several tens $\mu$m.

The examples of electron drift and diffusion in individual gas are described in the later section (Sec. 2.3).

## 2.2 Gas multiplication

The main process of gas detectors is a gas multiplication of an electron in the strong electric field around the anode. This process is theoretically explained based on Townsend theory. Here, the gas multiplication in a proportional wire chamber (Fig. 2.2) is explained, because the physical process is the same as the $\mu$-PIC.

At first, primary electrons produced by an incident particle in the gas volume are forced by the applied electric field in the chamber. In the moderate electric field of $\sim$1kV/cm in the drift region, the primary energy of the drifting electrons in the cloud is immediately lost by collisions with the gas atoms, and drifted toward the anode electrodes without any additional ionization. A small amount of electrons are lost by recombination or attachment. When a low energy electrons collides with a positive ion, the electron is sometimes combined with the ion. This is called "recombination", which appears in extremely weak electric field ($\ll$ 100V/cm). If an electron is captured by a neutral atom, the electron and atom form a negative ion. This phenomena is called "attachment". In

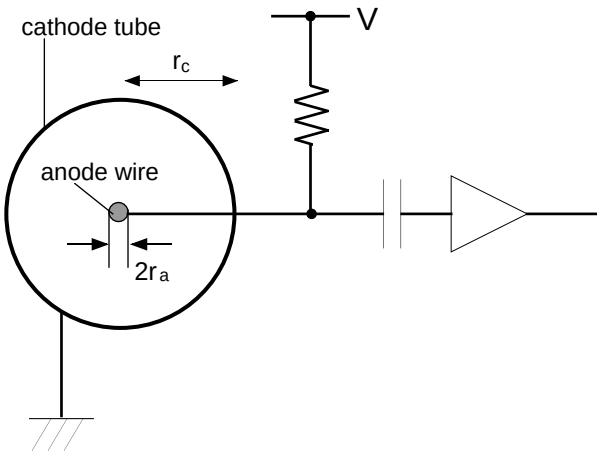


Figure 2.2: Schematic drawing of a proportional chamber.

the noble gas this effect is almost negligible.

The electric field near the anode electrode increases in proportional to $1/r$, where $r$ is the distance from the center of the anode. Then as an electron goes near the anode electrode, the energy of an electron increases. When the energy exceeds the first ionization potential of the gas, the secondary ionization are occurred. These secondary electrons are accelerated again, and they ionize gas atoms one after another. Hence, the number of the secondary electron exponentially increases in the proximity of the anode electrode, which is called an electron avalanche. If $\lambda$ is the mean free path of an electron for the secondary ionization, the number of ionization through the unit path of an electron is expressed as $\alpha = 1/\lambda$. This $\alpha$ is the first ionization coefficient or the *first Townsend coefficient*. Consequently, the number of the total electron $n$ after the path length of $x$ becomes

$$n = n_0 \exp(\alpha x), \tag{2.2}$$

where $n_0$ is the initial number of the primary electrons. The number of the total electron rapidly increases. Thus the $\alpha$ is an intrinsic value to the gas, and depends on the electric field strength. Since the electric field depends on the position, $\alpha$ is also a function of the path length of an electron. Therefore, the multiplication factor $M$ of a detector is expected as an exponentiated integral of the first Townsend coefficient along the drift

path,

$$M = \frac{n}{n_0} = \exp\left(\int \alpha \, \mathrm{d}x\right). \tag{2.3}$$

$M$ depends on the strength of the electric field through the dependence of $\alpha$. Therefore, $M$ is a function of the applied voltage through the dependence of $\alpha$ on the electric field. Here, this multiplication factor does not include the losses of the electrons during the electron drift via attachment or recombination. On the other hand, the measured gas gain is experimentally calculated using the charge collected by the anode electrode. Suppose the energy deposit $\Delta E$ of the incident particle is known, the measured gas gain $M_{\mathrm{eff}}$ is expressed as:

$$M_{\mathrm{eff}} = \frac{\textit{collected charge}}{\textit{released charge}} = \frac{Q_{\mathrm{col}}}{(\Delta E/W) \cdot e}, \tag{2.4}$$

where $Q_{\mathrm{col}}$, $W$, and $e$ are the collected charge, W-value of gas, and the elementary charge (charge of an electron), respectively. Sometimes, some fraction of the electrons are lost due to the recombination or other factors, and hence the measured multiplication factor is smaller than the absolute multiplication factor defined as the equation (2.3). Hence, we define the electron collection efficiency as follows:

$$R_{\mathrm{eff}} = N_{\mathrm{col}}/N_{\mathrm{tot}}, \tag{2.5}$$

where $N_{\mathrm{col}}$ is the number of primary electrons collected by the anode, $N_{\mathrm{tot}}$ is the total number of primary electrons. The measured multiplication factor $M_{\mathrm{eff}}$ can be also written using the electron collection efficiency $R_{\mathrm{eff}}$ as follows:

$$M_{\mathrm{eff}} = R_{\mathrm{eff}} M. \tag{2.6}$$

Note that the measured multiplication factor is not the *absolute* multiplication factor defined by the equation (2.3), but the *measured* multiplication factor expressed by the equation (2.4). Hereafter, we express the absolute multiplication factor as $M_{\mathrm{abs}}$ instead of $M$. Actually, in classical wire chambers, most primary electrons are collected by the anode electrodes, then the measured and the absolute multiplication factors become the same value. However, a wireless chamber such as an MSGC has a complicated structure, and some electrons attach on the detector structure other than the anode electrodes. In this case, the degradation of multiplication factor due to this electron loss can not be neglected.

In the multiplication process, large number of positive ions are generated. When these ions return to the neutral state via recombination, a photon of UV energy region (∼10eV) is emitted. Once the UV photon irradiates the electrode material, secondary electron(s) are emitted via the photoelectric effect. This secondary electrons are also multiplied near the anode electrodes. If the average number of the secondary electrons due to a positive ion exceed 1, this process occurs endlessly and causes discharges. In order to suppress this effect, some additional gases which absorb the UV photons are mixed with the base gas. Organic gases such as methane or ethane is normally used as the additional gas, which is called "quenching gas" or "quencher". These organic gases absorb the UV photons and change the energy into the rotation or vibration of the molecule.

## 2.3 Gases for detectors

The behaviors of incident photons and incident charged particles in a detector depends on the physical properties of the gas. The gas in a detector has to be suitably selected taking into account of various purposes such as X-ray detection or charged particle tracking.

### X-ray imaging

Noble gases such as argon and xenon are frequently used in gas detectors, because they have no electronegativity. In an electronegative gas such as oxygen, the electrons released by the incident particle are immediately captured by the electronegative gas. For X-ray detectors, a gas having a short absorption length of photon is required. As is well known, the cross section of photoelectric absorption is approximately proportional to $Z^5$ and $E^{7/2}$, where $Z$ is an atomic number of the material, and $E$ is the energy of an incident photon, when photon energies are greater than the energy level of the K-absorption edge and less than the electron mass. Absorption lengths of photon in typical gases are shown in Fig. 2.3 [25]. Argon is a useful gas for easy handling and its low cost. Because of its high $Z$, xenon gas is the most suitable gas for this purpose. As well as its high efficiency, xenon gas has another advantage of the short range for photoelectrons emitted from the Xe atoms. Therefore, a fine spatial resolution is obtained. Although krypton is a one of noble gases, it is rarely used for detectors, because it contains the radioactive isotope,

$^{85}$Kr which emits beta-ray of the maximum energy of 687keV.

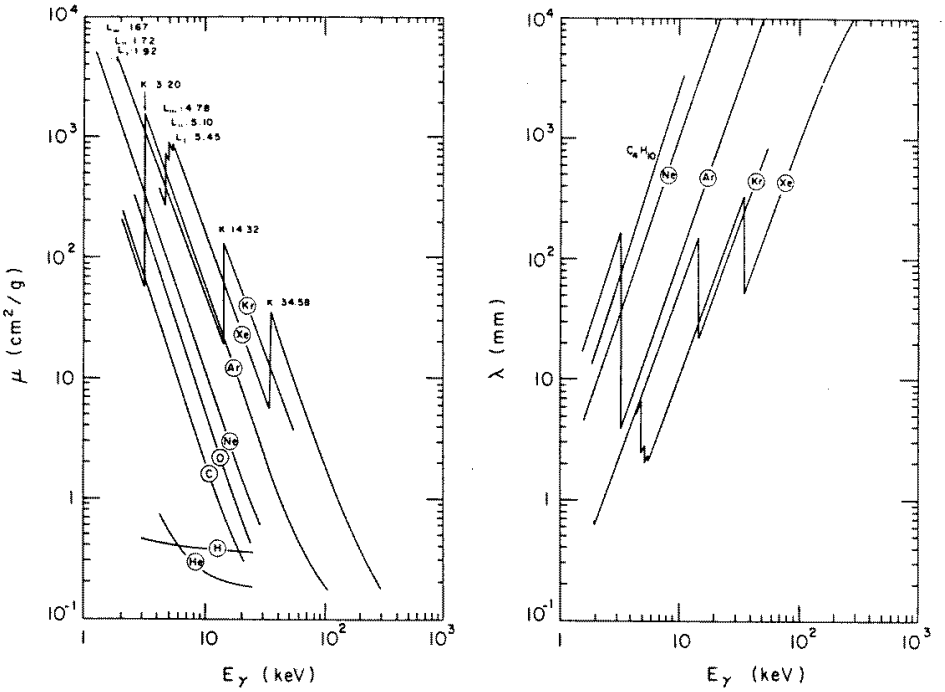


Figure 2.3: Cross sections of photoelectric effect (left) and mean free path (right) [25].

### Charged particle tracking

When we design a tracking detector for charged particles, deflection of the tracks due to multiple scattering have to be minimized. While electrons or other charged particles pass through matter, the incident charged particles are repeatedly scattered by nuclei of the matter. The physical process is expressed as Molière theory [26]. The deflection angle of the track is associated with the each atom which composite a molecule. In concrete, the root mean square of the deflection angle is expressed using a radiation length $X_0$ as follows [27] (see also Fig. 2.4):

$$\theta = \frac{13.6\,\mathrm{MeV}}{\beta cp}\, z \sqrt{\frac{x}{X_0}} \left(1 + 0.038\, \ln\!\left(\frac{x}{X_0}\right)\right), \tag{2.7}$$

where $p$, $\beta c$, and $z$ are momentum, velocity, and charge number of the incident particle, and $x$ means the thickness of the scattering medium. The gases which consist of heavy

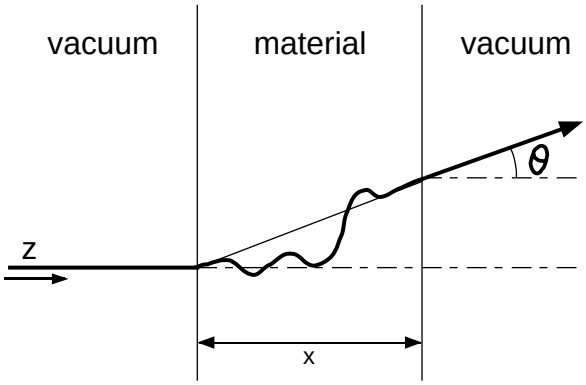


Figure 2.4: Schematic drawing of the multiple scattering.

atoms have small radiation length. The probability distribution of the scattering angle is approximated by a Gaussian function. Then the average angle is proportional to $Z$ of the medium. Since the incident particle undergoes large scattering in heavy gas such as xenon, light gases such as methane or ethane is more suitable than noble gases for particle tracking.

**Gamma-ray detection**

In the detection of the gamma-rays in the MeV energy region, the Compton scattering is the dominant interaction with a matter. Compton scattering is an elastic scattering between a photon and an free electron. The cross section of Compton scattering is proportional to the atomic number $Z$ which indicate the number of electrons bound in an atom. Therefore, large cross section is obtained for heavy gas such as xenon. However, for low energy gamma-ray ($\lesssim$ 100keV), the energy of scattered gamma-ray is broadened by Doppler shift in heavy gas. Additionally, the tracks of the recoil electron tend to be straggled in heavy gas such as xenon. Thus it is difficult to measure the direction of the recoil electron, although this is a key technique for the gamma-ray imaging as described in chapter 9. On the other hand, since the Compton scattering is an interaction of a free electron, the cross section is a function of only the *number of electrons*. That is

independent to whether the electron is bound in an atom or in a molecule. Therefore, following expression is also possible; the cross section is proportional to the number of electrons bound in an atom or a molecule. In the carbon tetrafluoride ($CF_4$), which has 42 electrons in a molecule, a large cross section is expected for Compton scattering. The cross section of photoelectric absorption depends on the atomic number of each atom which composites a molecule. Therefore, the boundary energy region that the dominant interaction changes from photoelectric absorption to Compton scattering is dependent on the gas. The boundary energy for Ar and Xe are about 100keV and 300keV, respectively. In contrast, since the atomic numbers of carbon and fluorine are less than that of argon or xenon, the quantum efficiency for photoelectric absorption is quite low. Thus, for $CF_4$ gas, Compton scattering is a dominant interaction even in low energy ($< 100$keV) gamma-ray. Furthermore, small deflection of the track is expected, because multiple scattering is small for the gas composed by light atoms. In addition, $CF_4$ has an advantage of the larger energy loss per unit length ($\mathrm{d}E/\mathrm{d}x$). The dE/dx for minimum ionizing particles (MIPs) of $CF_4$ is 7keV/cm which is about three times as high as that of argon. These physical properties are summarized in Table. 2.1 [29]. In this table, the numbers of electron in molecules are also expressed as $Z$ which is the same symbol as the atomic number.

| Gas | Z | Density $[10^{-3}\mathrm{g/cm^2}]$ | W [eV] | $(\mathrm{dE/dx})_{\mathrm{MIP}}$ [keV/cm] | Radiation length [m] |
|---|---|---|---|---|---|
| Ar | 18 | 1.78 | 26 | 2.44 | 110 |
| Xe | 54 | 5.86 | 22 | 6.76 | 15 |
| $C_2H_6$ | 18 | 1.34 | 27 | 1.15 | 340 |
| $CO_2$ | 22 | 1.98 | 33 | 3.01 | 183 |
| $CF_4$ | 42 | 3.93 | 54 | 7 | 92.4 |

Table 2.1: Physical Properties of gases at 20°C and 760 Torr [29].

**Electrons in the gases**

The drift velocity of electrons, the diffusion of an electron cluster, and the first Townsend coefficient are also important parameters which determine the performance of the gas

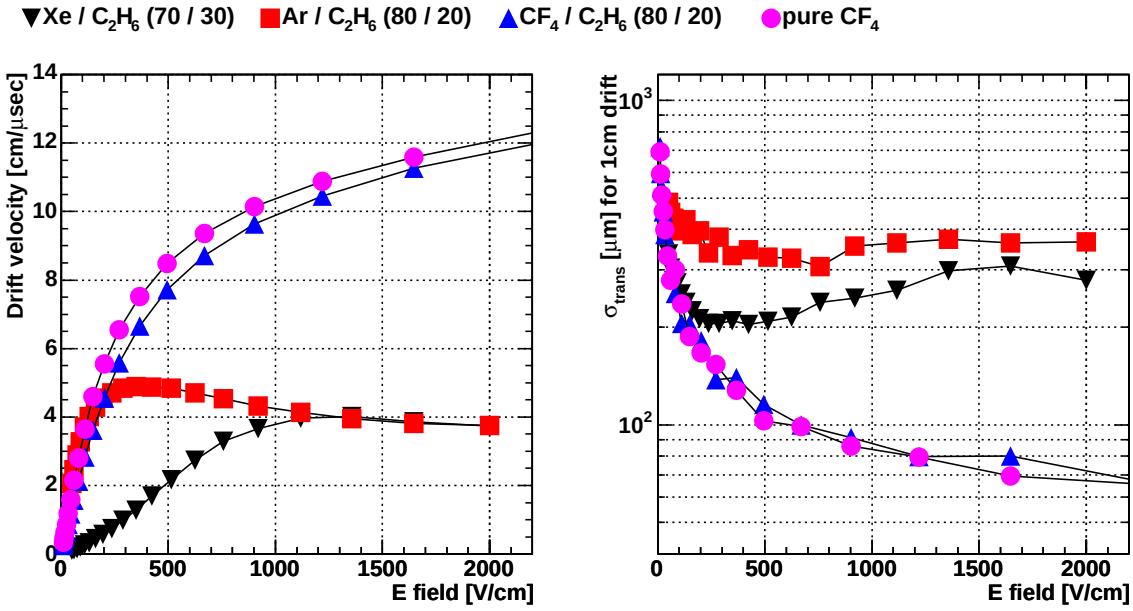


Figure 2.5: Drift velocities (left) and transverse diffusions (right) of electrons in each gas. Diffusion is defined as a standard deviation [$\mu$m] for 1cm drift.

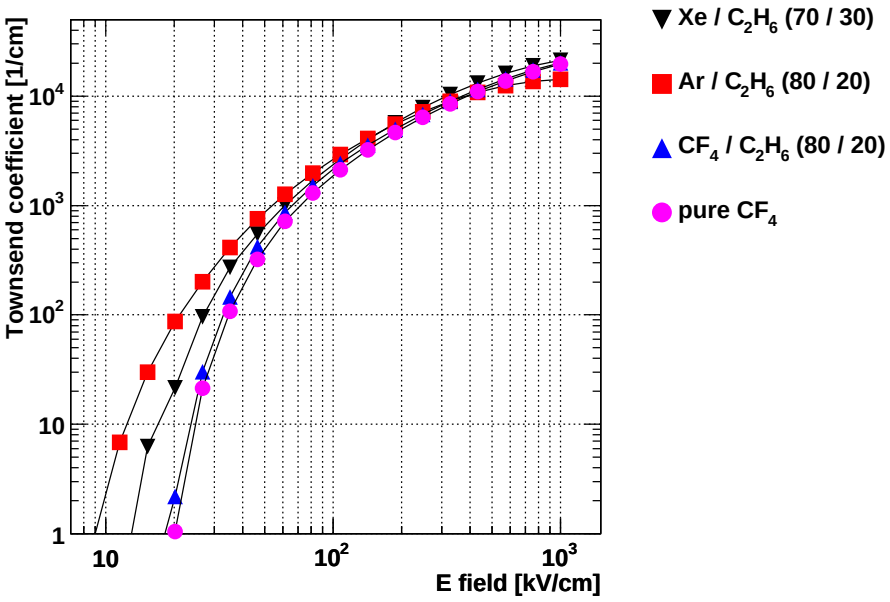


Figure 2.6: The first Townsend coefficients in each gases.

detector. In particular, the drift velocity and the diffusion are key factors for the performances of Time Projection Chambers (TPCs). These parameters are intrinsic to the gases, and are expressed as functions of the reduced electric field $E/p$. However, it is not easy to express these parameters as a simple function. Usually, experimental data or results of simulation are used to describe these parameters. As a simulation tool, the MAGBOLTZ computer program [28] is widely used. The MAGBOLTZ solves the Boltzmann transport equations for electrons in gas mixture under the influence of a electromagnetic field. Figs. 2.5 and 2.6 show the calculated drift velocity of electrons, diffusion of electrons, and the Townsend coefficients of some gases which are often used in gas detectors. In these figures, properties of pure $CF_4$ and $CF_4/C_2H_6$ (80/20), $Ar/C_2H_6$ (80/20), and $Xe/C_2H_6$ (70/30) gas mixtures are shown.

### Short summary

As the results, these gases has following properties:

**Ar-based gas** High gas gain at the low voltage is expected. The spatial resolution and

detection efficiency is not good for high energy X-rays. This gas is suitable for basic operation test of detectors because of its low cost. Also argon is a useful gas for particle tracking detectors.

**Xe-based gas** High detection efficiency for X-ray is obtained. The fine spatial resolution is expected. This gas is suitable for X-ray area detectors, disregarding its high cost.

**$CF_4$-based gas** Small multiple scattering and small diffusion is expected. Because of these properties and its large dE/dx, this gas is suitable for particle tracking detectors.

# Chapter 3

# Micro-pattern gas detectors

The Micro Pixel Chamber is one of the Micro-pattern gas detectors (MPGDs). Before the discussion of our detector, we review several Micro-pattern detectors developed prior to the Micro Pixel Chamber.

## 3.1 MicroStrip Gas Chamber

MultiWire Proportional Chambers (MWPCs) developed in 1968 [30] are commonly used as large area imaging detectors (Fig. 3.1). In principle, the spatial resolution of MWPCs is determined by the pitch of the anode wires. However a wire spacing is limited to about 0.5mm due to the repulsive force among the wires.

In the avalanche process, the same number of positive ions as that of the electrons are generated around the anodes. These ions are drifted toward the drift electrodes. If an electric field of 1kV/cm is applied in a 1cm thick drift space, the drift time of the positive ions from the avalanche to the drift electrodes is about 0.6msec in argon gas. During this time, the electric field in the chamber is distorted and hence the gas gain become lower, because the electric field is distorted by the space charge due to the positive ions, which is called space charge effect. Thus the rate capability is determined by the drift time of the positive ions; it becomes about $10^{3-4}$counts/sec $\cdot$ mm$^2$.

The Micro-Pattern Gas Detectors (MPGDs) such as MicroStrip Gas Chambers (MSGCs) were developed to overcome these limits of MWPCs. The MSGC was introduced

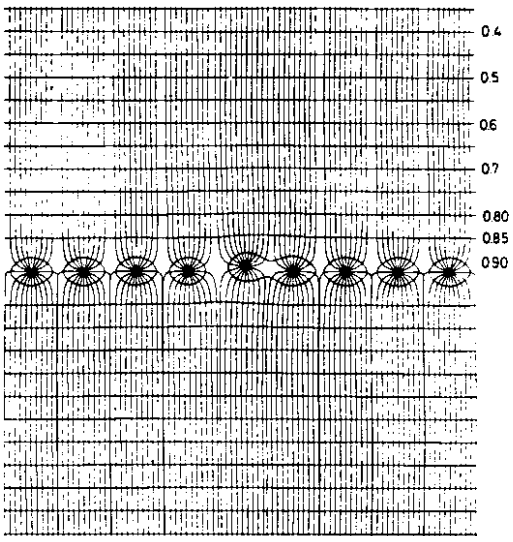


Figure 3.1: Structure of a MWPC and its electric field [25].

by Oed in 1988 [1]. The schematic structure of the MSGC developed by our group is shown in Fig. 3.2. In MSGCs, a narrow spacing of the electrode ($< 500\mu$m) was achieved using alternately arranged anode and cathode strips printed on a insulating substrate instead of wires of MWPCs. This micro structure was realized using a modern lithography technology. Because of the fine electrode pitch, the spatial resolution of below $100\mu$m was easily achieved. Furthermore, less positive ions from an avalanche return to the drift electrode than that of MWPCs, because they are immediately ($\lesssim 1\mu$sec) collected by the cathode strips placed near the anode strips. Thus the achieved capability for high counting rate was up to $10^{6-7}$counts/s $\cdot$ mm$^2$, which is more than 1000 times higher than that of MWPCs.

Because of these advantages, MSGCs were expected to be a good candidate for high intensity beam such as synchrotron radiation facilities or future high energy experiment. Our group had developed two-dimensional MSGCs (2D-MSGCs) with a thin ($20\mu$m) polyimide substrate [2] (see Fig. 3.2). The 2D-MSGC has following features: (1) fine position resolution of $< 100\mu$m, (2) rate capability for incident X-ray of $10^7$cps/mm$^2$, and (3) fine timing resolution of $<$ 100nsec. These features were utilized for rapid X-ray crystal analysis and small angle X-ray scattering (SAXS) experiments of protein solutions [3].

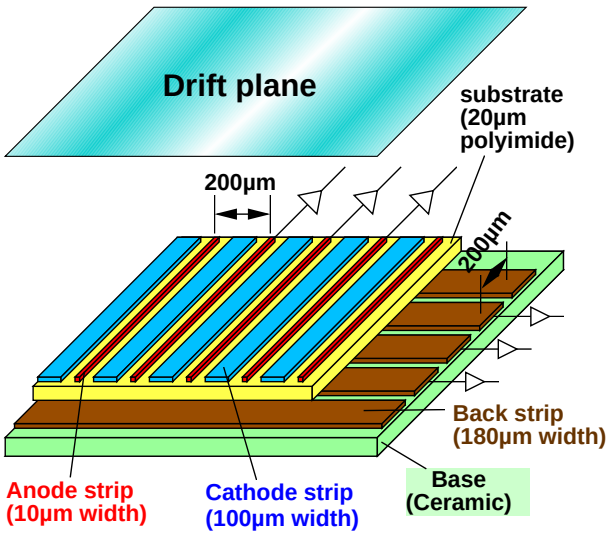


Figure 3.2: Schematic structure of MSGC.

However, MSGCs have some serious problems. For two-dimensional readout, 2D-MSGC has additional electrodes on the rear side of the thin substrate. These back electrode affect the electric field of the drift region. More specifically, positive ions produced in an avalanche are attracted by the back electrode, and attached on the substrate. The attached ions weaken the electric field near the anode strips. Consequently the gas gain decrease within a few minutes. In order to avoid this problem, the surface of the substrate was covered by a thin layer of organic titanium. By this process, the substrate had slight conductivity of $10^{12}\Omega$. The charging-up of positive ions was removed by the conductivity.

Another and more serious problem was the breakdown of electrodes by the discharges, which caused critical damage to the detectors. Although the mechanism of the discharge will be discussed in Sec. 4.4, they are attributed to the strong electrode near the cathode edge. The discharge probability become critical when the gas gain is higher than 1000. This is the limit of the gas gain for MSGCs.

These problem prevented the practical use of MSGCs. In the practical use, it is necessary to operate detectors in harsh environment. In order to operate stably, the MPGDs of the next generation need to possess robustness against discharges and suitable electrode structure to avoid charging-up of positive ions. Additionally, the mass production of a

large area detector is an important factor for a practical use. The Micro Pixel Chamber have been developed to satisfy these demands.

## 3.2 Intermediate gas multipliers

The gas gain of the MSGC was restricted to 1000 due to discharges. This gain is not high enough to obtain significant S/N for various experiments. One solution to overcome this problem is the use of a intermediate gas multiplier. If primary electrons were multiplied before reaching the MSGC, significant amount of charge can be obtained by MSGC with a low gas gain.

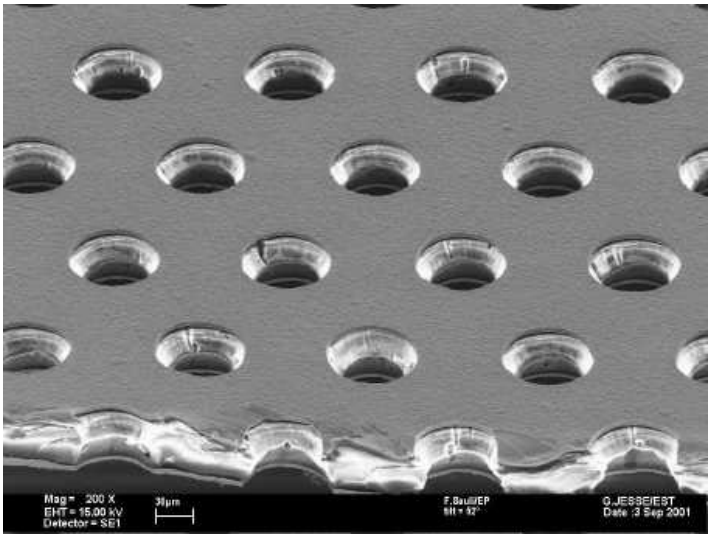


Figure 3.3: Microscopic photograph of the GEM [31].

**Gas Electron Multiplier** A representative detector based on this concept is the Gas Electron Multiplier (GEM) developed by F. Sauli [7]. The GEM consists of a 50$\mu$m thick copper-clad polyimide foil with high density (typically 140$\mu$m pitch) holes. The microscopic photograph is shown in Fig. 3.3. Since the GEM is manufactured using Printed Circuit Board technology, mass production is realized at low cost. High voltage is applied between both sides of the GEM. Primary electrons are multiplied in the strong

electric field formed in each hole. When a GEM is operated at a gas gain of about 100, significant signal is obtained by an MSGC with low gas gain ($\sim 100$). Then total gas gain can exceed 10000 [32].

Although the attainable gas gain of single GEM is limited to several hundred, a higher gas gain over $10^6$ can be obtained by combination of multiple GEMs. Even one electron is detectable by the multiple-GEM detector, which is used as a position sensitive gaseous PMT for UV and visible photon imaging [9, 13].

**Capillary plate** The gas multiplication in the capillary plate was confirmed by Sakurai [33]. It consists of a bundle of fine glass capillaries with electrodes on both the inlet and the outlet as shown in Fig. 3.4. Electrons are multiplied in the electric field applied in each hole. In our group, the capillary plate having the detection area of $95 \times 95\text{mm}^2$ was used as a intermediate gas multiplier for the MSGC. Fig. 3.5 shows the schematic structure of the hybrid system of an MSGC and a capillary plate [5, 6]. The high gas gains more than $10^3$ is achieved by the combination of the MSGC and the capillary plate, where gas multiplication in each step is less than 100. The multiple capillary plates combined with an MSGC was also developed. The gas gain of $5 \times 10^3$ was achieved [12].

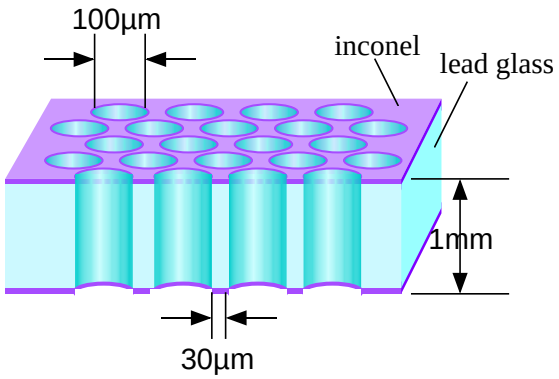


Figure 3.4: Schematic view of a capillary plate.

A common feature of intermediate gas multiplier such as GEM or capillary plate is that they suppress discharges by the reduction of gas gains of each multiplier. There remains some risk of discharges for the intermediate gas multiplier. Additionally, these floating

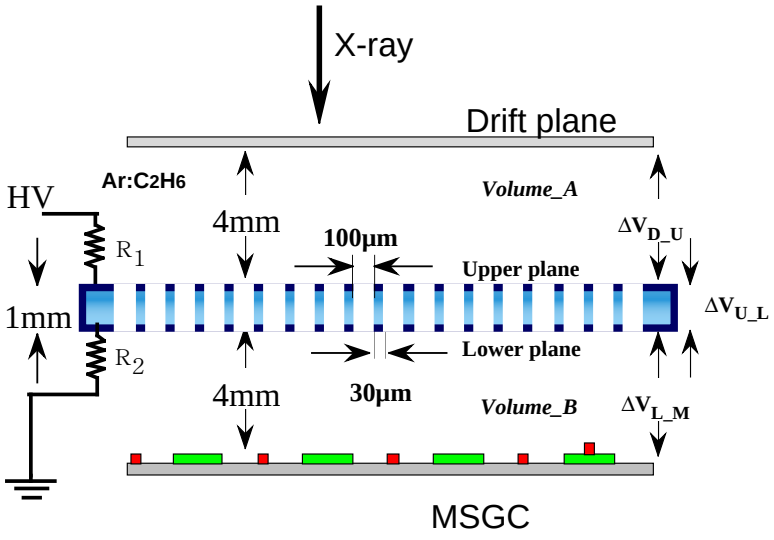


Figure 3.5: Capillary-MSGC combined system.

structures make the detector complicated to develop a large area detector. Therefore, a detector with simple structure and high attainable gas gain is required for a large area gaseous detector.

## 3.3 Pixel electrodes

One solution to obtain high gas gain is to use a pixel shaped electrode. The concentration of electric field lines on a pixel electrode is denser than that of a strip electrode for a certain voltage. Then a high gas gain is expected for a pixel detector.

The MicroDot (MDOT) detector is the first micro-pattern detector having the pixel type anodes [15]. A schematic structure and a cross-sectional view of the MDOT is shown in Fig. 3.6. The MDOT detector is manufactured on a silicon wafer based on the integral circuit (IC) technology. Anode readout buses are buried in a $5\mu$m thick $SiO_2$ layer, and pixel anode is formed through the insulator layer. The gas gain of more than $10^4$ is reported for stand-alone MDOT detector [34].

Since the depth of anode readout buses is only $2\mu$m, the electric field of the avalanche region is strongly distorted by the readout buses. This may cause a degradation of gas

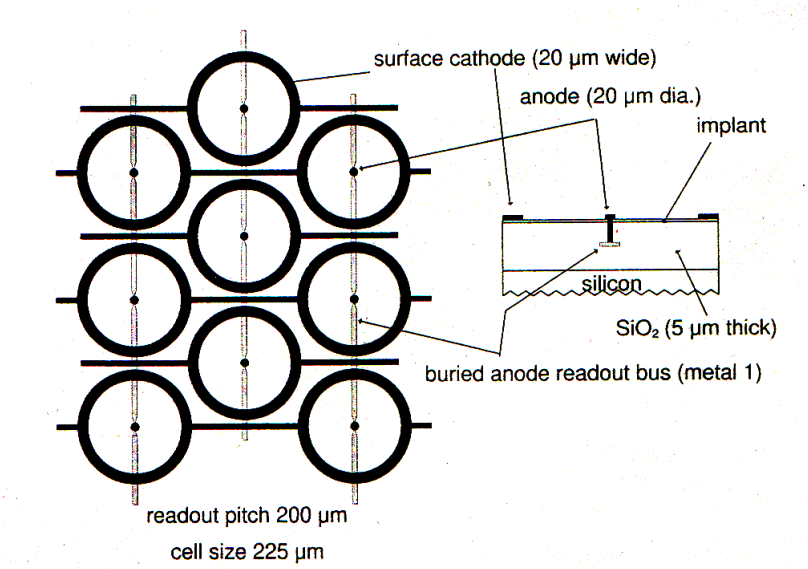


Figure 3.6: Structure of MDOT detector [15].

gain. The relation between the gas gain and the substrate thickness is discussed in later chapter. Additionally, the manufacturing technology for MDOT is difficult to apply for a large area detector. Large area MDOT detectors have not yet reported.

## 3.4 New manufacturing technique

In order to make a large area detector, the Printed Circuit Board (PCB) technology is preferred rather than the IC technology. A detector manufactured by the PCB technology have following features of expandability for a large area detector and mechanical robustness. As well as GEM, various type of detectors have been developed in the late 1990s, for example, Micro-Groove Detector (MGD), WELL detector, and Micro-Wire detector. Basically, above new detectors have the structure similar to a GEM. That is a 50$\mu$m thick metal-clad polyimide foil and regularly formed electrodes. These structures are schematically shown in Figs 3.7. An electric field is applied between the upper metal (cathode) and the lower metal (anode). Primary electrons are multiplied in the gap between the two metal layer similar to a GEM. The multiplied electrons are collected by planar anode

electrodes.

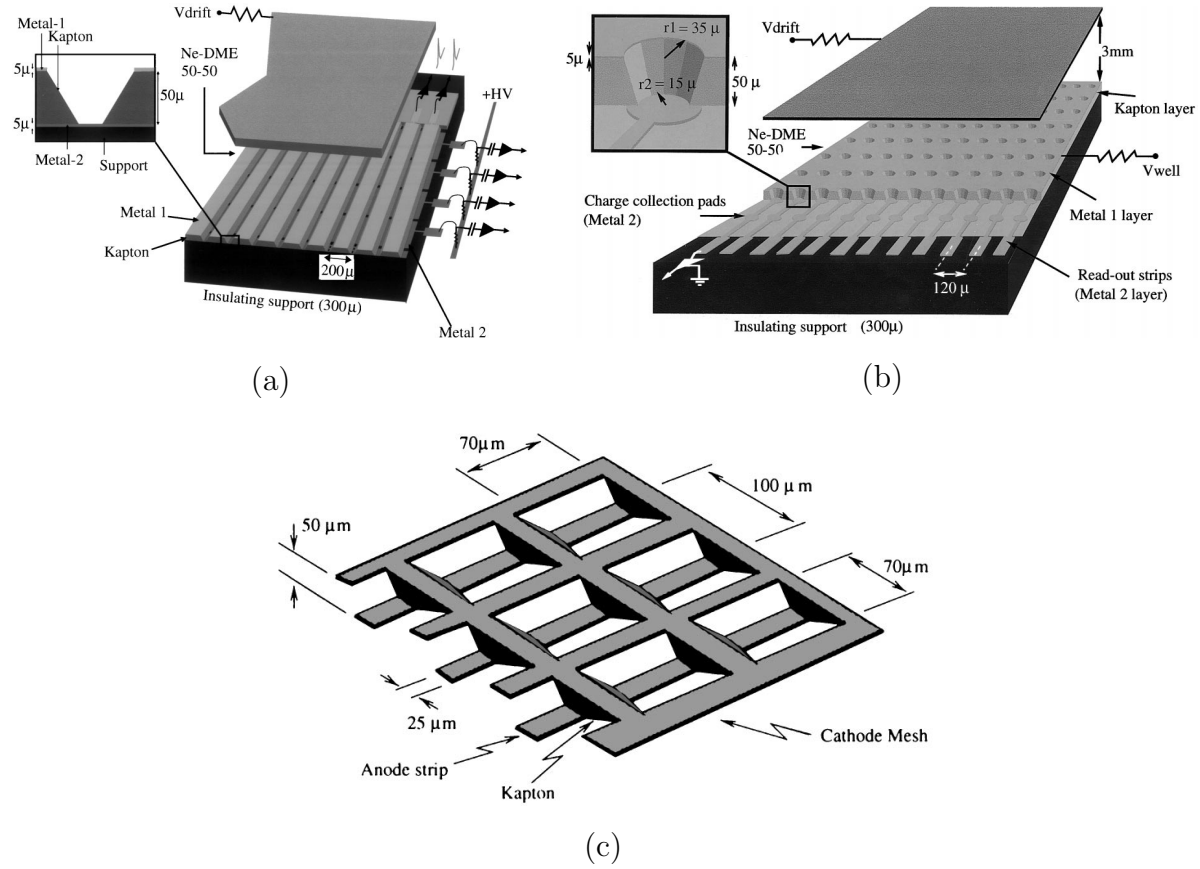


Figure 3.7: Schematic structures of several types of MPGDs. (a) Micro-Groove Detector [16], (b) WELL detector [17], and (c) Micro-Wire detector [19].

Although the gas gains of more than $10^4$ are obtained for these detectors, they are likely to be used as a readout device for a combined detector system with the GEM. For this use, a gas gain of the readout detector is not so high ($\lesssim 10^3$), then discharge is avoided.

The Micro Pixel Chamber is a new gaseous imaging detector which has the features of the pixel type detectors and PCB-based detectors.

# Chapter 4

# Development of the Micro Pixel Chamber

## 4.1 Electrode structure

Fig. 4.1 shows a schematic structure of the $\mu$-PIC. This detector is made using a double-sided printed circuit board (PCB) technology. Anode and cathode strips are orthogonally arranged on both sides of the insulating substrate with a thickness of 100$\mu$m, respectively. This substrate contains a glass cloth (prepreg structure) as a reinforcement in order to suppress deformation in the fabrication process. Each cathode strip has 400$\mu$m$\phi$ circular holes with a pitch of 400$\mu$m. 50$\mu$m$\phi$ cylindrical anode electrodes are formed on the anode strips and pierced at the center of each cathode hole.

Using both signals from the orthogonal anodes and cathodes, two-dimensional readout is easily realized. In 2D-MSGCs which have back electrodes on the rear side of the substrate, the induced charge on the back electrode due to cloud of ions around the anode is used for two-dimensional readout (see Fig. 3.2).

In the case of MSGCs with a thin substrate, the back electrode which is grounded is placed on the opposite side of the anode electrodes having a positive electric potential for the cathode. Then the vectors of the electric field around the anode direct the substrate due to the back electrodes. In the other words, as described in Sec. 3.1, the positive ions generated in an avalanche is immediately attached on the substrate. This charging-up

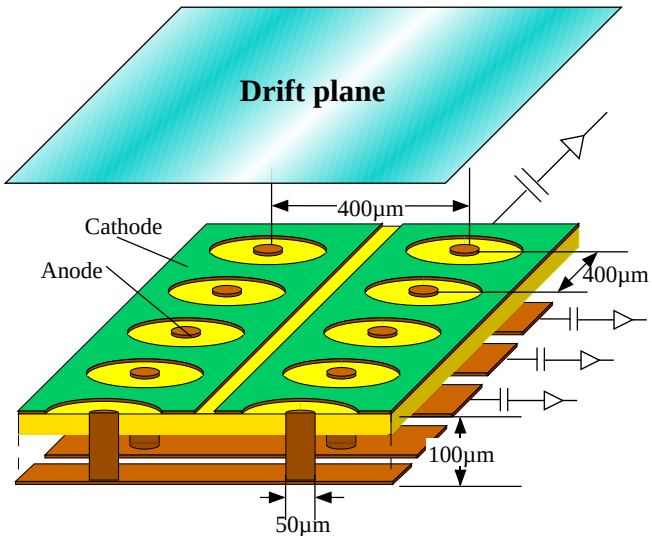


Figure 4.1: Schematic structure of $\mu$-PIC.

of positive ions causes a decrease of the gas gain [35]. In contrast, the back electrodes of $\mu$-PIC is connected to the pixel anodes. Hence, all electric fields on the substrate run upward. Then there are no charging-up of positive ions on the surface. The thickness of the substrate is relatively thick and similar to the distance between the anode and the cathode. This is the one of the outstanding features of our $\mu$-PIC compared with the other pixel detectors made of silicon wafer using IC technology. The electric field due to back electrodes can be weakened at the surface of the substrate. Thus the electric field is not distorted near the substrate by the back electrodes. These design parameters such as the substrate thickness and the anode diameter will be discussed in detail in chapter 7.

### High-voltage supply

Now, $10 \times 10\text{cm}^2$ $\mu$-PICs are available for performance tests. The $\mu$-PIC is mounted on the printed mother-board, on which amplifiers are connected to all readout electrodes (Fig. 4.2). In order to avoid the whole voltage down at discharges, the high voltage is individually applied to every 32 anode strips as shown in Fig. 4.3. At first, the high voltage is divided into eight branch. Each branch has a 1G$\Omega$ resistor, and divided into 32 anodes through 1M$\Omega$ resistors. All cathode strips are grounded through 1M$\Omega$ resistors on

the mother-board. Once a discharge occurs at a certain electrode, the current due to the discharge may affect other electrodes and cause sequential discharges. The 1GΩ resistors protect the electrodes from the discharge current.

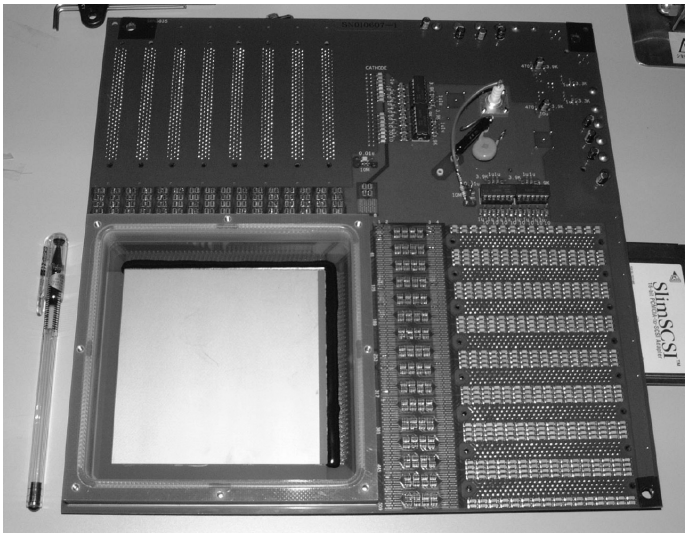

Figure 4.2: Photograph of the printed mother-board of the $\mu$-PIC.

## 4.2 Two-dimensional readout

Since MSGCs have parallel anode and cathode electrodes, two-dimensional readout was not so easy. For two-dimensional readout, it has the backstrip electrodes which are are arranged orthogonally to the anode and the cathode electrodes for our thin substrate MSGC. When an avalanche occurred around an anode, the charge is induced in the backstrip electrode. The amount of the induced charge is a difference between the charges collected by the anode and the cathode. Since major part of the total charge is collected by the cathode, the pulse height from backstrips are reduced to 20$\sim$30% of those from anode electrodes [36]. In contrast, the $\mu$-PIC has the orthogonal anodes and cathodes which collect the charge directly. Therefore, two-dimensional readout is easily realized without any other additional electrodes. Furthermore, as described above, the signal charges from the anode and the cathode is almost same. Fig. 4.4 shows a signal from

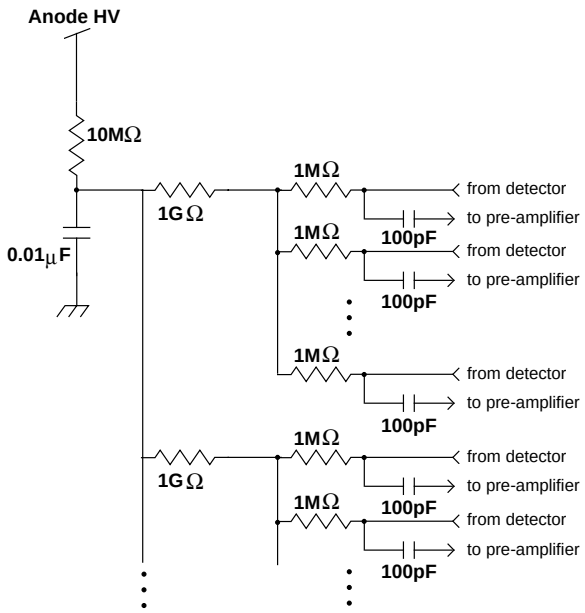


Figure 4.3: Diagram of the circuit to divide the applied voltage to each anode electrode.

both the anode and cathode electrodes for one event.

## 4.3 Fabrication of μ-PIC

We have developed several types of μ-PICs in order to achieve a high gas gain of $\sim 10^4$ and stable operation simultaneously. We have examined several manufacturing processes and the electrode structures, which are briefly summarized in Table 4.1.

### Prototype μ-PIC

The manufacturing process of the μ-PIC with a polyimide substrate is shown in Fig. 4.5. The key technique of the manufacturing is an anode forming. In the case of the prototype μ-PIC [20, 21] which has a detection area of $3 \times 3\text{cm}^2$ on the polyimide substrate, electric plating technique is used for the electrode formation. Copper was deposited in $CuSO_4$ solution from the bottom of the via-hole of 50μm diameter drilled by laser. After the formation of the electrode, the surface of the electrodes was coated with nickel and gold in

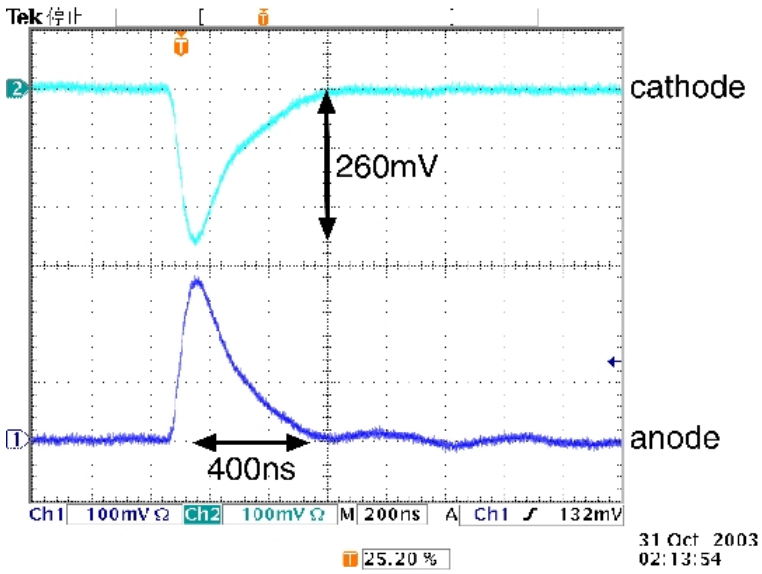


Figure 4.4: Signal shapes from both the anode and cathode electrodes.

| Detector | Substrate material | Electrode materials[a] | Anode height[b] (r.m.s.) | Cathode width |
|---|---|---|---|---|
| prototype | Polyimide | Cu, Ni, Au | $\lesssim 5\mu$m ($33\mu$m) | $359\mu$m |
| $\mu$-PIC1 | Ceramics | W, Ni, Au | $+10\mu$m ($\lesssim 2\mu$m) | $340\mu$m |
| $\mu$-PIC2 | Polyimide | Cu, Ni, Au | $-40\mu$m ($5\mu$m) | $336\mu$m |
| $\mu$-PIC3 | Polyimide | Cu, Ni, Au | $-15\mu$m ($3.6\mu$m) | $314\mu$m |
| $\mu$-PIC4-7 | Polyimide | Cu, Ni | $-20\mu$m ($\sim 3\mu$m) | $314\mu$m |

a: Nickel and gold were used for plating of the electrode surface.

b: Distance between the surface of the substrate and the top of an anode pillar. Negative value means anode electrodes are below the surface.

Table 4.1: Summary of the $\mu$-PICs developed by 2002.

order to protect against oxidation. During the plating process, hydrogen gas is generated from the anode electrodes. The gas bubble blocks up the via-hole (Fig. 4.6), and then anode forming is stopped. Sometimes, other anodes were continuously formed over the via-hole without bubble blocking. Hence, the anode heights become quite random. The number of the anodes which were higher than the surface of the substrate was about 50% of the $75 \times 75$ pixels. The deviation of the anode height from the average was about $30\mu$m (rms), which caused also the large non-uniformity of the gas gain.

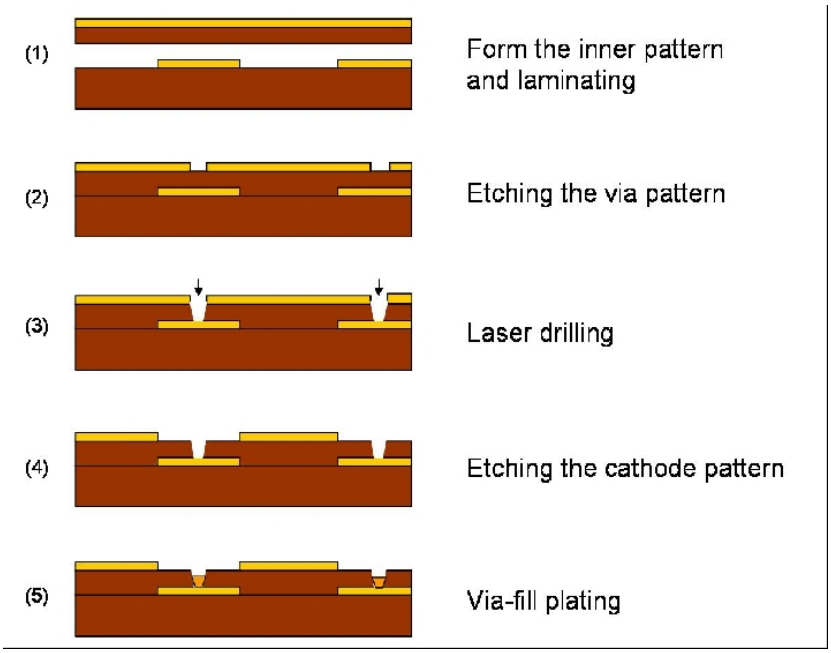


Figure 4.5: Manufacturing process of a polyimide-based $\mu$-PIC.

### Ceramic-based $\mu$-PIC

The manufacturing process of the first $\mu$-PIC ($\mu$-PIC1) having a large area of $10 \times 10\text{cm}^2$ was quite different from that used for the prototype detector in order to obtain the uniformity of the anode height. It is shown schematically in Fig. 4.7. Instead of the electronic plating, the electrodes of $\mu$-PIC1 were formed using conductive paste made from mainly tungsten. In this case, anode and cathode electrodes are "printed" all together. The ceramic ($Al_2O_3$; alumina) substrate is more suitable than polyimide for this process.

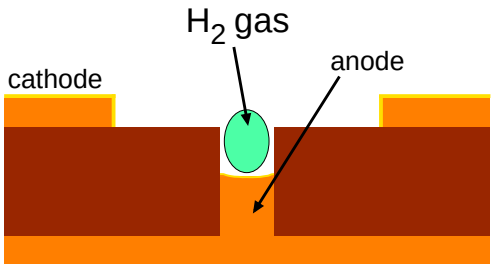


Figure 4.6: Schematic drawing which indicates the blocking of anode formation due to a hydrogen bubble.

Then we manufactured a ceramic-based $\mu$-PIC having the detection area of $10 \times 10\text{cm}^2$. The size of a ceramic substrate is limited by a deformation of substrate in the sintering process. Very uniform electrodes was realized by this method as shown in Fig. 4.8.

Although the $\mu$-PIC1 has very uniform shape electrodes, we found a serious problem of discharges. The anodes and cathodes had been broken down after a few discharges if the $\mu$-PIC1 operated in Ar-$C_2H_6$ mixture gas. The longest operation time was about 1 hour at the gas gain of $\sim$ 1000. The electrodes of the ceramic-based $\mu$-PIC often became conductive after a few small discharges with the resistance of several M$\Omega$ whereas the prototype (polyimide-based) $\mu$-PICs endured several tens discharges. The damaged electrode is shown in Fig. 4.9. When the electrode became conductive, the substrate was severely damaged and changed into black. The polyimide substrate looked to be dissociated due to the high temperature of a spark. In contrast, ceramics is never carbonized. Therefore, other reason of conductivity have to be considered. This conductivity seems due to the stuck of the carbon on the surface of the ceramic substrate that is produced from ethane gas in a discharge process. Ceramics (alumina) has a porous surface. This surface act as an adsorbent material. Then the carbon dissociated from the ethane molecule is stack on the surface of the substrate. Although it was hardly observed for the prototype $\mu$-PIC, the ceramic-based $\mu$-PIC was always suffered from discharges. Therefore, the polyimide substrate is preferred for stable operation. This carbon accumulation was not observed for the operation in inorganic gases such as Ar-$CO_2$ mixture gas. In the case, however, the $\mu$-PIC was not operated stably.

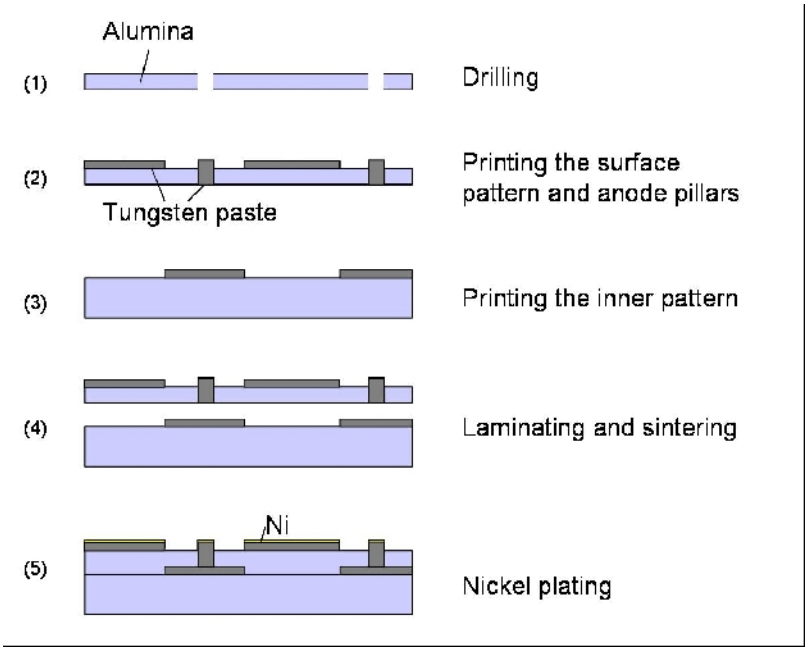


Figure 4.7: Manufacturing process of a ceramic-based $\mu$-PIC.

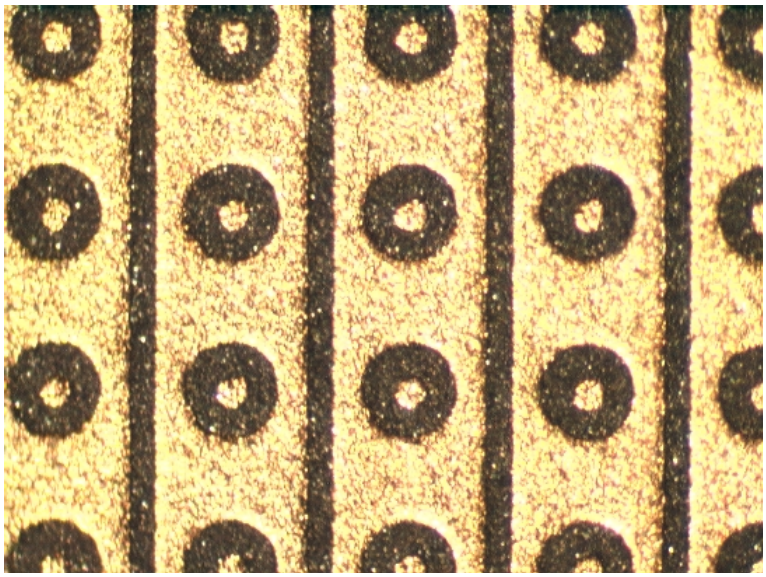

Figure 4.8: Microscopic photograph of a ceramic-based $\mu$-PIC.

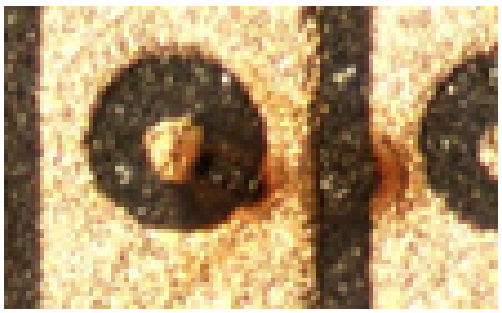

Figure 4.9: Microscopic photograph of a damaged electrode of $\mu$-PIC1.

### Polyimide-based $\mu$-PIC

All $\mu$-PICs (from $\mu$-PIC2 to $\mu$-PIC7) made later had a polyimide substrate. Although the basic structure and the manufacturing process are the same as those of the prototype $\mu$-PIC, the uniformity of the electrode formation have to be dramatically improved for the larger area detector. For this purpose, following improvements were carried out for the fabrication of large area polyimide-based $\mu$-PICs.

**Careful cleaning** The non-uniformity of the anode height was caused by the fluctuation of the start timing of the anode growing due to the pollution in the via-hole. A careful cleaning of the bottom of each via-hole using ultrasonic cleaning was carried out to remove such a pollutants.

**Shape of a via-hole** The shape of the via-hole plays an important role to remove a hydrogen bubble in the via-hole. The via-hole shape of $\mu$-PIC2-7 is slightly tapered, and the surface was desmeared. The desmear process is used to remove tiny pollutants attached on the surface of the via-hole. These processes help a bubble to be removed smoothly from the via-hole.

By these improvements, the blocking up of the via-hole by hydrogen bubble was almost avoided. The deviation of the anodes was decreased from 33$\mu$m (prototype $\mu$-PIC) to 5$\mu$m. In $\mu$-PIC2, the anode formation is stopped at the anode height of 40$\mu$m below the substrate in order to suppress the abnormal deposition of copper which is called

"dendrite". The photograph of an abnormally grown anode is shown in Fig. 4.10. This figure shows the dendrite observed in $\mu$-PIC2. The dendrites should be inactivated by potting silicone rubber on the cathode hole because the extremely high electric field around the dendrites causes non-uniformity of gas gain or discharges.

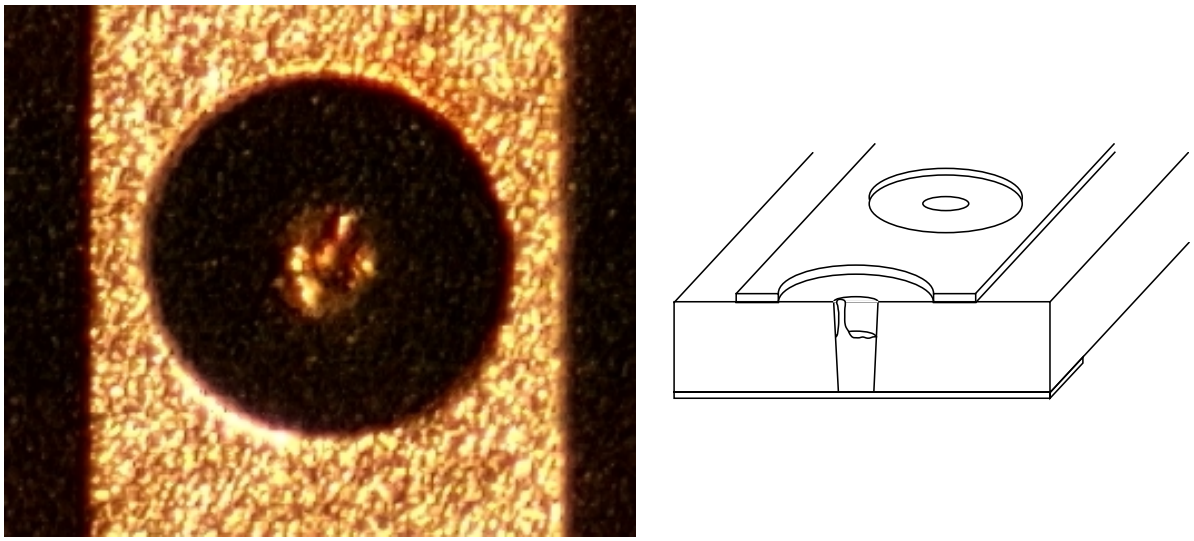

Figure 4.10: The abnormally grown anode which is called "dendrite" (observed in $\mu$-PIC2). The right figure shows a cross-sectional image of the dendrite.

In order to remove the bubble completely and make uniform electrodes, further improvements were carried out.

**Rocking the substrate** In order to accelerate the removal of the hydrogen bubble, the substrate was rocked in the solution during plating. Furthermore, periodic shock is also effective for this purpose. In addition, this process help the circulation of the solution. In order to rock the substrate effectively, a large plating tank was specially prepared for $\mu$-PIC6 and 7.

**Rate of plating** During the plating, cathode electrode (made of copper) is gradually dissolved due to the sulfuric acid contained in the solution. Therefore, a fine tuning of plating rate and composition of the solution is necessary to form a high anode pillar and

wide cathode strips simultaneously. The period of plating was adjusted within 20 hours. Consequently, the width of the cathode strips ($\sim 314\mu$m) become narrower than that of prototype $\mu$-PIC ($\sim 340\mu$m).

After these improvements, uniformity of the anode height was kept within $3\mu$m (rms). However, the formation of the anode electrodes were stopped when the top of the anodes reach $20\mu$m below the surface of the substrate. This depth was inevitably needed in order to avoid the dendrites. Consequently, the number of remained dendrites were decreased within 3% of the whole anode pixels. The microscopic photograph of the polyimide-based $\mu$-PIC is shown in Fig. 4.11. Attachment of carbon dissociated from ethane due

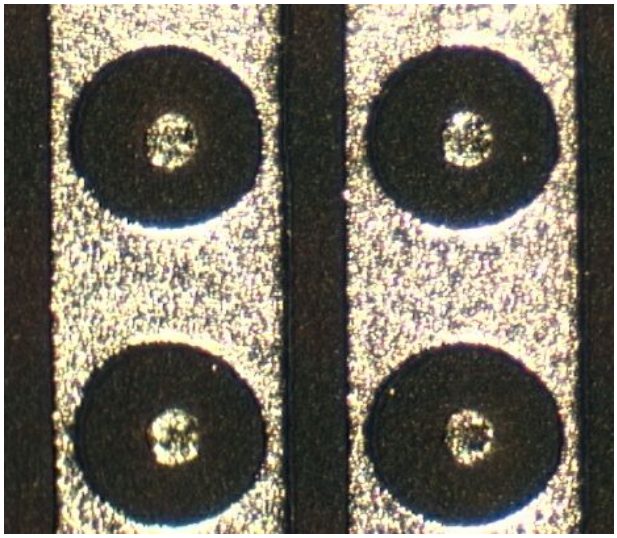

Figure 4.11: Microscopic photograph of a polyimide-based $\mu$-PIC.

to discharge was hardly observed for the polyimide-based $\mu$-PICs. Therefore, damage of discharges is much smaller than that of ceramic-based $\mu$-PIC. Thus the stability was drastically improved for the polyimide-based $\mu$-PICs. The long time continuous operation of more than 1000 hours was realized with the gas gain of 3000 as described in chapter 6.

Although we had succeeded to suppress the break-down of the electrode of the $\mu$-PIC, following problems still remained. The first problem is loss of the cathode strips during the plating process. If the cathode strips are narrow, the electric field near the cathode

electrode is not uniform. Second, some fluctuation of anode height still remained within $\sim 3\mu$m. As described in later section (Sec. 6.1), this problem quite affects to the gas gain uniformity. At last, the top of all anode electrodes are $20\mu$m below the surface of the substrate. The drift of the primary electrons are partly prevented by the edge of the substrate. This problem is discussed in chapter 7.

## 4.4 Discharge

### 4.4.1 Streamer

Electrons in the avalanche are spherically diffused due to the thermal fluctuation during the drift process. On the other hand, the positive ions are regarded as stopping at the position of ionization, because the drift velocity of positive ions is much slower than that of electrons. Thus, the shape of the growing avalanche is like a water drop consisting of a spherical electron cluster and positive ion tail [25]. When the strength of the electric field generated by the space charge of the avalanche is similar to the drift electric field, the avalanche does not grow any more. In this phase, the strong electric field is localized in front and behind the primary avalanche. The secondary ionization is occurred by the UV emission from the excited atoms in the avalanche cloud, and secondary avalanches grow in front and behind the primary avalanche. Eventually a long filament-like forward and backward charge propagation appears. This become a conductive channel called "streamer", which leads a fast discharge. These processes are schematically shown in Fig. 4.12.

Once the total charge in one avalanche exceeds $10^{7-8}e$, the streamer formation rapidly proceeds [38]. This limit charge is known as Raether limit. For a heavily ionizing particle (such as an $\alpha$ particle), about $10^4$ electron ion pairs are typically created, and the maximum gas gain to avoid the Raether limit is between $10^3$ and $10^4$. Thus the gas gain of detectors is restricted so as to control the total charge of the avalanche within the Raether limit.

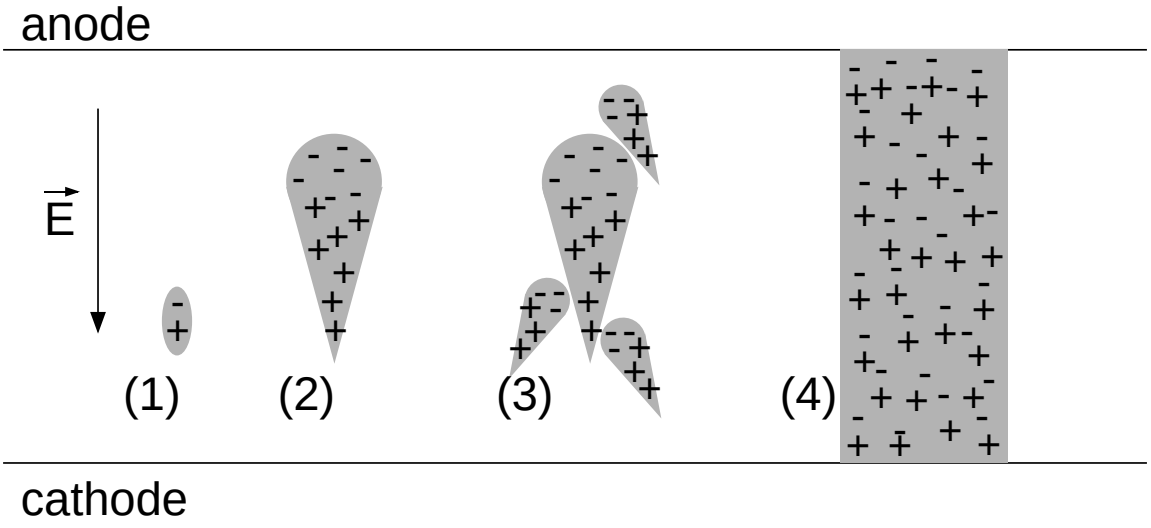


Figure 4.12: Growth of an avalanche into a streamer. (1) The initial ionization occurs in the electric field $\vec{E}$. (2) The electron avalanche grows in the strong electric field. (3) The secondary avalanches occur by localized electric field near the primary avalanche. (4) The avalanche grows up to a conductive plasma called a streamer.

### 4.4.2 Field emission

Discharges in a gas detector are usually triggered by an electron. In ordinary operation, electrons are generated only by the incident particles. However, discharges may occur without irradiation. Thus, in this case, the electron(s) generated somewhere in the detector triggers a discharge. In a high electric field, electrons are emitted from the surface of metal due to the tunnel effect [39]. The current density $j$ due to the electron emission is expressed by Fowler-Nordheim's equation as follows:

$$j = 1.55 \times 10^{-6} \, \frac{E^2}{\phi} \, \exp\left( -6.83 \times 10^7 \, v \, \frac{\phi^{3/2}}{E} \right), \tag{4.1}$$

where $E$ is the electric field, and $\phi$ is a work function of the metal, which is between 4 and 5 for many metals. $v$ is a correction term of the work function in the electric field. Here, the value of $v$ is close to 1 [40]. The threshold electric field to avoid discharges can be calculated using this equation by measuring the rate of discharges. When discharge occurs with the rate of $\sim 1$/min, the current density becomes the order of $10^{-21}$A/cm$^2$. Then the threshold electric field is about 800kV/cm. While the electric field near the electrode exceed this value, field emissions are initiated and trigger a discharge.

### 4.4.3 Discharges in MicroPattern detectors

#### Surface discharge

The electrodes of MPGDs are usually formed on the surface of the substrate. In other words, MPGDs have "triple junctions" which consists of the electrodes, the dielectric (substrate), and the gas. The electric field near the triple junction becomes strong due to the discontinuity of the dielectric constants among the materials. In this case, break-down due to the "surface discharge" or the "surface breakdown" from the triple junction is an important process of the discharge. In particular, the strong electric field which exceeds the threshold of field emission may be localized near the triple junctions of the cathode. In the strong field, electrons can be emitted from the cathode by a field emission process. When this electron collides the surface of the dielectric, the surface is positively charged up through the Secondary Emission Electron Avalanche (SEEA) mechanism [41]. It is

considered that this positive charging-up proceeds to the surface discharge, although the detailed process from charging-up to discharge is not clear yet.

### Malter effect

If the organic gases such as methane or ethane are used as quenching gases, some molecules are dissociated by the incident particles. Then free radicals are formed, which is polymerized and stuck on the electrodes due to electrostatic attraction [42]. Once a thin insulator film is stuck on the surface of the cathode the positive ions accumulate on the insulator layer, which acts as a capacitor. The electric field in the insulator may become strong enough to occur the field emission. This electron emission caused by a thin insulator is called "Malter effect" [43]. This is a kind of dielectric breakdown. The Malter electrons cause a self-sustained discharge [44]. Sometimes, the electrons can be emitted all at once like a jet, which is considered to be a main break-down triggering mechanism [45].

### Surface conductivity

When the gas used in the detector contains an organic gas as a quencher, the molecule of the organic gas is dissociated by the high temperature due to a discharge. Then a cluster of carbon is produced along the discharge path. In MPGDs, the radical carbon may be accumulated on the surface of the substrate between an anode and a cathode, which makes the surface of MPGDs conductive. The tendency of the accumulation depends on the material of the substrate. If the substrate is made of a porous material such as alumina, hydrocarbon such as ethane is easily dissociated and attached on the surface, because the porous material act as a adsorbent. On the other hand, the polyimide surface has less adsorbent property. Thus the carbon accumulation rarely occurs for the polyimide substrate. However, once the surface becomes rough due to discharge damages, the carbon maybe accumulate on the surface, and causes a breakdown. Also, the polyimide substrate may be carbonized by a high temperature due to a discharge, which becomes a bridge of conductivity.

### Discharges in MSGC and $\mu$-PIC

In MSGCs, the electric field near the cathode edge becomes more than 100kV/cm which is high enough for a gas avalanche. Therefore, once an electron is ejected from the cathode due to field emission, the electron undergo the gas multiplication near the cathode edge. The multiplied electrons directly drift toward the anode and multiplication occurs again. As a result, gas multiplication factor increases up to $10^5$ [46]. The maximum gas gain of MSGCs is restricted to $\sim$ 1000 by this multiplication due to electron emission from the cathode edge. In order to suppress the electron emission, the MSGC of which cathode edge was covered by polyimide was developed [47]. In this case, it is necessary to consider the accumulation of positive ions on the polyimide.

In $\mu$-PIC, electrons emitted from the triple junctions run on the surface of the substrate with avalanche multiplication. Then these electrons may cause the surface discharge. In any case, the discharges looks triggered by the electron emission in a high electric field near the cathode edge. In order to suppress discharges, we have attempted weakening the strength of electric field near the triple junction of the cathode edge, which is discussed in later chapter.

# Chapter 5

# Data Acquisition System

The data acquisition (DAQ) system is one of the most important parts in the development of $\mu$-PIC to handle a huge number of signals from fine electrodes of $\mu$-PIC. In this section, the overview of the DAQ system for the imaging and its performance are described.

## 5.1 Overview of the DAQ system

The narrow electrode spacing of $\mu$-PIC allows us to operate in high counting rate up to $10^7$ counts per second and obtain a very fine position resolution. In order to obtain these features, the fast readout electronics is inevitable, which handle a large number of signals from 256 anodes and 256 cathodes of $10 \times 10\text{cm}^2$ $\mu$-PIC. In order to apply the $\mu$-PIC as a real time imaging detector, a data acquisition rate of more than 20MHz is required. Especially for charged particle tracking using a TPC, the spatial resolution along the drift direction is determined by the processing speed. For example, in a gas with the electron drift velocity of 4.5cm/$\mu$sec, the spatial resolution for drift direction would be less than 1mm for the DAQ system operated with 50MHz, whereas that is 2.3mm for the DAQ rate of 20MHz. The analog data processing is ill-suited for the high-speed and multi-channel data acquisition which is required for the $\mu$-PIC. Alternately, we have developed the DAQ system which handle all signals digitally.

The DAQ system for two-dimensional imaging consists of following parts:

- 16 amplifier-shaper-discriminator (ASD) boards,

- one position encoding module,
- one memory module,
- one CPU board.

The block diagram of this DAQ system is shown in Fig. 5.1.

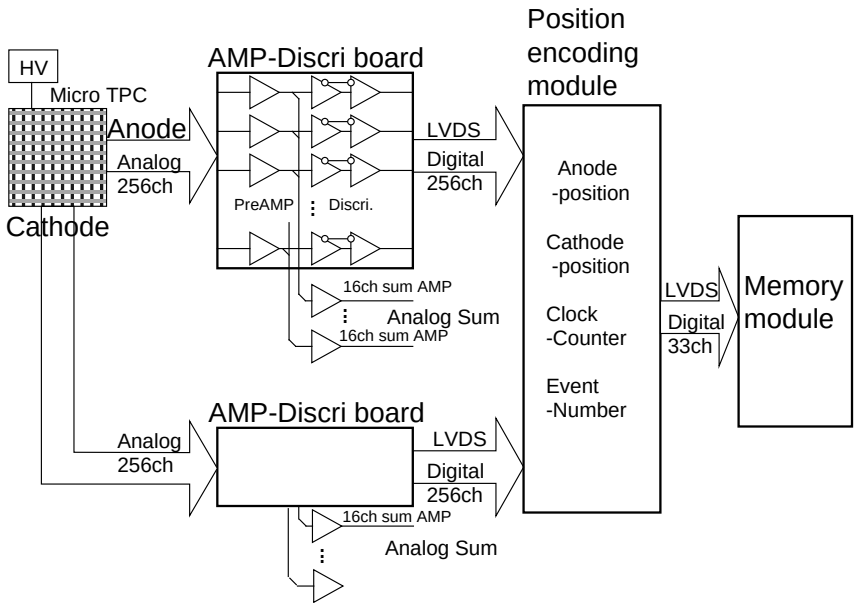


Figure 5.1: Block diagram of the DAQ system.

Pulses from anodes and cathodes are individually amplified by ASD boards (Fig. 5.2). An ASD board has 16 ASD chips which were originally developed by KEK for ATLAS Thin Gap Chambers (TGC) [48]. The ASD chip consists of a fast preamplifier (gain $\approx 0.8$V/pC), shaping amp (gain = 7), and discriminator. One ASD chip has four inputs, four discriminator outputs, and four analog outputs from each preamplifier. The block diagram of one channel of the ASD chip is shown in Fig. 5.3. Each 16 analog signals of 32 channels are summed at the end of the board. The discriminator output of amplifier boards is LVDS differential signal, which are directly fed to the FPGA chips in the position encoding module.

Because the ASD signal from TGC is originally used for the trigger decision, the integration constant is very fast ($\tau = 16$nsec). However, this integration constant is too

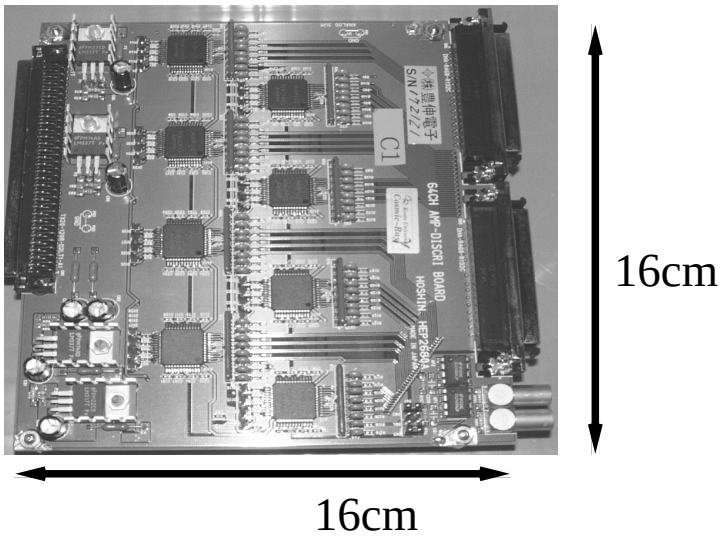


Figure 5.2: Photograph of an ASD board.

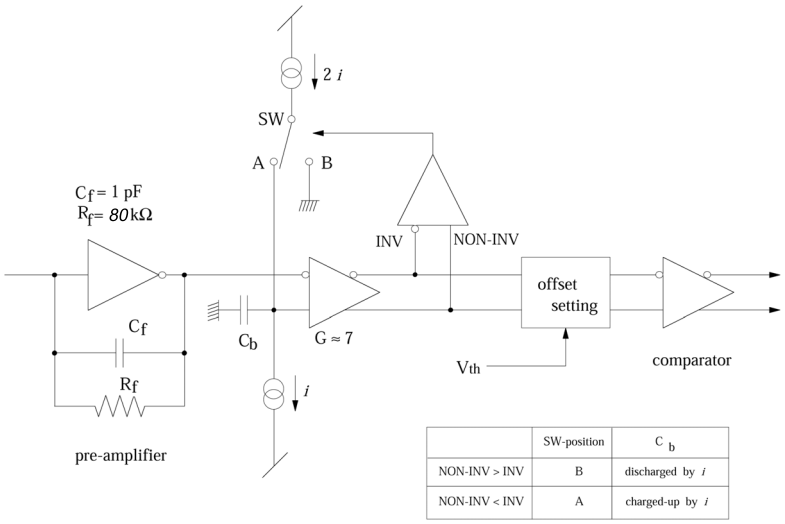


Figure 5.3: Block diagram of the ASD chip.

short to collect all pulse charges from the $\mu$-PIC. Therefore, the measured pulse height of the analog output was lower than that expected from the gas multiplication. By the simulation, if the integration constant of the preamplifier were extended to 80nsec, the signal from the $\mu$-PIC would be twice higher than that of using 16nsec integration constant amplifier [49]. The output signal of the improved ASD was compared with the original ASD for TGC. Fig. 5.4 shows the signals of the 5.9keV X-ray obtained by $\mu$-PIC with the original ASD (upper signal) and the improved ASD (lower signal) [49]. Thus we have developed the new ASD with the integration constant of 80nsec.

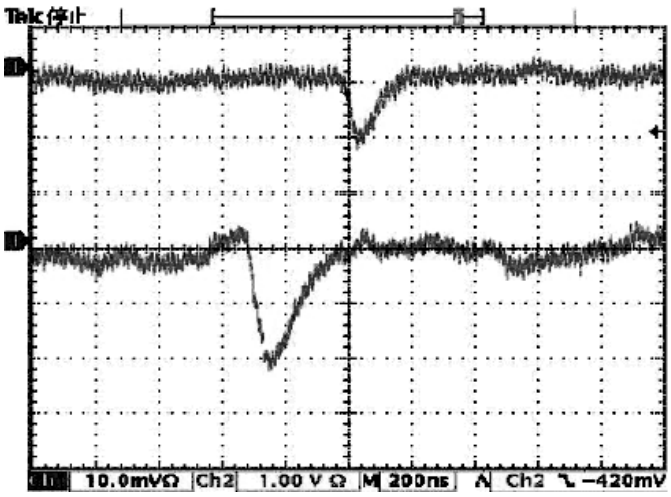


Figure 5.4: Upper signal and lower signal were obtained by original and improved ASDs, respectively.

The digital signals from ASD boards are fed to the position encoding module, where the position of the hit electrode is encoded. Fig. 5.5 shows the position encoding module, which consists of five Field Programmable Gate Arrays (FPGAs; Xilinx Virtex-E). These FPGAs accept LVDS signals without any external terminators. The position encoding logic of FPGAs used here can be rewritten for various purposes. This system operates with the clock of 20MHz or 40MHz. In one event all signals are synchronized to the clock and processed in one clock using a pipeline processing.

The hit position of X-ray is encoded as following (see also Fig. 5.6). 256 channel LVDS signals from anode are fed to two FPGAs. At first, these signals are synchronized to the

Figure 5.5: Photograph of the position encoding module.

clock in each FPGA (Fig. 5.7), then the minimum and maximum channel position of the hit anode electrode are also encoded here. Simultaneously, the minimum and maximum channel position of the cathode is also encoded in the other two FPGAs by the same method. These information from four FPGAs are fed to the fifth FPGA, which requires the both hits in the anode and cathode in the same internal clock, and encode the number of hit electrodes (corresponding to the hit width) and the both center positions for anode hits and cathode hits. Here, an event with the hit width of less than or equal to 8 is regarded as a valid event. An event having the width of more than 8 is rejected as a noisy or an accidental event. Resultant encoding information of output signal is fed to the VME memory module as a sequence of 33bit parallel signal, which consists of 32bit main signal (position, width, etc.) and auxiliary 1bit WRITE signal. The correctly encoded signals should have the WRITE signal as well as the 32bit main signals. This encoding logic obtains an arithmetic mean of the hit signals whereas weighted mean of charge is often used for conventional wire chambers. Since the size of a primary electron cloud is similar to the electrode pitch of the $\mu$-PIC, the spatial resolution of about 100$\mu$m is expected by

this simple method.

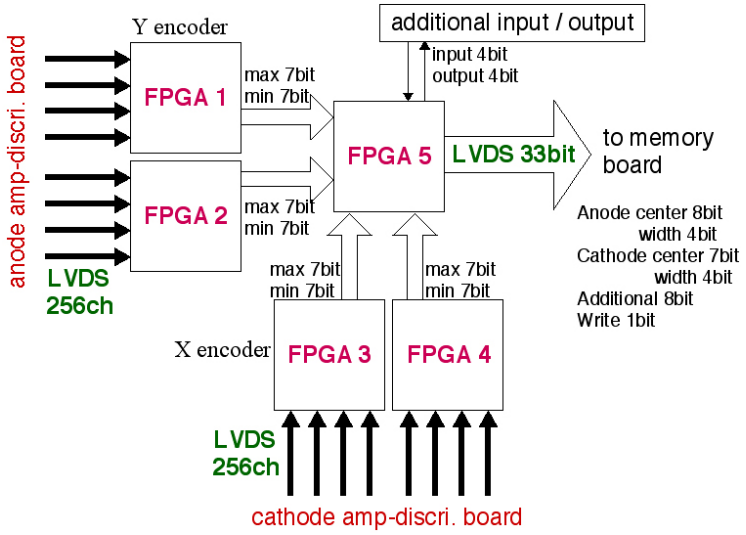


Figure 5.6: Block diagram of the position encoding module.

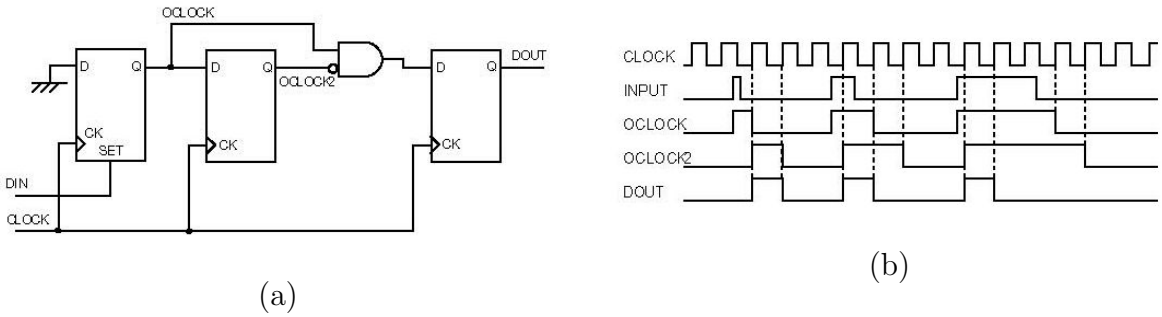


Figure 5.7: Circuit diagram (a) and a timing chart (b) of the synchronizing circuit [50].

The information obtained by the position encoding module are sent in LVDS level through a 33 channel cable to a VME6U-based 32 bits memory module. This module consists of SRAM memories of 32MByte in total, because high-speed read and write operation is possible for SRAM. Fig. 5.8 shows a photograph of the memory module. The validity check is carried out hear using the WRITE signal, and the accepted signals

are accumulated in the SRAM memories. This memory module is controlled by the CPU board, which also controls other modules concerning with the DAQ system, such as ADCs.

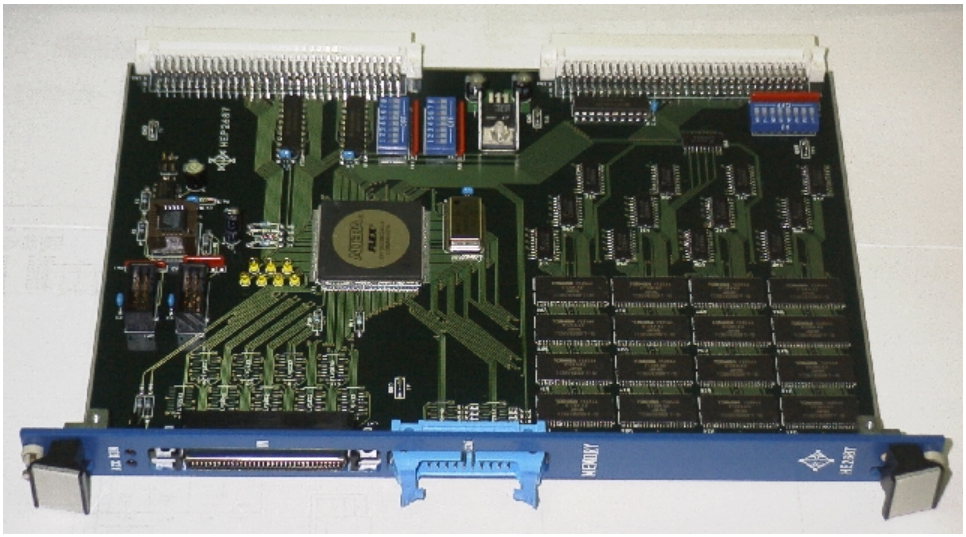

Figure 5.8: Photograph of the memory module.

## 5.2 Performance

The performance of the DAQ system for the high counting rate was studied using an X-ray generator (Kevex X-ray CU028, tungsten target). The acceleration voltage of the generator was 20kV and the intensity was controlled by varying the tube current between 0.01mA and 0.6mA. The DAQ was operated with the clock of 40MHz. The result of the high rate test is shown in Fig. 5.9, where the data acquisition rate against the tube current is plotted. We achieved the maximum data acquisition rate of 7.7MHz, which is twice higher than that of the previous DAQ system developed for two-dimensional MSGCs [6]. This system has a capability of $40 \times 10^6$ event per second for synchronous events. However, X-ray usually enter the detector at random, and the duplication hits within one clock degrades the capability. The number of incident events in one clock follows the Poisson distribution. Therefore, the expected data acquisition rate $R$ is calculated by the following

formula:

$$R(r) = r \cdot \exp(-r/c), \tag{5.1}$$

where, $r$ is a real event rate, and $c$ is the clock cycle of the DAQ system. The maximum value of $R(r)$ is $c/e$ at $r = c$. When the clock is 40MHz, the theoretical limit of the data acquisition limit is 14.7MHz. The obtained counting rate was about half of the expected counting rate from the Poisson distribution. The saturation is thought to be due to the time-lag between the signal lines in the FPGAs.

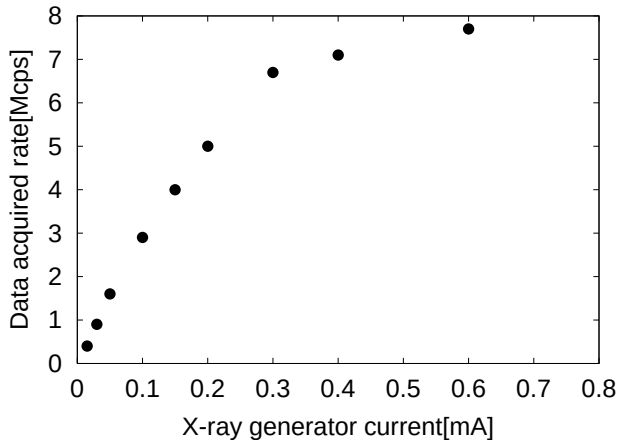


Figure 5.9: Result of the high rate test of the $\mu$-PIC and the DAQ system.

# Chapter 6

# Performance of the $\mu$-PIC

The performances of the $\mu$-PIC, about gas gains, energy resolution, and long time stability are described here. This study becomes a basis for all applications of the $\mu$-PIC.

## 6.1 Performance test of the $\mu$-PIC

The detectors were operated in $Ar/C_2H_6$ (80/20) gas mixture at the atmospheric pressure. The depth of the drift space was 1.2cm and an electric field of 500V/cm was applied. The positive high voltage was applied to anode electrodes, and all cathode electrodes were grounded. Here the polyimide-based $\mu$-PIC with lower anode ($\mu$-PIC4-7) is described for all performance tests in this section.

$\mu$-PIC was irradiated by a non-collimated radioactive source of $^{55}$Fe (5.9keV), and the output charge of the sum of $32 \times 256$ pixels was measured. The gas gains were calculated from the obtained charge. Fig. 6.1 shows the obtained gas gains as a function of the anode voltage, which are plotted as filled squares. The maximum gas gain of $1.5 \times 10^4$ was achieved, which is about 10 times higher than that of stand-alone MSGCs. Stable operation was attained at the gas gain of between 3000 and 5000.

The obtained spectrum of $^{55}$Fe source (5.9keV) was shown in Fig. 6.2 In this experiment, $32 \times 32$ pixels ($12.8 \times 12.8$mm$^2$) were used for signal readout. The spectrum obtained from this area is shown in Fig. 6.2 (a). An escape peak is seen at 2.7keV as well as the main peak of 5.9keV. Achieved energy resolution of this area was about 30%

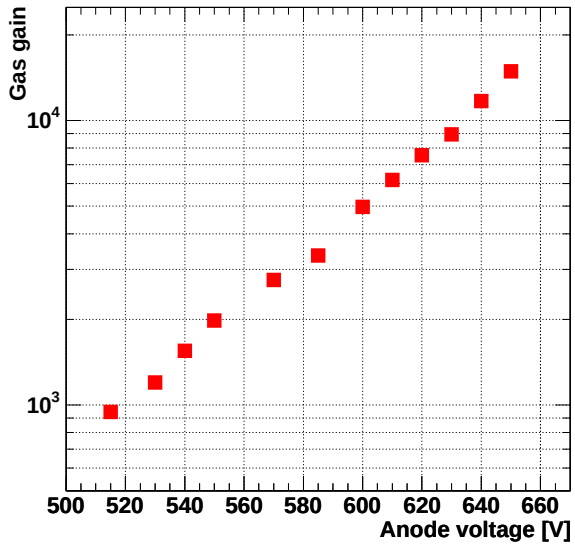


Figure 6.1: Gas gain curve of the $\mu$-PIC as a function of the applied voltage.

(FWHM). The spectrum from whole detection area is also shown in Fig. 6.2 (b). This spectrum was obtained using a Flash ADC (FADC). In this case, the escape peak is not clear. The energy resolution of this area was about 50% (FWHM).

The position dependences of the gas gain are measured for all detection area of the $\mu$-PIC4. The detection area was divided into $8 \times 8$ regions, and gas gain was measured from the peak of the spectrum for each region which consists of $32 \times 32$ pixels. The result is shown in Fig. 6.3. There observed a large fluctuation of the gas gain. The maximum gas gain was about 5 times higher than the minimum gas gain. The standard deviation of the gas gain was more than 40%. All polyimide-based $\mu$-PICs with the lower anodes have a similar tendency of the gas gain fluctuation. This deviation can be attributed to the non-uniformity of the anode heights of which deviation was 3-5$\mu$m. This non-uniformity of the gas gain causes unstable operation. If there are some spot of extremely high gas gain, the maximum voltage for stable operation is governed by the high gain area. Consequently, low gas gain will obtained by the remaining (large) area.

One of the important properties of the $\mu$-PIC is the capability of high counting rate. In the conventional MWPCs, positive ions produced in the avalanche drifts toward the

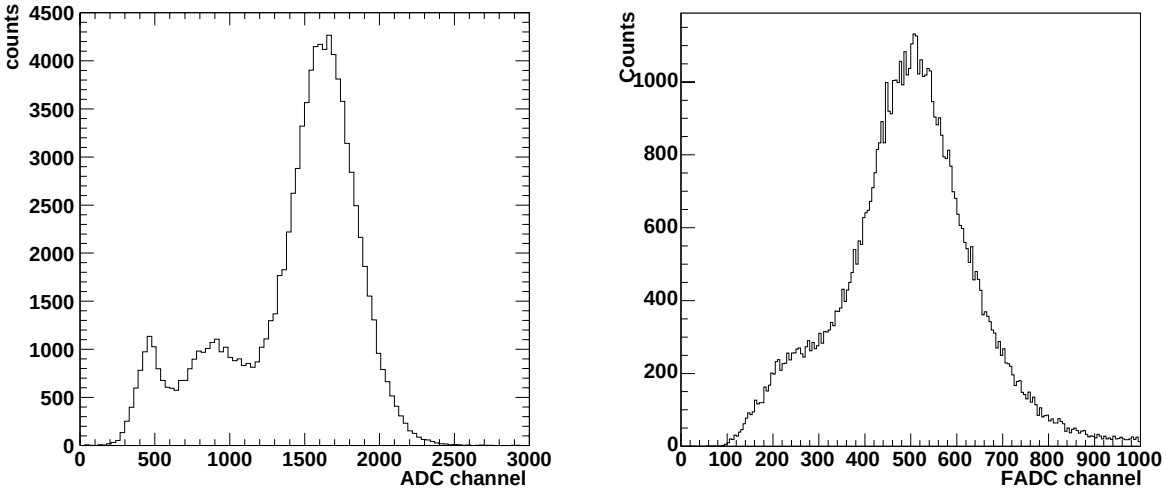


(a) (b)

Figure 6.2: Energy spectra of $^{55}$Fe source. (a) Obtained from the detection area of $12.8 \times 12.8\text{mm}^2$. (b) Obtained from the whole detection area ($100 \times 100\text{mm}^2$).

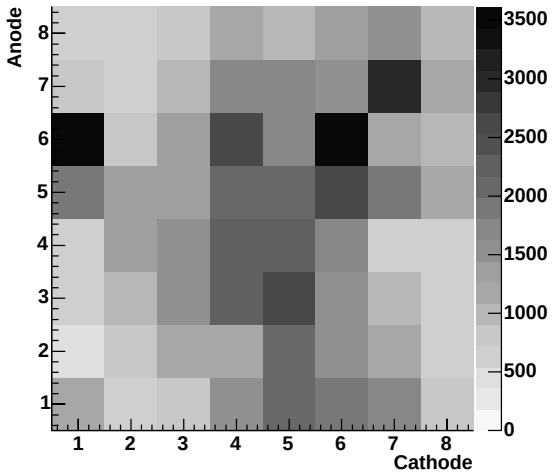


Figure 6.3: Map of the measured gas gains.

cathode electrode which is also used as a drift electrode. High rate capability is restricted to $10^{3-4}$cps/mm$^2$ by the drift time of positive ions (∼1msec). On the other hand, positive ions from the avalanche are expected to drift toward the cathode electrode formed on the substrate near the anode. The drift time of the positive ions from an anode to a cathode is about 200ns. If some positive ions escape toward the drift electrode, the feedback ions will be observed as a current $I_d$ between the drift plane and the ground. In contrast, a current $I_a$ between the anode electrodes and the ground is the summation of the drift current $I_d$ and the cathode current $I_c$ corresponding to the collected charge by the cathode. Since the cathode current can not be measured directly in our system, we measured the drift current $I_d$ and the anode current $I_a$. The fraction of the feedback ion is defined as a ratio of $I_d$ to $I_a$. Incident X-rays were collimated through a 10mm thick lead block with a hole of 6mm diameter. Fig. 6.4 shows the measured anode and feedback current for $\mu$-PIC6 as a function of the counting rate of X-rays. The observed drift current was about 25% of the anode current which corresponds to the total collected charge, and this fraction was independent of the X-ray intensity.

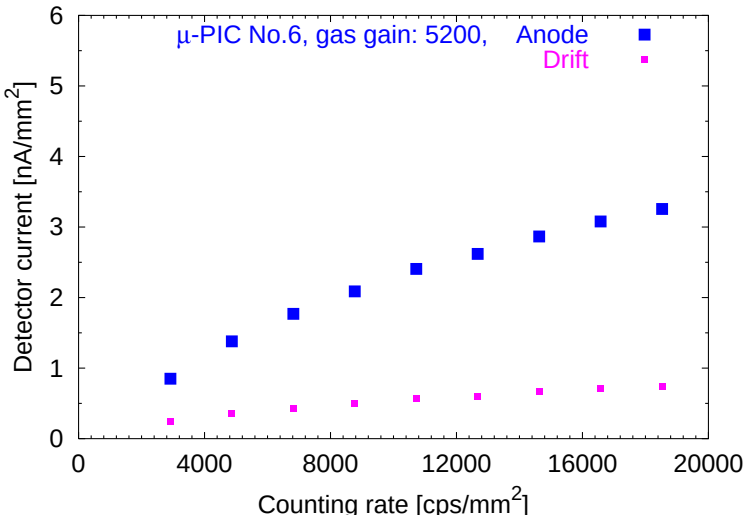


Figure 6.4: Anode and feedback current as a function of the counting rate of X-ray.

## 6.2 Long term stability

Long term stability of the gas gain is most important for various applications of $\mu$-PIC. In MSGCs, the gas gain decreases in one hour. It is explained by charging-up of positive ions on the substrate. This degradation can be avoided by fine tuning of the anode-cathode and anode-backelectrode voltages [2]. In this case, the gas gain slowly increases in a few hours or longer. It is considered that this increasing of gas gain is due to the dielectric polarization of the substrate.

On the other hand, there is no charging-up of positive ions for $\mu$-PIC because of the electrode structure as mentioned in Sec. 4.1. However, the effect of the dielectric polarization in the $\mu$-PIC was unknown, which should be observed because polyimide is also used as an insulator similar to MSGC.

The variation of the gas gain was measured for the previous $\mu$-PIC for 120 hours (about 5 days) with the gain of more than 3000. During this measurement, the $\mu$-PIC was irradiated by an $^{55}$Fe source with counting rate of $\sim$150counts/sec. Fig. 6.5 shows the gas gain variation as a function of the elapsed time since the anode voltage supply. Slight increase of the gas gain was observed in the first 20 hours, which we think is due to the polarization effect of the polyimide substrate. In the first a few hours, there were steep increase of the gas gain. It can be understood as the electron attachment on the substrate. In this case, the electric field due to the attached electrons is superimposed on the primary electric field due to the electrodes. As described in chapter 7, the electron attachment is attributed to the lower anode height of 20$\mu$m below the substrate surface. If the anodes were higher than the substrate, no electron attachment would be expected. Thus variation of the gas gain would be small. This will be described in next chapter.

Another variation of the gas gain in a few months was also observed. Fig. 6.6 shows the gain curve observed in 15 August 2002 (filled circle) and 23 October 2002 (filled square). During this interval, the gas gain became about 2 times higher. This effect is explained as water contamination. Polyimide substrate is thought to contain some water just after the fabrication. This water gradually evaporates during the operation, then the water vapor contaminate the detector gas ($Ar/C_2H_6$ mixture). Because, the water molecule has polarity, some primary electrons are captured by the molecule. Therefore, the resultant gas gain is considered to be degraded in the detector during the early phase

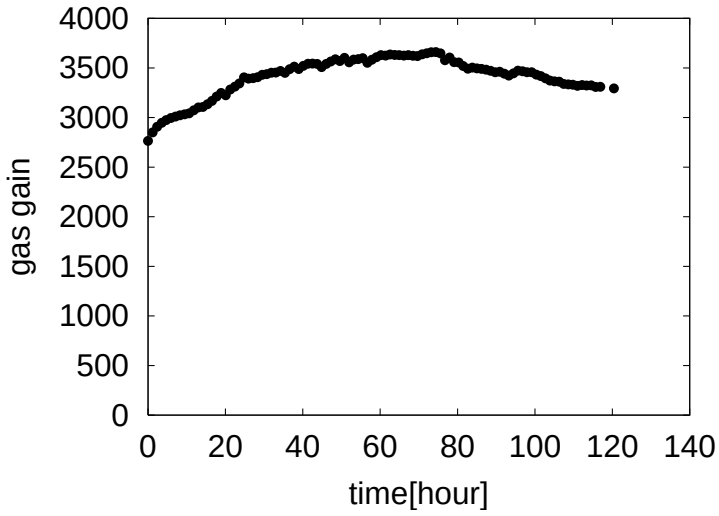


Figure 6.5: Gas gain variation as a function of the time.

of the operation. The gas gain increases gradually with the evaporation of the water in the substrate. After a months, the gas gain become constant for all $\mu$-PICs. In order to obtain a stable gas gain from the beginning of operation, it is important to completely evaporate the water contained in the polyimide substrate using vacuum dehydration, which has to be carried out in near future.

## 6.3 Operation in carbon tetrafluoride gas

As described in Sec. 2.3, the $CF_4$ gas is suitable for a tracking of MIPs. Furthermore, high detection efficiency is expected by pressurized $CF_4$ gas. However, there are few samples which reported the performances in $CF_4$ gas for pixel detectors. The operation test of the $\mu$-PIC in $CF_4/C_2H_6$ mixture gas was performed using a prototype $\mu$-PIC with the detection area of $3 \times 3\text{cm}^2$. The variation of the gas gain in $CF_4$ by changing the gas pressure was measured. The experimental setup is shown in Fig. 6.7. The $\mu$-PIC (prototype) was installed in the gas pressure vessel. We measured the analog summed signal from $10 \times 70$ pixels using a charged pre-amplifier with a gain of 1V/pC. As shown in Figs. 6.8, the gas gain of over $10^3$ was obtained at a pressure of 2.5atm, although

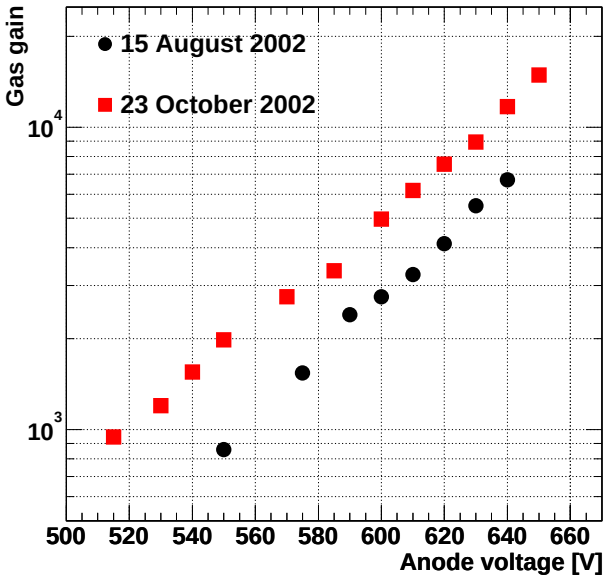


Figure 6.6: Gas gain variation in two months.

somewhat higher operation voltage was required than argon-based gas.

In this experiment, significant stability in high gas gain up to $10^4$ was not obtained. The best condition should be found to obtain high gas gain and stability. For this purpose, we will try other combination of gases, such as $Ar/CF_4/C_2H_6$.

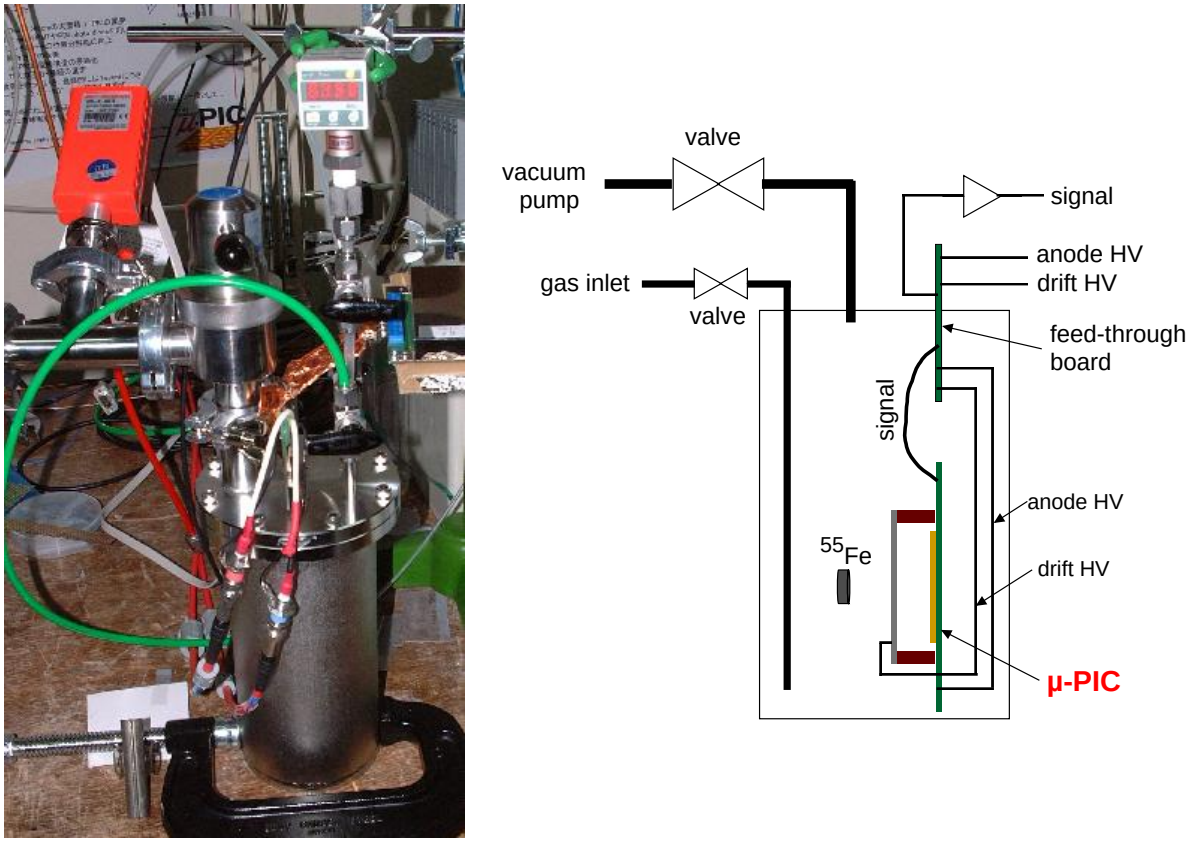


Figure 6.7: Experimental setup for $CF_4$ and high pressure test.

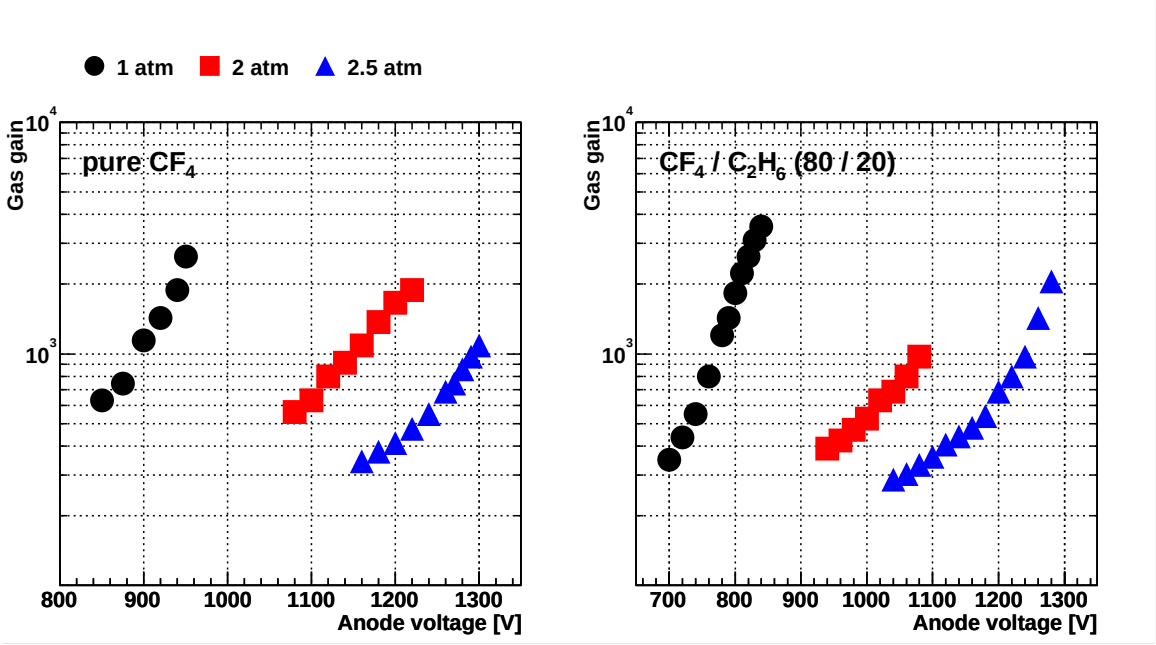


Figure 6.8: Gas gain curve obtained by $CF_4$ test.

# Chapter 7

# Improvement of $\mu$-PIC

We found that the $\mu$-PICs with lower anode have some problems. In this chapter, we investigated these problems quantitatively using a three-dimensional simulation, and found a new electrode structure to overcome problems.

## 7.1 Problem of former $\mu$-PICs

The $\mu$-PICs with lower anode achieved high gas gain ($\sim 10^4$) and stable operation with low gas gain of 3000. However, we need to obtain the stable operation with high gas gain of 10000 for its applications. First, we summarize the defects of the $\mu$-PICs.

**Non-uniformity of gas gain** If we focus on a narrow region of the detection area, the energy resolution of about 30% was obtained. As shown in Fig. 6.3, however, the gas gain strongly depends on the position. The factor 5 of difference was measured between the minimum gas gain and the maximum one.

**Low gas gain** The required gas gain for detection of a MIP track is derived from the W-value and $\mathrm{d}E/\mathrm{d}x$ of each gas. Using the data described in table 2.1, the gas gain of more than $10^4$ is needed for $\mu$-PICs. Furthermore, stable operation is also required at this high gas gain. Although the maximum gas gain of $10^4$ was achieved, stable operation could be obtained only in a low ($< 5000$) gas gain.

These problems were considered to be attributed to the lower anode height, which was due to the manufacturing conditions of the $\mu$-PIC. As mentioned before, the anode height was limited to $\sim 20\mu$m below the surface of the substrate to keep the uniformity of the anode height. Even in this condition, the uniformity of the anode height is also restricted within $3\mu$m. In order to estimate how the performance of the $\mu$-PIC would be improved due to the uniform and high anode, we performed a three-dimensional simulation varying the geometrical parameters of the $\mu$-PIC.

The feature of the $\mu$-PIC which clearly differentiate from the MDOT detector is the thickness of the substrate. As mentioned in Sec. 3.3, the electric field near the substrate of the MDOT is affected by the anode readout buses. Therefore, the effect of the substrate thickness must be investigated using the simulation.

## 7.2 Simulation study

### 7.2.1 Simulation method

#### Simulation code

Here, simulation studies were carried out using MAXWELL 3-D Field Simulator (hereafter, MAXWELL) [53] and GARFIELD [54]. The electromagnetic field in a three-dimensional structure was calculated using a finite element method by the MAXWELL program. In this method, the structure is divided into fine tetrahedrons called "mesh". The electromagnetic field is calculated in each mesh point based on Maxwell's equations. A unit cell of the $\mu$-PIC was created in the MAXWELL program, which has a size of $400 \times 400\mu\text{m}^2$ and consists of a polyimide substrate with a relative dielectric constant of 3.5 and a pair of anode and cathode electrodes. Fig. 7.1 shows the mesh structure of a unit cell of the $\mu$-PIC. Maps of the electric field, the voltage, and the dielectric constant were generated at each unit cell, which are called the "field maps". The infinite repetitive structure (Fig. 7.2) was created by combining the unit cell with a periodic boundary condition.

These maps were fed to GARFIELD and then the dynamics of the drift electrons

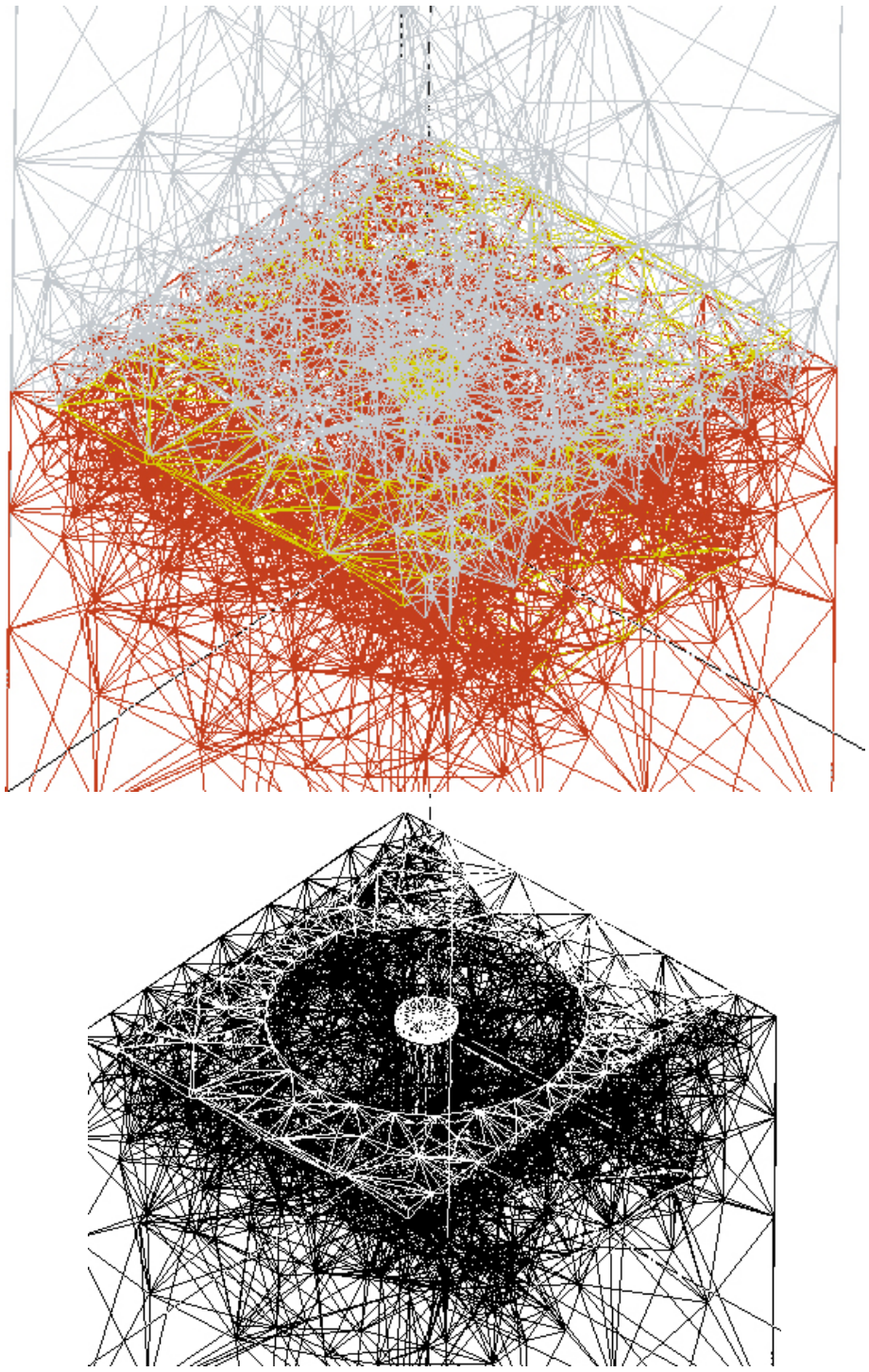

Figure 7.1: Mesh structure of the $\mu$-PIC. The upper panel shows the full mesh including the drift space. The lower one shows only the structure of the detector.

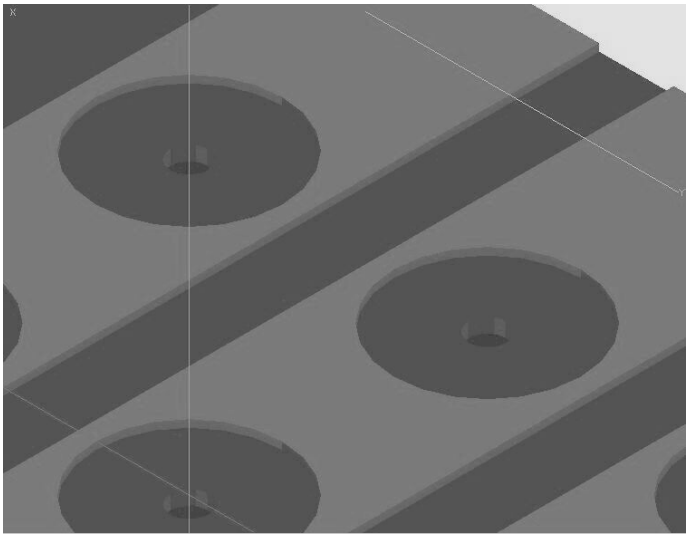

Figure 7.2: Basic $\mu$-PIC structure generated by MAXWELL.

were simulated. GARFIELD is a program for the detailed simulation of drift chambers. Originally GARFIELD does not deal with dielectrics and three-dimensional structures. However, GARFIELD can read the field maps generated by MAXWELL. Primary electrons were uniformly distributed in the unit area 400$\mu$m above the substrate and the drift paths of electrons were calculated by the Monte Carlo method. The multiple scattering of drifting electrons in the gas is calculated by the MAGBOLTZ program [28] which works as a subprogram of the GARFIELD. The absolute multiplication factor $M_{\rm abs}$ was calculated by equation (2.3). Because the observed gas gain is determined by $M_{\rm eff}$ which includes a degradation of factor $R_{\rm eff}$, we focus on $M_{\rm eff}$ in the following discussion.

### Basic parameters

The geometrical parameters of the $\mu$-PIC used for the simulation are listed below, where $h$ is the height from the surface of the substrate.

1. Height of the anode electrode (variable; default = 10$\mu$m),
2. Width of the cathode strip (fixed; 314$\mu$m),
3. Diameter of the cathode openings (fixed; 260$\mu$m),

4. Substrate thickness $t$ (variable; default = 100$\mu$m),

5. Diameter of the anode electrode $d$ (variable; default = 50$\mu$m).

At first, we discuss the $R_{\rm eff}$ dependence on the anode height. Moreover, $M_{\rm eff}$ dependences on $t$ and $d$ are examined, in which we assume the anode height is 10$\mu$m above the surface of the substrate. These geometrical parameters of the $\mu$-PIC are described in Fig. 7.3. $D$ means the distance between the anode pillar and the cathode edge. The default value of $D$ is 105$\mu$m. The thickness of the cathode electrodes is fixed to 10$\mu$m for all calculations. The anode-cathode voltage was 600V and the drift electric field was 1kV/cm. The gas mixture was $Ar/C_2H_6$ (80/20).

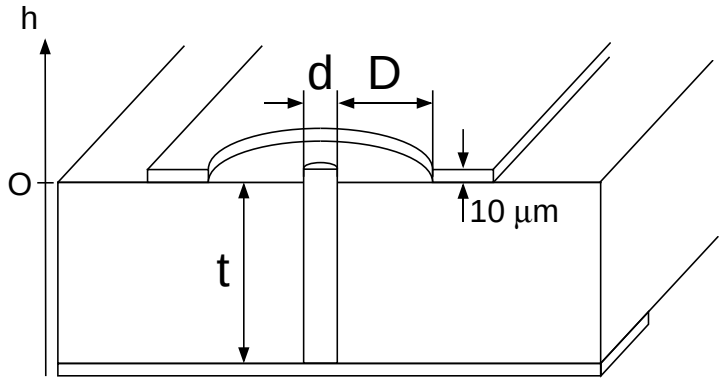


Figure 7.3: Description of the geometrical parameters of the $\mu$-PIC.

### 7.2.2 Simulation Result

**$R_{\rm eff}$ dependence on the anode height**

Firstly, we simulate the dependence of the electron collection on the anode height in order to clarify the problem of the $\mu$-PIC. The calculated drift lines of primary electrons are shown in Fig. 7.4 (a). This figure shows the cross-sectional view of the electrode structure. The left-half path of the figure are obtained by a numerical calculation using the Runge Kutta Fehlberg (RKF) method. Each drift lines calculated by this method traces the electric flux lines. The drift lines of right-half in the figure are the results simulated by

the Monte Carlo (MC) calculation. The deflection of the electron track due to the multiple scattering is included in the MC calculation. We found that some drift electrons terminate on the substrate. The distribution of the terminal points of drift electrons are also shown in Fig. 7.4 (b), where all drift electrons are calculated by the Monte Carlo method. The terminal points of the electron are roughly distributed along the anode readout electrode arranged on the rear side of the substrate. The terminal points are sorted into following three types:

1. collected by the anode electrodes and contributing to the signal (signal event),
2. terminated on the substrate between the anode and the cathode (near-anode event),
3. terminated on the substrate between two cathode strips (gap event).

The electron collection efficiency $R_{\rm eff}$ is defined as a fraction of type 1 events against the total event. In the $\mu$-PIC, $R_{\rm eff}$ was only about 30%. The dominant event was type 2 which accounts 65% of the total events. It means that the collected charge is only one third of a primary electron cloud. Therefore, observed pulse height is only 0.3 times of that expected by the Townsend coefficient.

We simulated the effect of the anode height in the range from 40$\mu$m below the substrate surface (the level of $\mu$-PIC2) to 10$\mu$m above the substrate (the level of $\mu$-PIC1). Fig. 7.5 presents the result of this simulation, where the fraction of type 1, 2, and 3 events are plotted as filled circles, triangles and squares, respectively. Obviously, the fraction of signal event increases with the raise of the anode level. Then the collection efficiency would become close to 90% if the top of the anode exceeds the surface of the substrate.

The electrode structure of the $\mu$-PIC with higher anodes was created in the MAXWELL and the drift paths of primary electrons were calculated by the GARFIELD. Because the gap between the cathode strips also attracts some of primary electrons [37], the gap was reduced from 86$\mu$m to 40$\mu$m in order to obtain high collection efficiency. Fig. 7.6 (a) shows the resultant drift lines of the primary electrons. Obviously almost all electrons are collected by the anode electrodes. This is also shown in Fig. 7.6 (b), which shows the distribution of the terminal points of the primary electrons. The electron collection efficiency was attained to 97%.

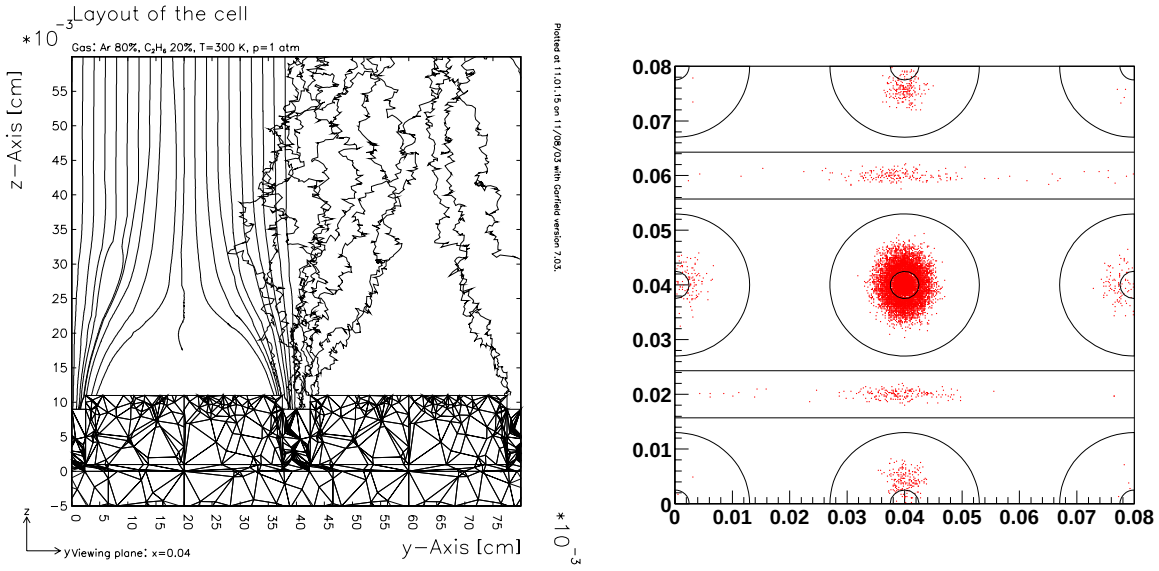


(a) (b)

Figure 7.4: Electron drift of the $\mu$-PIC with lower anode. (a)Cross-sectional view of electron drift. The paths of left-half are calculated by the Runge Kutta Fehlberg method. The drift lines of right-half are simulated by the Monte Carlo method. (b)Distribution of the terminal points of electron drifts.

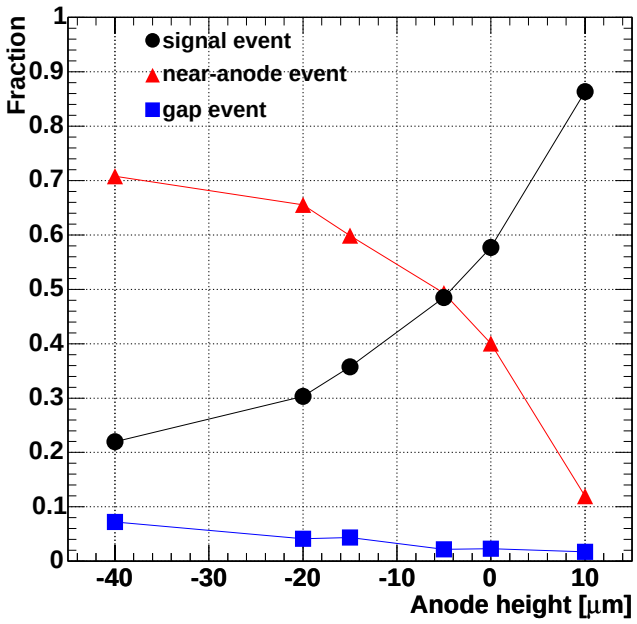


Figure 7.5: Relation between electron collection efficiency and anode height. The filled circles mean the electron collection efficiency. The filled squares and the filled triangles mean the inefficiency.

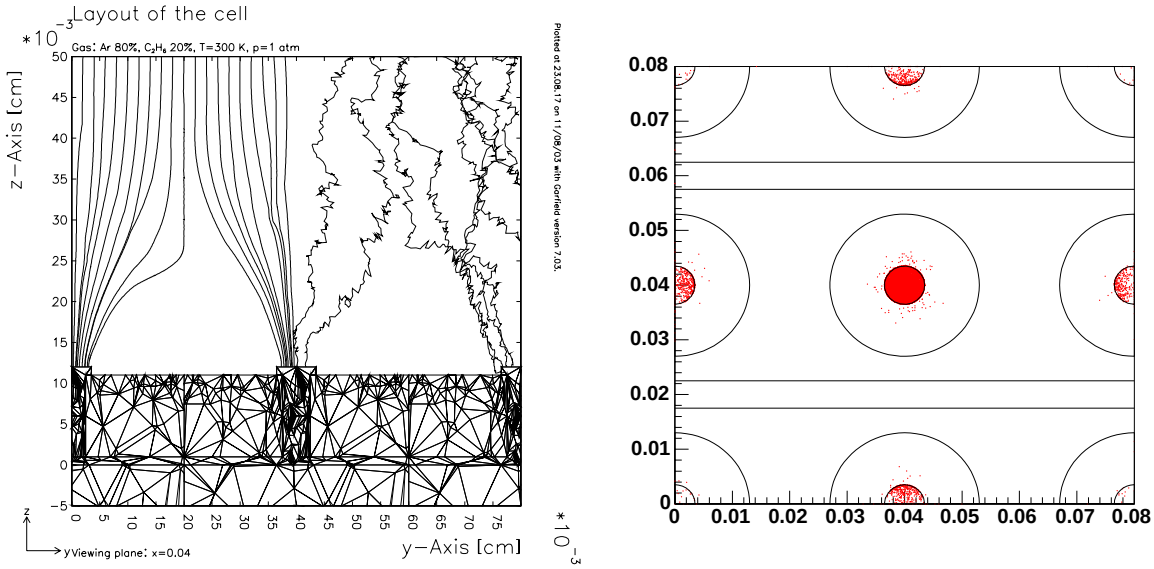


(a) (b)

Figure 7.6: Drift lines of primary electrons and their terminal points of the electron for the $\mu$-PIC with higher anodes. (a) Cross-sectional view of them. The paths of left-half are calculated by the Runge Kutta Fehlberg method. The drift lines of right-half are simulated by the Monte Carlo method. (b) Distribution of the terminal points of electron drifts.

### $M_{\rm eff}$ dependence on the substrate thickness

Pixel-type gas detectors developed prior to $\mu$-PIC were made by the IC technology, and hence had a very thin insulator layer (several $\mu$m). Therefore, the electric field in the drift region near the surface of the substrate is affected by the readout strips buried in the insulator. Some of the drift electrons would be directed toward the readout buses, rather than the anode electrodes as shown in Fig. 7.7. This effect would be observed as a degra-

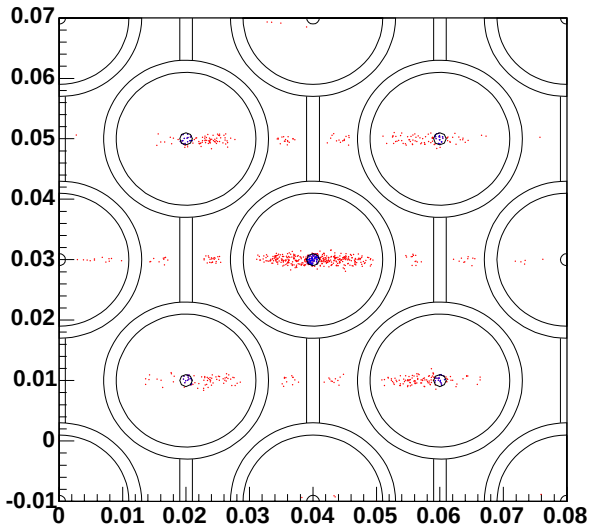


Figure 7.7: Terminal points of drift electrons for a MDOT detector.

dation of the gas gain, or small $R_{\rm eff}$ values. Furthermore, the accumulated charge on the substrate might cause serious discharges. There are two approaches to avoid this problem. The first is to make a narrow-pitch detectors [55]. Actually, a narrow pitch ($< 100\mu$m) MDOT detector was reported to have overcome this problem. Because discharges could be problematic with the small anode-cathode distance, we adopted the other approach; a thick substrate. This approach was only realized with the PCB technology, and hence $\mu$-PIC has its outstanding features in its thick substrate.

As described above, efficient electron collection is expected for the higher anode electrodes. In order to evaluate the effect of the substrate thickness quantitatively, we use

the $\mu$-PIC structure having the anode pillar of 10$\mu$m above the surface of the substrate.

Figs. 7.8 and 7.9 show the drift lines of primary electrons and the distribution of their terminal points. where the results of the thin ($t = 5\mu$m) and thick ($t = 200\mu$m) substrates are shown in (a)s and (b)s, respectively. For $t = 5\mu$m, some of the drift lines end at the substrate (Fig. 7.8 (a)) and the resultant electrons are terminated on the substrate (Fig. 7.9 (a)). It was obvious that the buried anode readout buses distorted the drift electric field for $t = 5\mu$m, because the electron end points are distributed above the anode strips which are placed orthogonally to the cathode strips. On the other hand, most of the electrons are collected to the anode electrodes for $t = 200\mu$m. Fig. 7.10

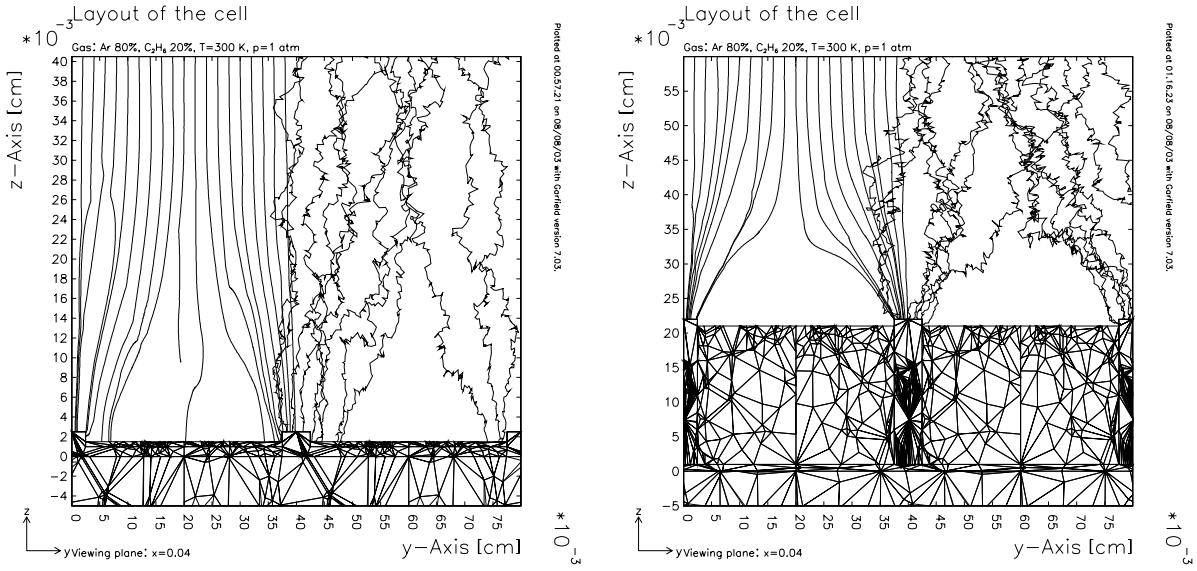


(a) (b)

Figure 7.8: Simulated drift lines of primary electrons for (a) $t = 5\mu$m, and (b) $t = 200\mu$m. In both figures, the drift lines drawn in the left half were calculated by the RKF method; those in the right half were simulated by the MC method.

shows the $R_{\rm eff}$ dependence on $t$. For a thin ($t < 10\mu$m) substrate, $R_{\rm eff}$ was found to be less than 0.5, while that with a thick ($t > 100\mu$m) substrate exceeds 0.8.

Another parameter which determines $M_{\rm eff}$ is $M_{\rm abs}$. Because $M_{\rm abs}$ strongly depends on the electric field around the anode electrodes, $M_{\rm abs}$ also depends on $t$. Fig. 7.11

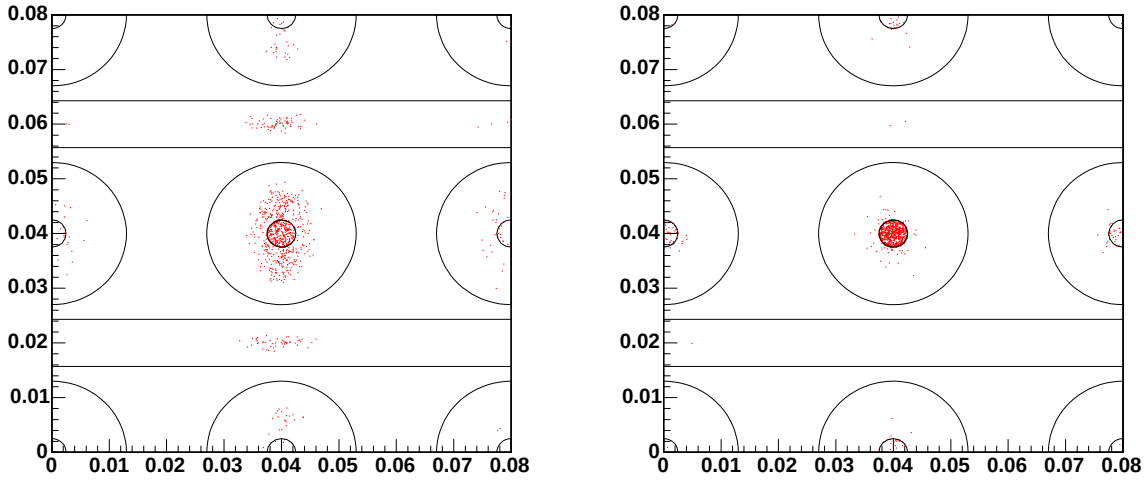


(a) (b)

Figure 7.9: Terminal points of electrons on the electrode plane of the $\mu$-PIC of (a) $t = 5\mu$m, and (b) $t = 200\mu$m. 1000 events are shown in both cases.

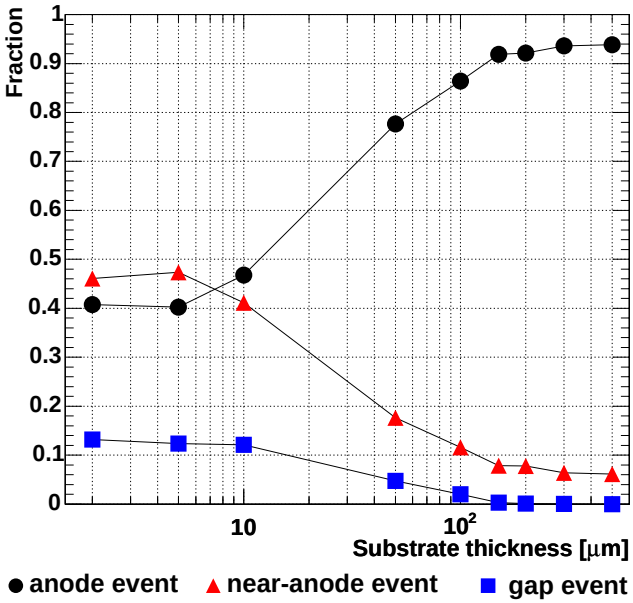


Figure 7.10: Electron collection efficiency dependence on $t$ (filled circles). For reference, fractions of electrons that are terminated on the substrate in the cathode openings and the gaps between the cathodes are shown by the triangles and squares, respectively.

(a) shows the electric fields as a function of the distance $r$ from the anode center at $h = 11\mu$m. With a thin ($t = 5\mu$m) substrate, the electric field averaged over the top area of the anode electrodes (hereafter $E_a$) reaches only 60kV/cm, while that with a thick ($t > 100\mu$m) substrate exceeds 120kV/cm. Because $M_{abs}$ strongly depends on $E_a$, a thick substrate is important for large $M_{abs}$ value. The electric fields near the surface of the substrate ($h = 1\mu$m) are also shown in Fig. 7.11 (b) as a function of $r$. The electric field averaged along the circumference of the cathode edge (hereafter $E_c$) is found to be 10 times stronger for thin ($t = 5\mu$m) substrate than that for a thick ($t > 100\mu$m) substrate. Hence, the Townsend coefficient for a thin substrate becomes larger near the cathode edge, which is likely to cause discharges due to the emission of electrons from the cathode electrode, which may be attributed to that the distance between the cathode edge and the anode readout bus ($t$) is much shorter than the distance between the anode pillar and the cathode edge ($D$). On the other hand, if $t$ is larger than $D$, the effect of the readout

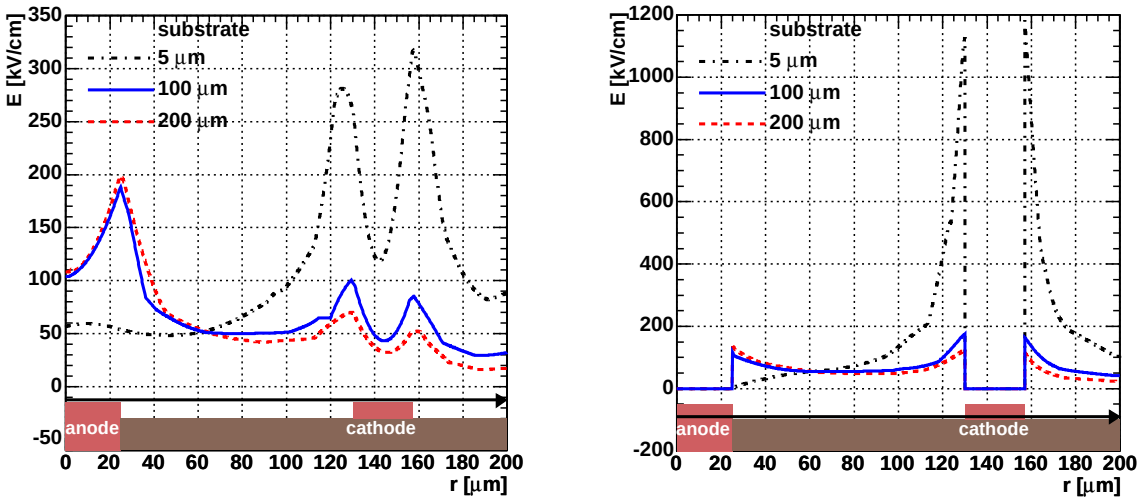


Figure 7.11: Strength of the electric field as a function of the distance from the anode center: (a) the $r$ axis is located 1$\mu$m higher above the top of the anode electrodes. (b) the $r$ axis is located 1$\mu$m higher above the substrate.

bus is efficiently shielded by the substrate, and the $E_c$ was weaker than the $E_a$. $E_a$ and $E_c$ for various $t$ values are shown in Fig. 7.12. It is intuitively expected that $E_c$ should be at least weaker than $E_a$ though the mechanism of discharges will be discussed in later section. Because $E_a$ is comparable to $E_c$ with $t \sim 100\mu$m, thickness of the substrate of the present $\mu$-PIC is thought to satisfy the minimum point, though it is not still sufficient. Thicker substrate ($t \gtrsim 150\mu$m) would help to realize larger $M_{abs}$ with the $\mu$-PIC.

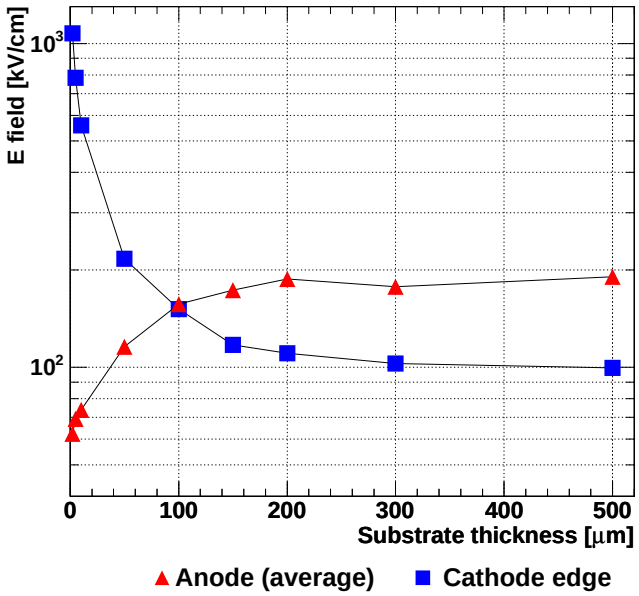


Figure 7.12: Strength of the electric field at the center of an anode pixel (triangle), and near to the cathode edge (square) as a function of the substrate thickness.

As a consequence of these two studies, thicker substrate gives larger $M_{eff}$. Fig. 7.13 shows $M_{eff}$ as a function of $t$. With a substrate thicker than $150\mu$m, $M_{eff}$ is expected to be twice larger than the current $\mu$-PIC.

**Scaling parameter;** *TDR*

When we discuss the the dependence of performances on the substrate thickness for detectors having various geometrical parameters, it is useful to introduce a general geo-

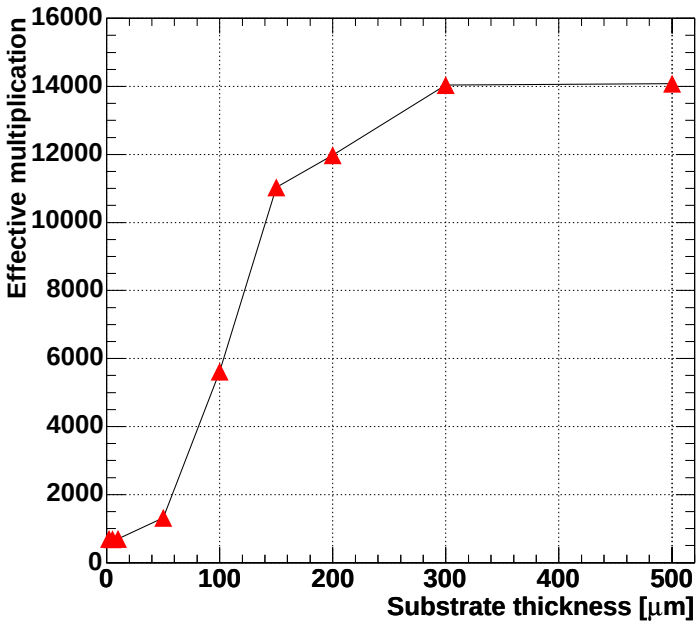


Figure 7.13: Calculated effective multiplication $M_{\rm eff}$ as a faction of the substrate thickness.

metrical parameter. We define a new parameter, the "*thickness-distance ratio* ($TDR$)"; $TDR = t/D$, where $t$ and $D$ are the substrate thickness and the distance between the anode and the cathode, respectively as shown in Fig. 7.3. The default values of $D$ and $t$ are 105$\mu$m and 100$\mu$m, respectively. This new parameter have to be checked its reliability. For this purpose, the geometrical parameters $d$, $t$, and $D$ were varied within a reasonable range. The structures similar to the original $\mu$-PIC ($TDR \approx 1$) was emulated with the scale factors of 0.5, 1.5, and 2.0, as well as the default value. The voltage between the anode and the cathode was also varied with the scale factor so that the electric field at the anode center becomes about 100kV/cm for all scale factors. The electron collection efficiencies were calculated for each structure, which is shown in Fig. 7.14. Roughly constant values were obtained with the variation of 10%. Also the same calculations were carried out varying $TDR$. Fig. 7.15 shows the variation of $R_{\rm eff}$ as a function of $TDR$ for the scaling factor of 0.5, 1.0, 1.5, and 2.0. In the case of large $TDR$ ($\gtrsim 1.0$), $R_{\rm eff}$ was regarded as constant for several scaling factors. However, while $TDR$ becomes smaller, significant difference of the calculated $R_{\rm eff}$ was found for larger scaling factors. Consequently, this results mean that the $TDR$ parameter is useful for the evaluation of the electrode structure of which size is sub-mm level.

### $M_{\rm eff}$ dependence on the anode diameter

The dependences of the $R_{\rm eff}$ and $M_{\rm abs}$ on the anode diameter ($d$) were also studied. Although the current technology can manufacture only anode electrodes with a diameter larger than 50$\mu$m, it is worth to investigate the optimum diameter. Fig. 7.16 shows $E_{\rm a}$ as a function of $d$. Obviously, $E_{\rm a}$ decreases with increasing $d$. On the other hand, large $R_{\rm eff}$ is expected for the large $d$, as shown in Fig. 7.17. Fig. 7.18 shows the effective multiplication factor $M_{\rm eff}$ as a function of $d$. As is well known, this result shows that a smaller $d$ 20-30$\mu$m has a larger gain, however, it also indicates that a sufficient multiplication is expected for an $d \sim 50\mu$m.

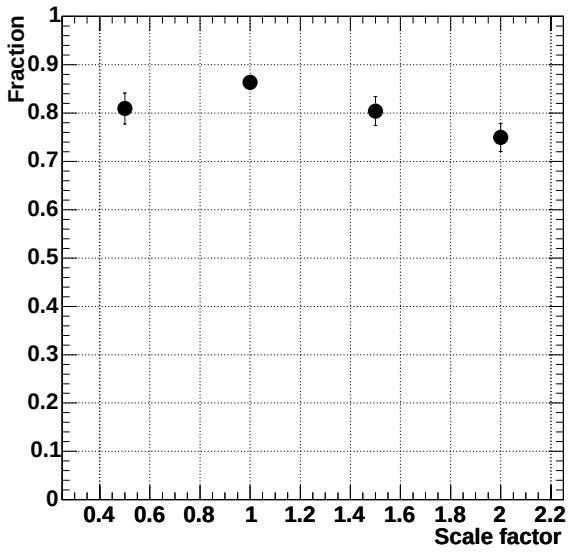


Figure 7.14: The electron collection efficiency as a function of the scale factor. The scale factor = 1 is the default value of $d$, $t$, and $D$.

## 7.3 Detector optimization

### 7.3.1 μ-PIC with a thick substrate

In the previous section, we showed that the thicker substrate and smaller diameter of the anode electrode would help to improve the performance of the μ-PIC. Because smaller anode electrodes are technically unreachable in the PCB technology, we evaluated the maximum $M_{\rm eff}$ of the μ-PIC with a thick substrate considering the maximum anode voltage for stable operation.

As indicated in earlier works about MSGCs [46, 47, 56], the dominant mechanism of discharges in micro-pattern gas detectors is a consequence of the ejection of electrons from the cathode edge by spontaneous field emission. At a normal operation condition of MSGCs, the electric field near the cathode edge exceeds 100kV/cm, which is high enough for a gas avalanche [46]. Electrons released from the cathode electrodes undergoes the gas multiplication near both the cathode and anode electrodes, while the primary electrons have gas multiplication only near the anode electrode. We can assume that the electric

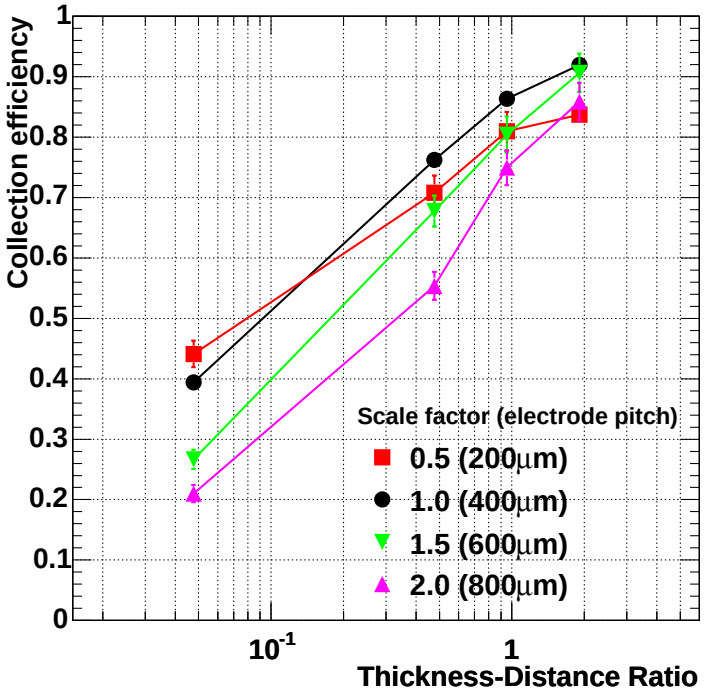


Figure 7.15: Dependence of the electron collection efficiency on *TDR* for the scale factors of 0.5 (square), 1.0 (filled circle), 1.5 (inverse triangle), and 2.0 (triangle). The corresponding electrode pitches are also shown.

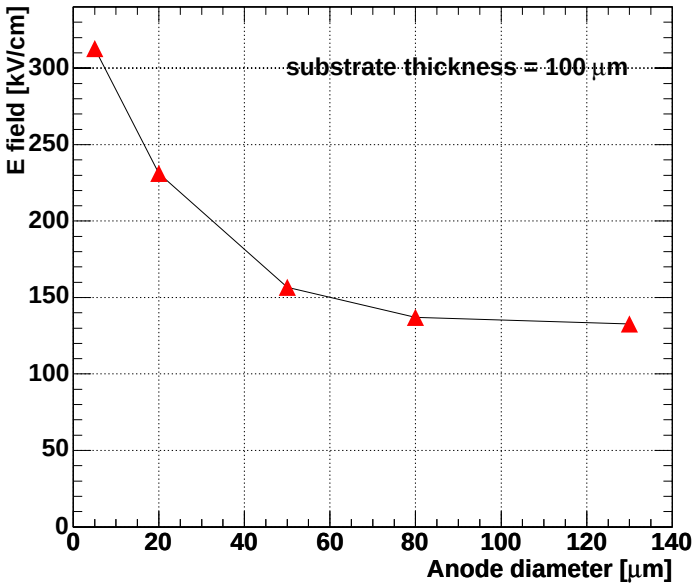


Figure 7.16: Electric field at the anode pixel as the function of the anode diameter.

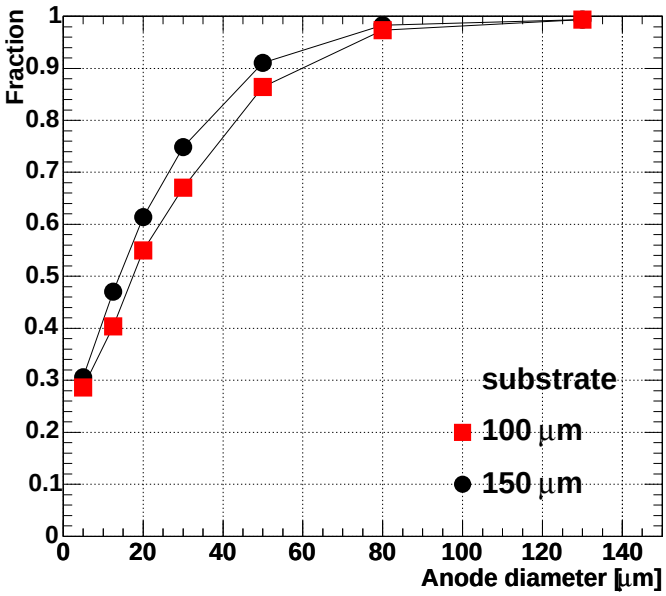


Figure 7.17: Electron collection efficiency as a function of the anode diameter.

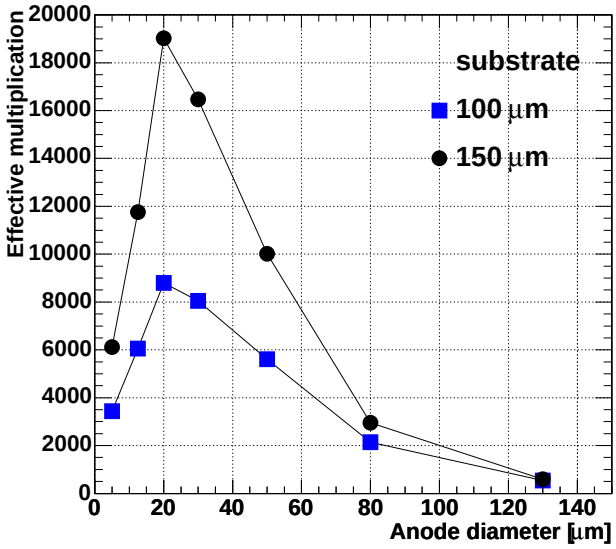


Figure 7.18: Dependence of the effective multiplication factor as a function of the anode diameter.

field near the cathode governs the discharge process and "stable operation" can be judged by the cathode field. It is natural to think this discharge mechanism can be applied to $\mu$-PIC, and we can estimate the possibly maximum anode voltage and $M_{\rm eff}$ before discharges starting by the cathode field $E_{\rm c}$.

From the experimental results (Sec. 6.1), we knew that the attainable anode voltage before discharges was about 630V, which corresponds to the maximum $E_{\rm c}$ of 200kV/cm. Here 200kV/cm is used as the limit of $E_{\rm c}$. As mentioned in the previous section, $E_{\rm c}$ becomes weaker for a large $TDR$ with the same anode voltage. In other words, the corresponding voltage $V_{\rm lim}$ becomes higher for a larger $t$. In Fig. 7.19, $V_{\rm lim}$ and corresponding $M_{\rm eff}$ are shown as a function of $TDR$. For a thicker substrate of $TDR > 1.5$, maximum anode voltage exceeds 800V, of which the maximum gas multiplication for that voltage is higher than $10^6$, as shown in Fig. 7.19. Taking into account other factors which cause discharges such as roughness of the cathode surface, the gas gain might achieve $10^5$ for a 150$\mu$m thick substrate. Thus, geometrical structures of $\mu$-PIC or other pixel-type detector are thought to be optimized by increasing $TDR$.

### 7.3.2 Substrate-ablated $\mu$-PIC

As discussed above, a thick substrate is thought to drastically improve the performance of the $\mu$-PIC. However, it would be technically difficult to form an anode pillar through a thick substrate especially in case $t/d \gg 1$. Even though we make a $\mu$-PIC with a thick substrate, if the anode pillar is lower the surface of the substrate, $R_{\rm eff}$ becomes small and we don't achieve large $M_{\rm eff}$. One of the solutions to retain large $M_{\rm eff}$ with a low anode pillar is to ablate the substrate by a physical or a chemical process, e.g. laser machining. Fig. 7.20 shows the structure of the $\mu$-PIC with an ablated substrate ("*well-type* $\mu$-PIC") created by the Maxwell program. We simulated the performance of this type $\mu$-PIC for several anode height between $h = -40\mu$m to $h = 0\mu$m. All parameters except the cathode width (340$\mu$m) were set to the default values. A wider cathode is used to improve $R_{\rm eff}$. Fig. 7.21 shows the simulated electron terminal points for anode height at $h = -20\mu$m. Calculated $R_{\rm eff}$ was more than 99% for all the anode height. The absolute gas multiplication $M_{\rm abs}$ depends on the anode height, as shown in Fig. 7.22.

We manufactured a prototype of the well-type $\mu$-PIC. The substrate around the anode

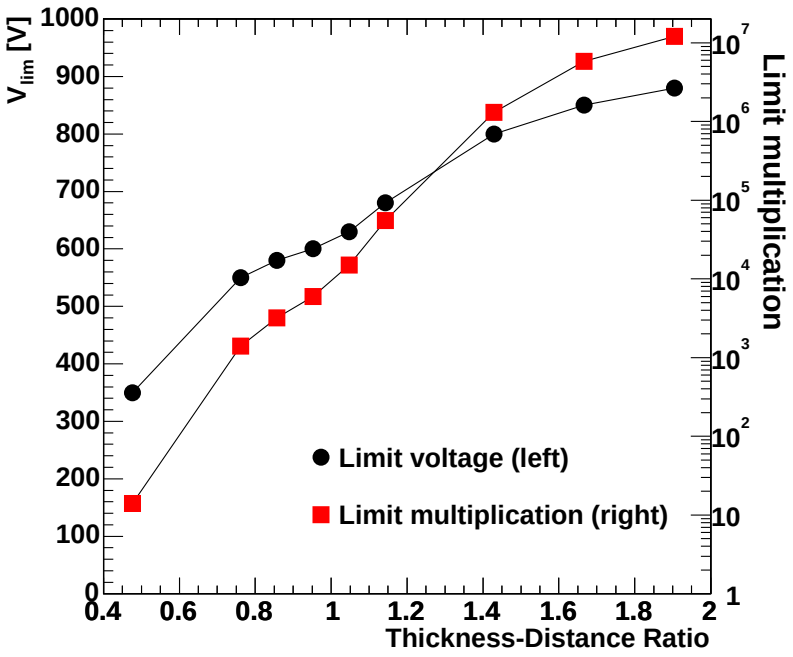


Figure 7.19: Dependence of the limit voltage (filled circle) and the corresponding achievable gas gain (filled square) as a function of the *Thickness-Distance Ratio*.

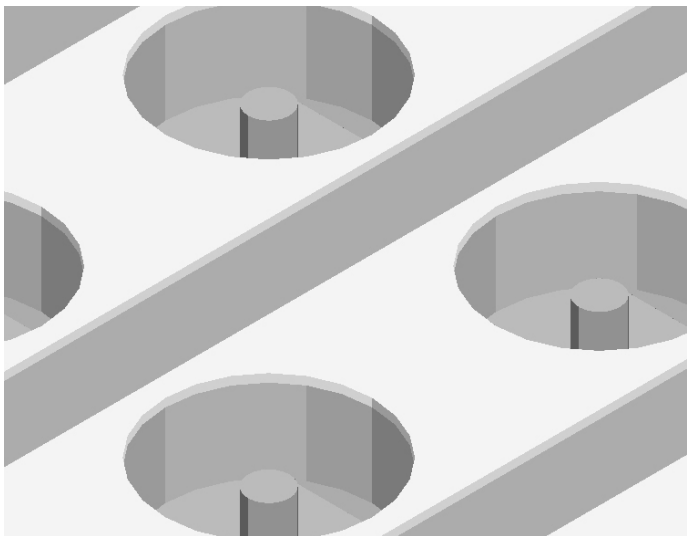

Figure 7.20: Substrate-ablated $\mu$-PIC.

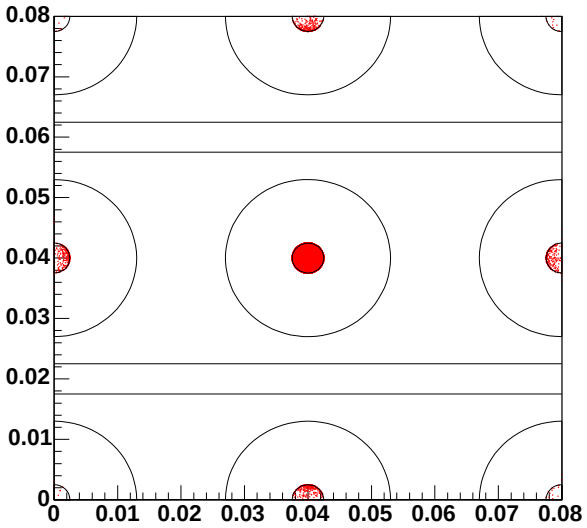


Figure 7.21: Distribution of drift terminal points of electrons for the well-type μ-PIC.

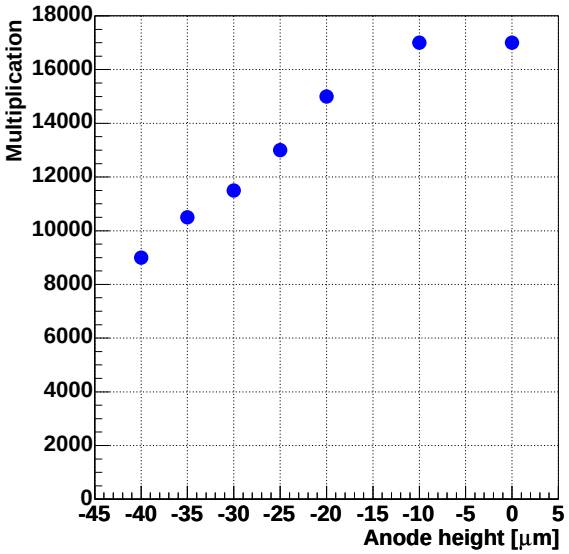


Figure 7.22: Simulated absolute gas multiplication as a function of the anode height for the well-type μ-PIC.

was ablated by a laser treatment, as shown in Fig. 7.23. The anode electrodes remained

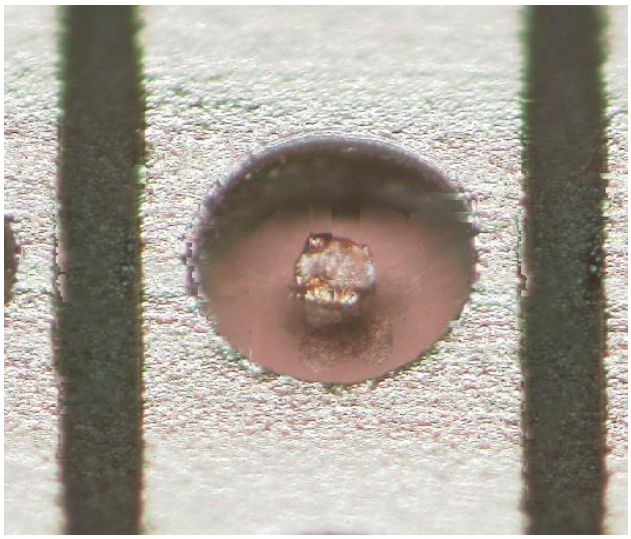

Figure 7.23: Microscopic photograph of the well-type $\mu$-PIC.

on the readout strip electrodes like pillars. Fig. 7.24 shows the measured gas gains of the well-type $\mu$-PIC. Measured gas gains are smaller than those of previous $\mu$-PIC because we ablated the substrate of the $\mu$-PIC whose anode height are lower than $h = -20\mu$m. The detector became unstable by discharges when the gas gain exceeded $10^3$. Although the reason for the discharges is not very clear, we have some hypotheses, e.g. the shape of the ablated well, and a distortion of the top shape of the anode pillars that occurred during the ablation process. For these reasons, the electric field might become locally strong, and then discharge paths could easily be formed between the cathode edge and the anode strip. A simulation shows that a slightly smaller diameter of the well than the cathode ring is much better for discharges. However, at present, it looks quite difficult to control the ablation process with the required accuracy for a large area detector. We will try this type detector when the new technology becomes available.

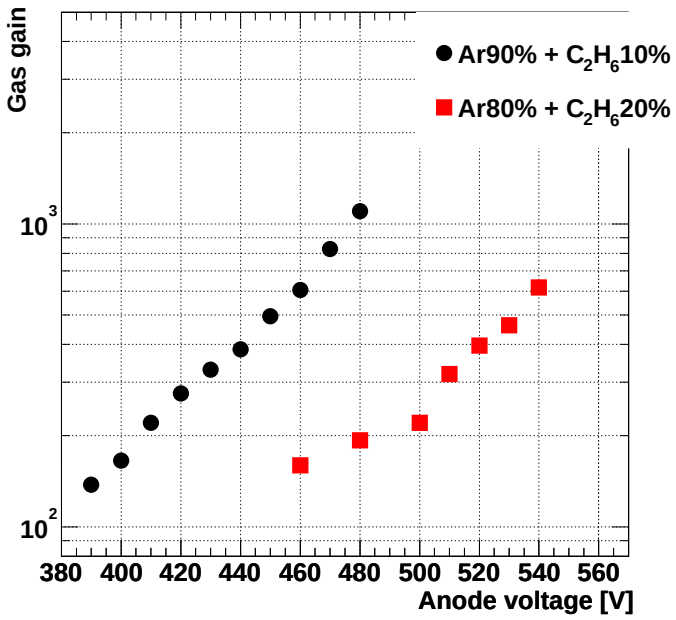


Figure 7.24: Gas gain curve of the well-type $\mu$-PIC.

## 7.4 Development of the improved $\mu$-PIC

The conventional electroplating technology looked very difficult to control the growth of the anode in such a fine level. Then we applied the new manufacturing technology, which is a combination of the chemical (electroless) plating and electric plating. Using this new technique, a $\mu$-PIC was manufactured as follows (see also Fig. 7.25). First, a thin copper layer is formed on the all surface of the laser-drilled 100$\mu$m thick substrate using electroless plating. Via holes are filled over the surface, and a thick copper layer is formed by electric plating (via-fill plating). A copper surface is etched until its thickness is reduced to $\sim 10\mu$m. Finally, both anode and cathode electrodes are formed by etching simultaneously, and hence the anode height (10$\mu$m) is quite same as that of the cathode surface. The gaps between cathode strips is also formed by etching together with the anode pixels. Cathode material is not lost in this process whereas cathode strips of the previous $\mu$-PIC were slightly dissolved in the plating process. Then a narrow gap of 60$\mu$m was realized. Other geometrical parameters are summarized in Table 7.1. A microscopic photograph and a schematic drawing are shown in Fig. 7.26 together with those of the previous $\mu$-PIC. This new $\mu$-PIC having the detection area of $10 \times 10\text{cm}^2$ was named "$\mu$-PIC8". Very precise processing is possible for the etching technique. It allows us to make almost uniform electrodes. The deviation of the anode height was within 3$\mu$m in whole detection area ($10 \times 10\text{cm}^2$). Furthermore, there was almost no abnormal anode formation; the fraction was less than 0.1%. This technique can be applied for larger area detectors because the uniform electrodes was achieved in $10 \times 10\text{cm}^2$.

| | Parameter | value |
|---|---|---|
| Anode | height | 10$\mu$m |
| | diameter | $\sim 50\mu$m |
| Cathode | width | 340$\mu$m |
| | hole diameter | 260$\mu$m |
| | thickness | 10$\mu$m |
| Substrate | thickness | 100$\mu$m |

Table 7.1: Geometrical parameters of the new $\mu$-PIC.

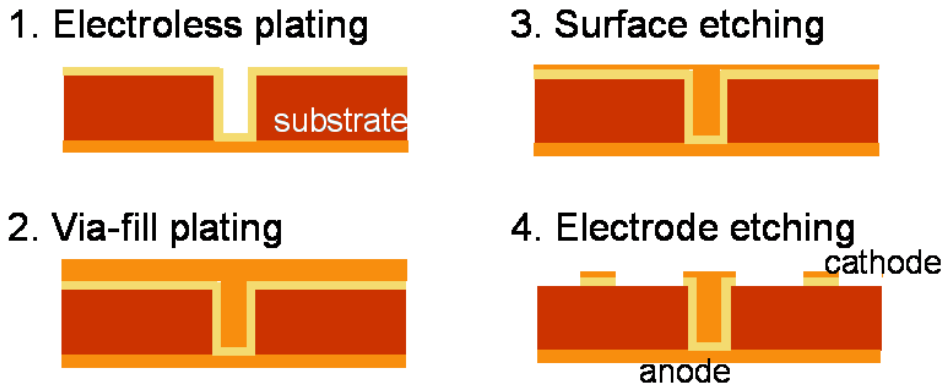


Figure 7.25: Manufacture process of the latest μ-PIC

.

We succeeded to form nine μ-PIC patterns on one large polyimide substrate in one manufacturing process as shown in Fig. 7.27. Now systematic shift of the anode position is observed as shown in Fig. 7.28. The offset increases with the distance from the center. This systematic shift is attributed to the difference of the thermal expansion between polyimide and copper. If the position of via holes are corrected before the manufacture process by estimation of this difference, the accurate electrodes will be realized and a larger area ($30 \times 30\text{cm}^2$) μ-PIC can be made.

## 7.5 Performance test

### 7.5.1 Basic performance

The basic performances of μ-PIC8 were tested. The conditions of the experiment were all the same as those of the previous μ-PICs described in chapter 6. The obtained gas gains were plotted in Fig. 7.29 by filled circles together with the gas gain curve of the previous μ-PIC. Obviously, the gas gains of the new μ-PIC were three times higher than those of the previous μ-PIC. This difference can be explained by the effect of the higher anode of the new μ-PIC. This result shows that most of the primary electrons due to the incident particle are collected by the anode electrodes. In other words, the electron

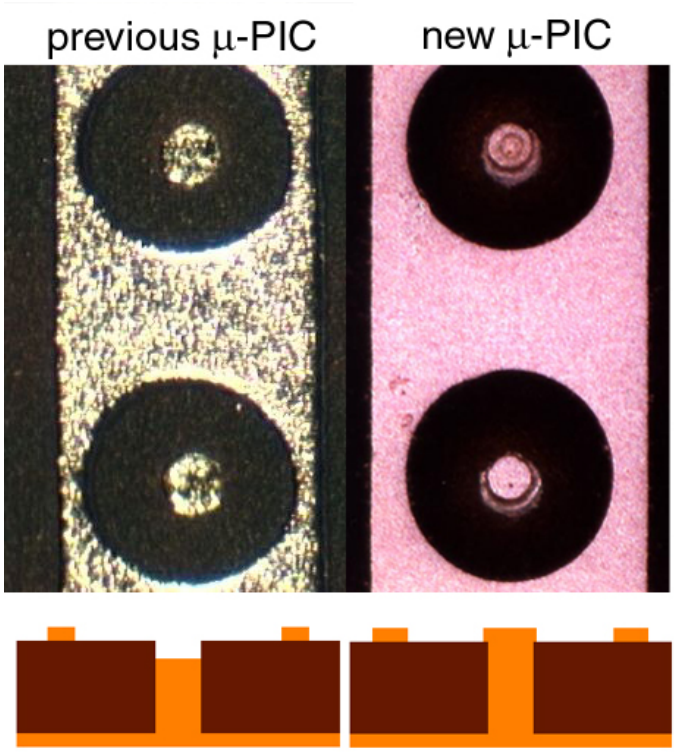


Figure 7.26: Microscopic photograph and schematic cross section of the previous $\mu$-PIC (left) and the new $\mu$-PIC (right).

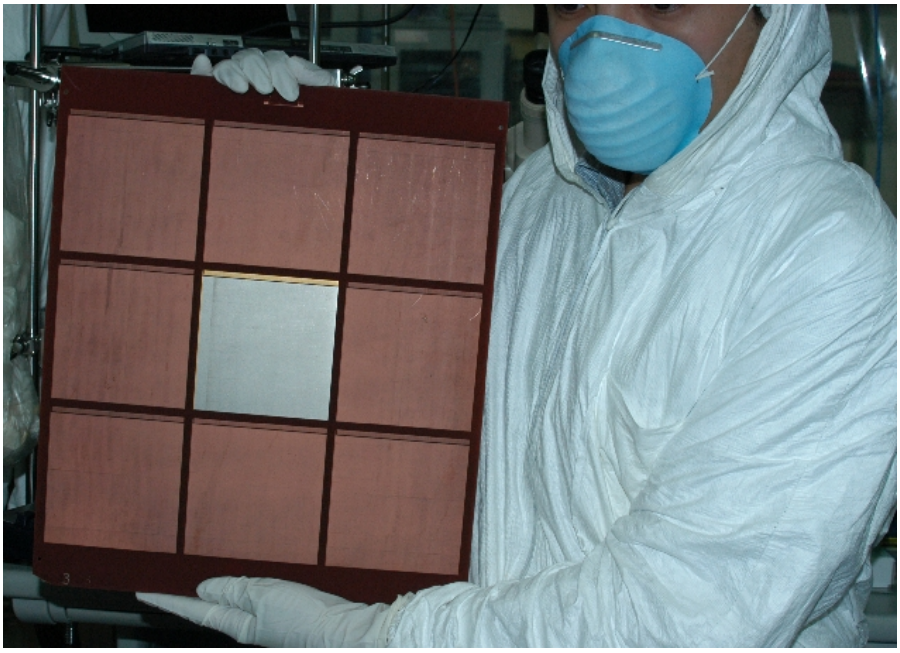

Figure 7.27: Photograph of a substrate board formed nine $\mu$-PIC patterns. Each square is a $\mu$-PIC pattern. The center one is plated by nickel, and the other are not coated.

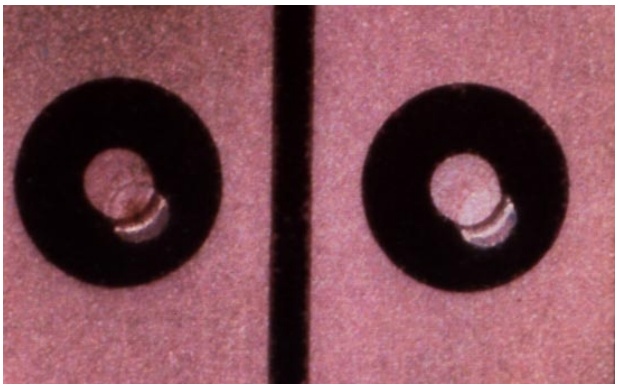

Figure 7.28: Microscopic photograph of shifted anodes observed in edge region.

collection efficiency was close to 100%.

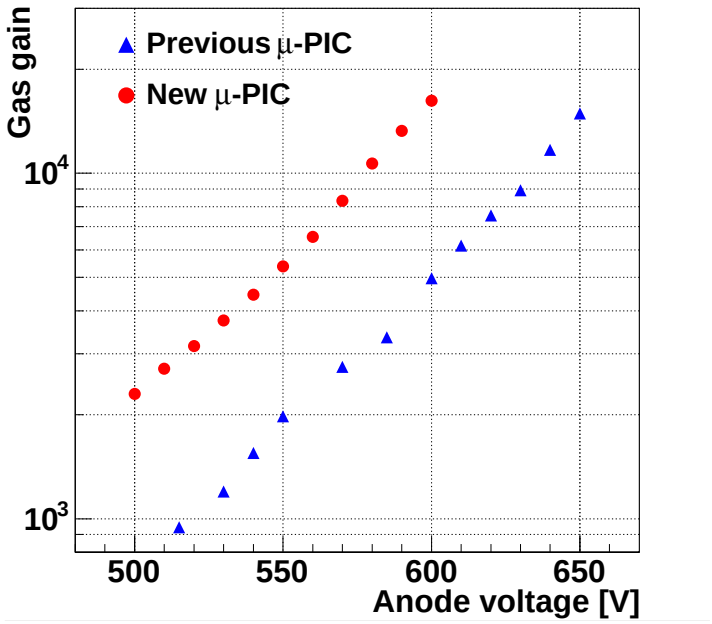


Figure 7.29: Gas gain curve of the new $\mu$-PIC (square) and the previous $\mu$-PIC (circle).

The energy spectrum was measured using 5.9keV X-ray from an $^{55}$Fe source. Fig. 7.30 (a) shows the spectrum obtained from the detection area of $12.8 \times 12.8\text{mm}^2$. An escape peak is clearly seen at 2.7keV as well as the main peak of 5.9keV. Achieved energy resolution of this area was about 23% (FWHM). Fig. 7.30 (b) also shows the spectrum from whole detection area ($100 \times 100\text{mm}^2$). Although the spectrum from whole detection area was somewhat broadened, the energy resolution of 30% (FWHM) was kept.

Dependence of the gas gain on the detection position was also measured using an $^{55}$Fe source. The detection area was divided into $8 \times 8$ segments and gas gains were measured in each segment which has $32 \times 32$ pixels. Fig. 7.31 shows the map of the measured gas gain of the full detection area. The standard deviation of the gas gain distribution was only 7%. The uniformity of the gas gain was drastically improved compared to that of the previous $\mu$-PIC as shown in Fig. 7.32.

The feedback of the positive ions generated in the avalanche is measured using an

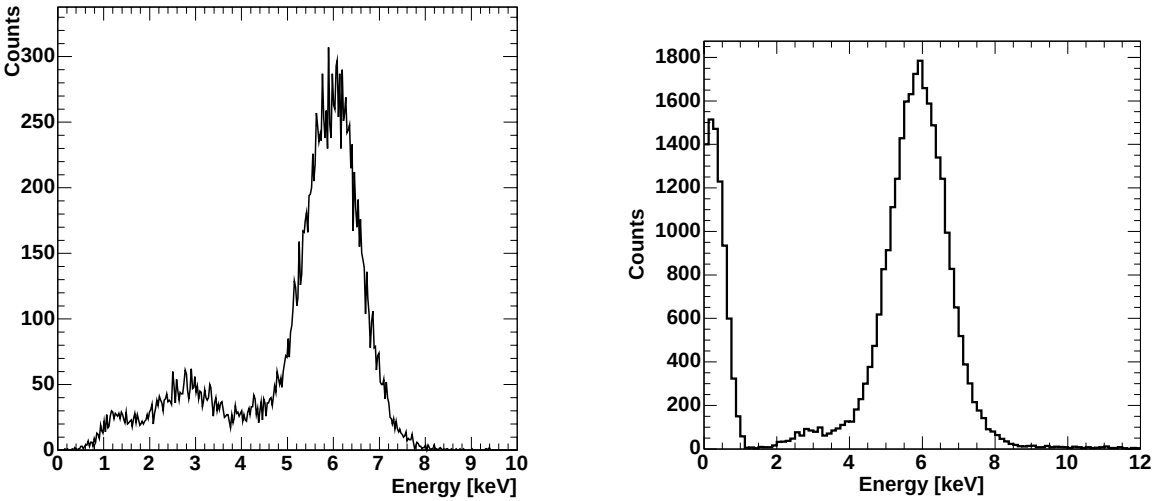


(a) (b)

Figure 7.30: Energy spectrum obtained from the detection area of (a) $12.8 \times 12.8\text{mm}^2$ and (b) $100 \times 100\text{mm}^2$ by irradiating the $^{55}$Fe source.

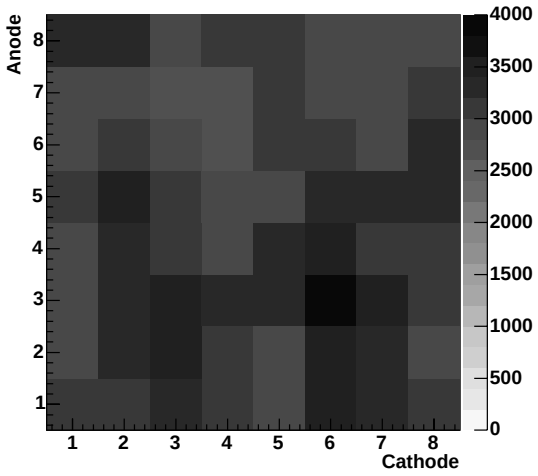


Figure 7.31: Map of the measured gas gains.

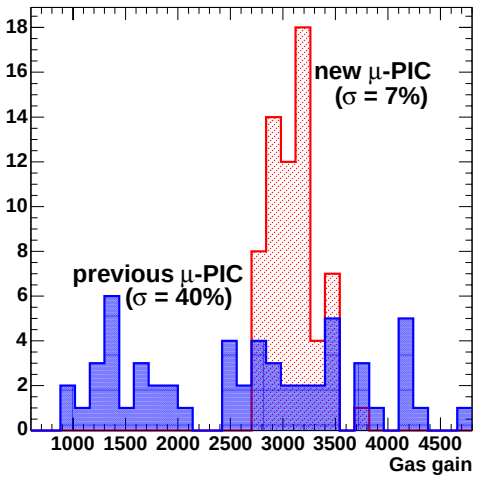


Figure 7.32: Gas gain distribution of the previous and the new $\mu$-PIC.

X-ray generator. In order to compare the result to the previous $\mu$-PIC, the setup of the X-ray generator was same as those of the previous one. Fig. 7.33 shows the anode and the drift current of the previous and the new $\mu$-PICs as a function of X-ray counting rate per unit area. As a result, the observed feedback current was about 1/3 of the anode current which correspond to the total collected charge. It was almost similar to that of the previous $\mu$-PIC. Furthermore, this current was independent on the X-ray counting rate (Fig. 7.34).

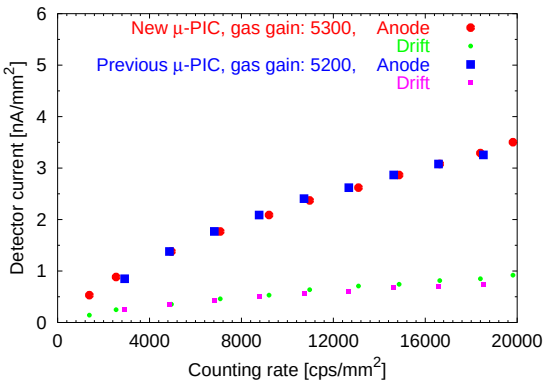


Figure 7.33: Anode and drift current as a function of the counting rate of X-ray.

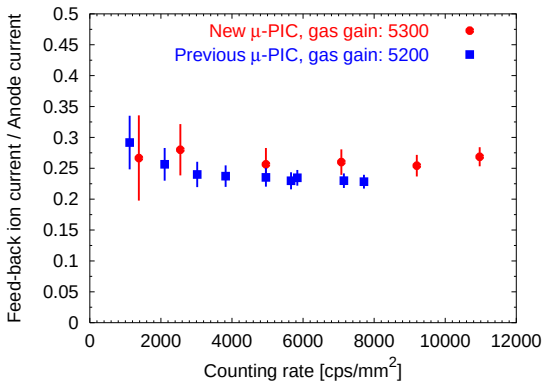


Figure 7.34: Fraction of the feedback current to the anode current.

### 7.5.2 Long term operation

Long term operation more than 1000 hours was also examined for the new $\mu$-PIC at the gas gain of $> 6000$. Fig. 7.35 shows the variation of the gas gain during 150 hours (corresponding to 6.25 days). As described in Sec. 6.2, almost constant gas gain for long term is expected, because the accumulation of electron on the substrate is smaller than that of the previous $\mu$-PICs. Actually, a slight increase of the gas gain was observed also for the $\mu$-PIC8. The variation from the initial gas gain was within 15%, which is about half of that of $\mu$-PIC4. It is considered that this small increase expresses a variation of the gas temperature.

The increase of gas gain in a few months was also observed in the new $\mu$-PIC. The gas gain became about 1.5 times higher during 2 months as shown in Fig. 7.36. The

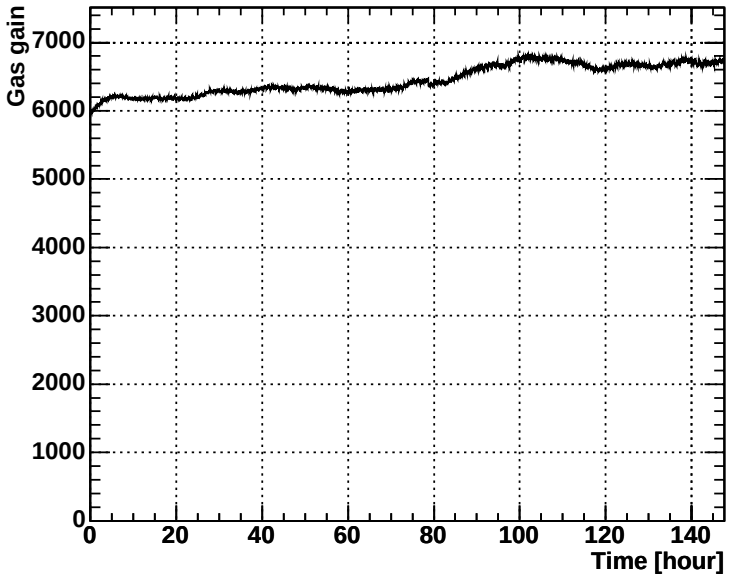


Figure 7.35: Variation of the gas gain in 150 hours.

resultant gas gain of $1.6 \times 10^4$ was achieved. This gain increase can be explained as water contamination as well as the previous $\mu$-PIC, because the new $\mu$-PIC is made of the same material as the previous one.

The obtained basic performances are summarized and compared with those of the previous $\mu$-PIC in table 7.2. Most properties were improved for the new $\mu$-PIC.

| | Previous $\mu$-PIC | New $\mu$-PIC |
|---|---|---|
| Max gas gain | $1.5 \times 10^4$ | $> 1.6 \times 10^4$ |
| Stable gas gain | $\sim$3000 | $\sim$6000 |
| Energy resolution (FWHM) | 30% | 23% |
| Gain uniformity ($\sigma$) | 40% | 7% |
| Feedback fraction | 1/3 | 1/3 |

Table 7.2: Performance comparison of the previous and the new $\mu$-PIC.

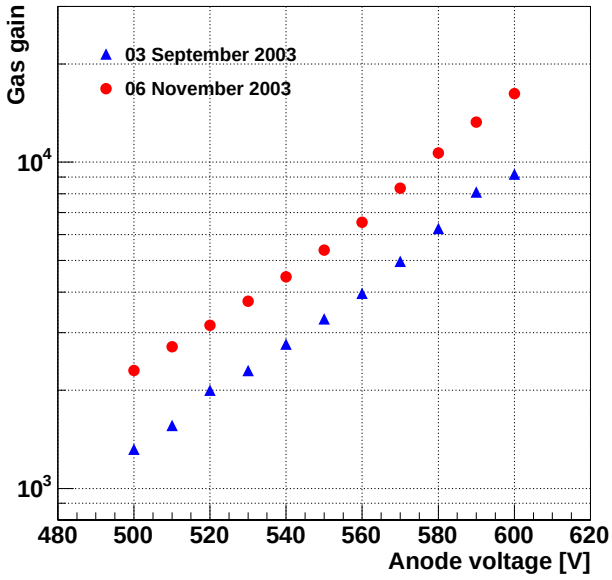


Figure 7.36: Variation of the gas gain in two months.

# Chapter 8

# Imaging and 3D tracking

All applications of the $\mu$-PIC is based on the two-dimensional imaging. Imaging of X-rays or charged particles is the most interesting feature of the $\mu$-PIC. Here, we describe about the capabilities of X-ray imaging, and three-dimensional tracking of charged particles in the use of Time Projection Chamber.

## 8.1 X-ray imaging

The $\mu$-PIC has narrowly spaced electrodes, which provide the spatial resolution of about 100$\mu$m by a digital readout DAQ system. The DAQ system operates with the clock of 20 or 40MHz, then real-time imaging is obtained in principle, which contains $\sim 10^6$ data per second. Then a high-quality moving image can be taken like a CCD-based detector. Furthermore, energy information is also available as well as the position and timing information. That will establish a new technique of imaging.

We evaluated the performances of X-ray imaging using a standard test chart for X-ray imaging. The test chart is made of 0.05mm thick lead with the slits of various width. We used an X-ray generator with the acceleration voltage of 12kV, which was set at a distance of 35cm from the drift electrode of the $\mu$-PIC. Irradiation at the surface of the detector is expected to be uniform at this distance. A 1mm thick aluminum plate was used for filtering of low energy X-rays ($\lesssim$5keV). In order to obtain a clear image, we used the gas mixture of $Xe/C_2H_6$ (70 / 30) at atmospheric pressure, because the practical range of

photoelectrons is shorter than the electrode pitch. Diffusion of the electron cloud (rms) is 210$\mu$m for 1cm drift. Hence, the diffusion is expected to be about 60$\mu$m for the drift length of 3mm, which is much shorter than the electrode pitch (400$\mu$m). Fig. 8.1 shows an X-ray transparency image of the test chart. As shown in the figure, even 0.5mm wide slits are clearly separated by eyes.

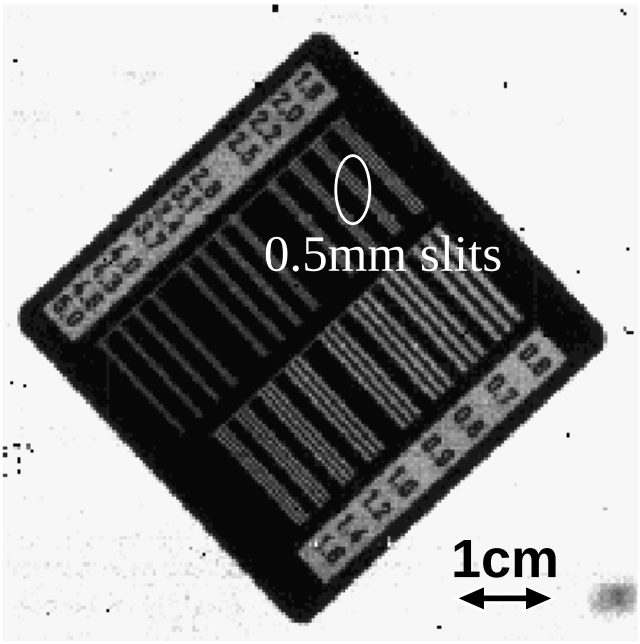


Figure 8.1: X-ray image of a test chart.

From a simple statistics, the spatial resolution (r.m.s.) of the detectors with digital readout is expressed by the following formula:

$$\sigma = d/\sqrt{12}, \tag{8.1}$$

where $d$ is the electrode pitch. Since the electrode pitch of the $\mu$-PIC is 400$\mu$m, the expected spatial resolution is 115$\mu$m. The actual spatial resolution was measured by the knife edge method using the test chart. In order to suppress the range of the electron in the gas, the acceleration voltage of the X-ray generator was set to be 10kV. A 1mm thick aluminum plate was also used for this measurement. The counting rate was projected along one of the edge of the test chart for 2cm as shown in Fig. 8.2. This profile was fitted

using an error function:

$$\mathrm{erf}(x) = \frac{2}{\sqrt{\pi}} \cdot \int_0^x \exp(-t^2)\,\mathrm{d}\,t. \tag{8.2}$$

Then the fitting function is

$$Count(x) = a_1 + a_2 \cdot \mathrm{erf}\left(\frac{x - a_3}{\sqrt{2}a_4}\right), \tag{8.3}$$

where $x$ means the length along the edge and $a_1$, $a_2$, $a_3$, and $a_4$ are the fitting parameters. The calculated spatial resolution, $a_4$, was 120$\mu$m. This result was very close to the limit from the statistics: $\sigma = d/\sqrt{12} = 115\mu$m.

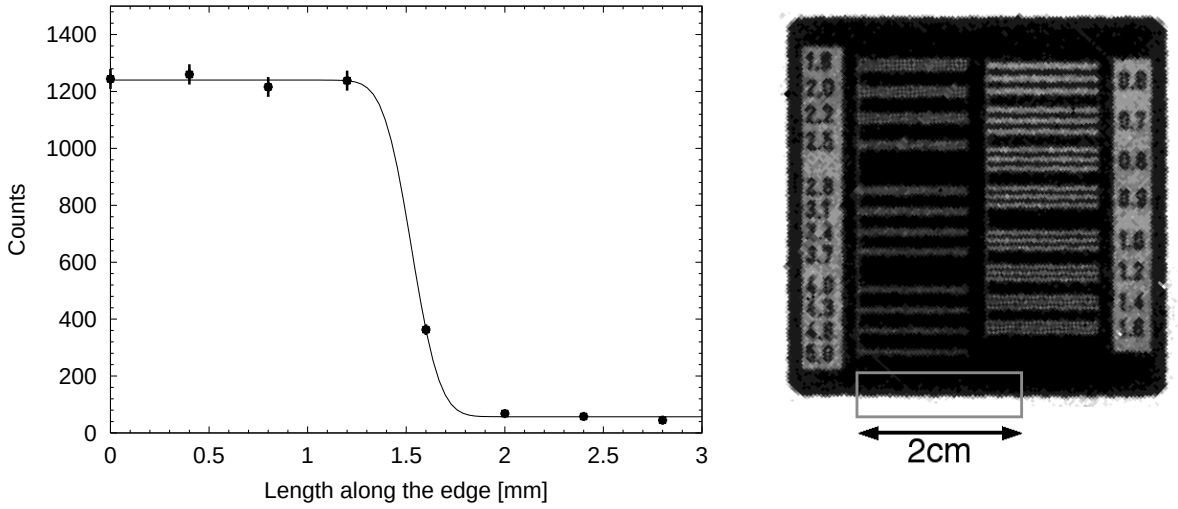


Figure 8.2: Projected image of the test chart edge and the best fit function. The area used for the projection is shown in the right figure.

The image distortion is an important property for large area detectors. In the case of an X-ray image intensifier [51] which is commonly used for material science, there is some image distortion due to the focusing of photoelectrons. Image distortion is also observed for the detector with analog readout such as charge division and delay line methods. Therefore, raw images obtained by these detectors must be calibrated and corrected suitably. To the contrary, the $\mu$-PIC with the fast digital readout causes no image distortion in principle. In order to verify this, a universal printed circuit board

with 0.1 inch pitch and 1mm $\phi$ holes was used as a calibration pattern. The detection area of $76.8 \times 76.8\text{mm}^2$ is used for this experiment, which area corresponds to about 56% of the whole detection area. Fig. 8.3 (a) shows the transparency image of a universal printed circuit board irradiated by the X-ray from the generator with the acceleration voltage of 12kV. The grid in the image are the border lines between pre-amplifiers which are drawn in every 32 channels. The close-up image is shown in Fig. 8.3 (b). The observed image distortion is within the pixel size ($400\mu$m).

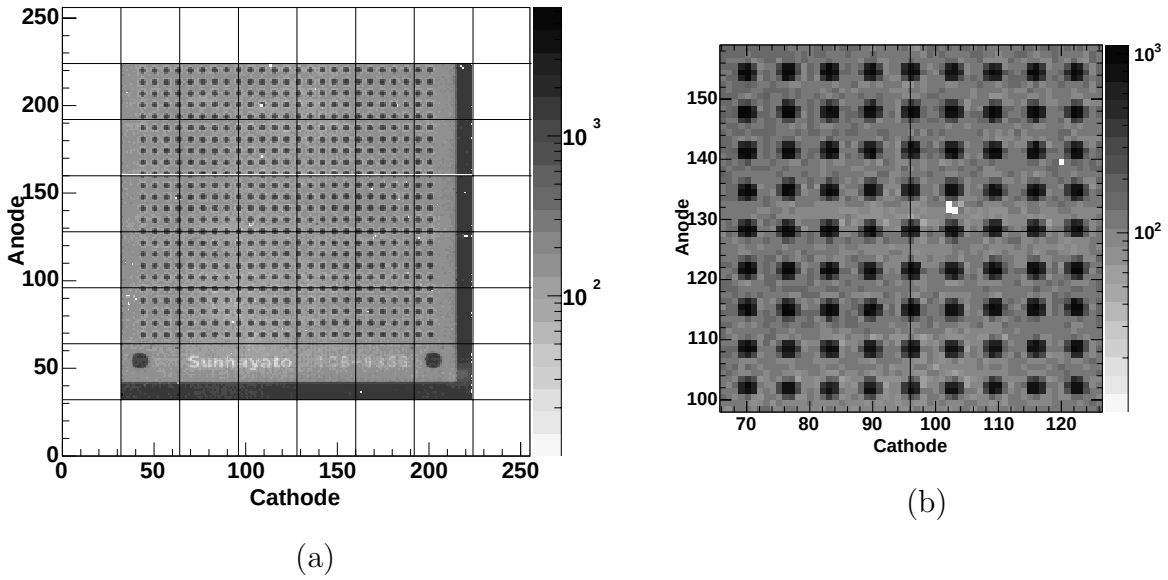


(a) (b)

Figure 8.3: Transparency image of a universal printed board with 0.1 inch pitch (a) and its close-up image (b). The grids in the image mean the border lines between pre-amplifiers which are drawn in every 32 channels. Obviously, the image distortion is within the pixel size.

We also evaluated the image uniformity of the $\mu$-PIC using the detection area of $76.8 \times 64.0\text{mm}^2$. The acceleration voltage of the X-ray generator was 20kV, and the low energy X-ray ($\lesssim$3keV) was filtered by a 200$\mu$m thick aluminum plate. A 5cm thick polyethylene block was used as a scatterer for a uniform irradiation. The obtained image

is shown in Fig. 8.4. The counting rate was slightly high in the center region. That is due to the intrinsic intensity distribution of the X-ray generator. Taking into account the variation of intensity , the non-uniformity of image was about 6% for all detection area.

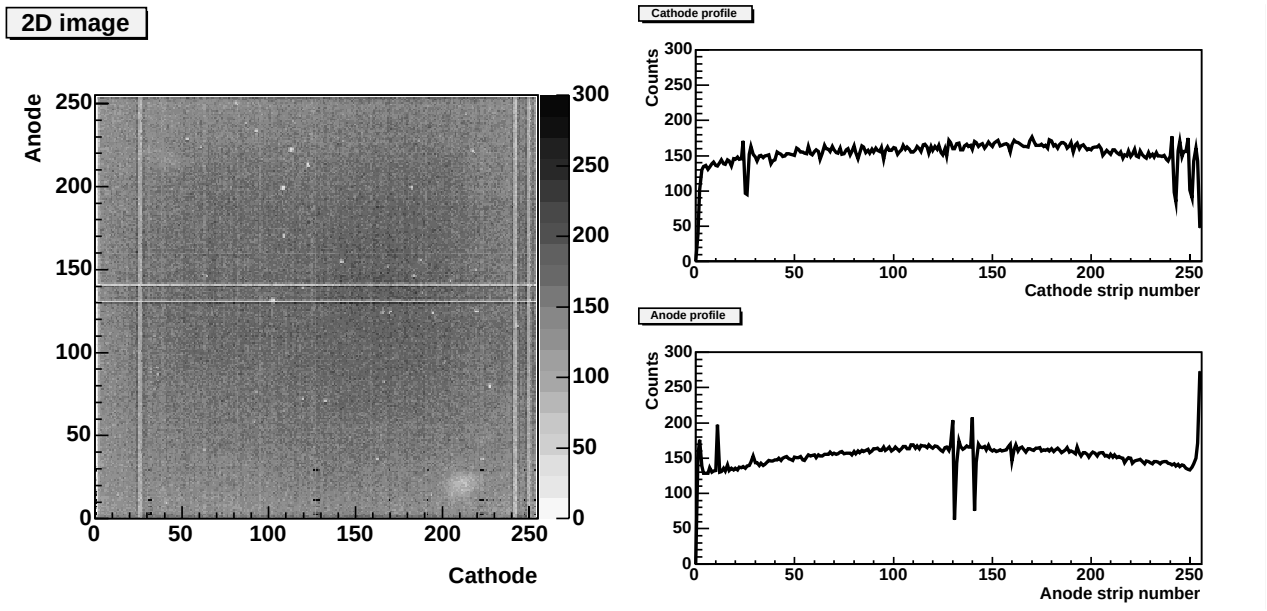


Figure 8.4: The left panel is a two-dimensional image of uniformly irradiated X-ray. In the right panel, the projection on the cathode axis (upper) and on the anode axis (lower).

## 8.2 Performance of $\mu$-TPC

### 8.2.1 $\mu$-PIC readout for the $\mu$-TPC

In order to observe tracks of charged particles, the $\mu$-PIC works as a readout device of a Time Projection Chamber (TPC). The TPC is a three-dimensional tracking device for charged particles, which uses a two-dimensional array of pickup electrodes together with a measurement of the drift time. The TPC consists of multiplication region and drift region as shown in Fig. 8.5. A uniform electric field is applied in the drift region. Conventionally, the multiplication region consists of a MWPC with the segment cathode. An electron cloud along the track of incident charged particles drifts toward the multiplication region

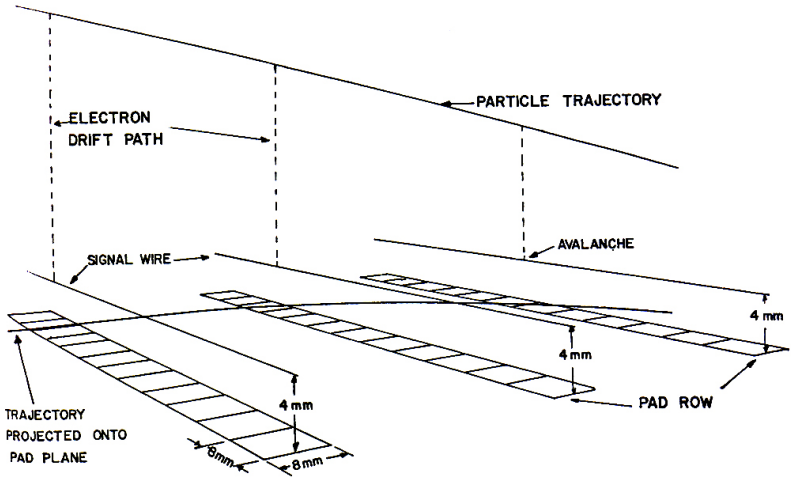


Figure 8.5: Schematic structure of a TPC and the detection principle [57].

and picked up by the anode and the cathode. A three-dimensional track is reconstructed using two-dimensional projected track detected by pick-up electrodes and the hit timing of each electrode. In a conventional TPC consisting of a MWPC and a long drift cage, an avalanche occurs around the sense wire, and signals are induced on the cathode pads. However, a part of ions produced in the avalanche gradually accumulate on the wall of the drift cage, and these accumulated ions distort the electric field in the drift volume. In the case of the conventional MWPC-based TPCs, this problem was overcome by using the gating grids [58]. While gas avalanche is grown around the anode electrodes, the gating grids are closed in order to block the feedback of positive ions to the drift region. In contrast, as described in chapter 3, the feedback of the positive ions to the drift region is suppressed by using a MPGD without gating grids. GEM readout for the TPC is developed in CERN [59].

We made the TPC with the $\mu$-PIC readout which is named the Micro Time Projection Chamber ($\mu$-TPC). The $\mu$-TPC consists of the $\mu$-PIC and the drift cage shown in Fig. 8.6. This drift cage has an area of $10 \times 10\text{cm}^2$ and an 8cm long drift region. A negative high voltage of $-3.3$kV is applied to the top of the drift cage made of a 1mm thick aluminum plate. The 0.3mm thick inner aluminum plane is connected to it through 22M$\Omega$. A 4mm wide field cage electrode is connected to the plane through 10M$\Omega$. Another fourteen field

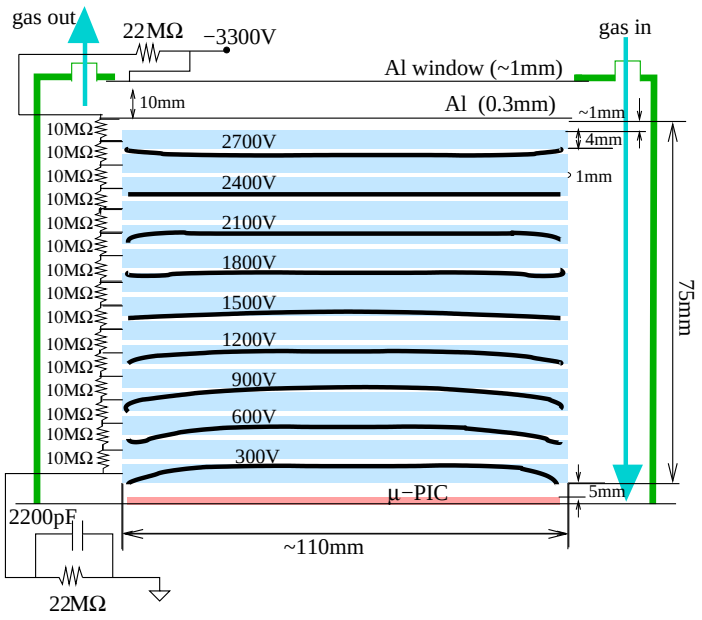


Figure 8.6: Structure of the $\mu$-TPC with the calculated electric potential (thick solid lines).

cage electrodes are spaced by 1mm, and each is connected to the next through 10MΩ. The wide field cage electrode prevent from attachment of positive ions on the insulating gap between the electrodes. The photograph of the field cage is shown in Fig. 8.7. Gas flows through the chamber via connectors at both sides of the top plate. Fig. 8.6 also shows the calculated electric potential in the drift region by the GARFIELD program [54]. An electric field of 0.4kV/cm was produced uniformly in the inner region (∼80% of the full drift volume). The field cage was set in a gas vessel and mounted on the mother board as shown in Fig. 8.8.

### 8.2.2 Heavy particles

Tracking of heavy charged particles with sub-relativistic energy is not so difficult, because the energy loss of the particle is large. Therefore, a dense track is expected to be observed with a moderate gas gain ($\sim$ 3000). We used the gas mixture of argon and ethane with the mixture ratio of 80:20 and 90:10. The basic properties of each mixture are summarized

Figure 8.7: Photograph of the field cage of the $\mu$-TPC.

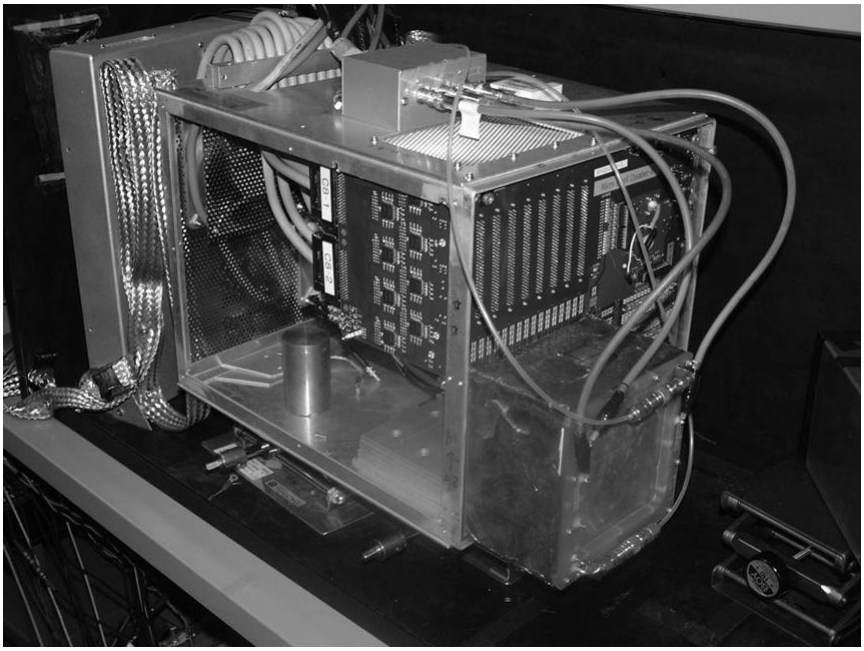

Figure 8.8: The photograph of the developed $\mu$-TPC.

in Table 8.1.

| Mixture ratio | Drift velocity [cm/$\mu$s] | Diffusion ($\sigma$[$\mu$m]) |
|---|---|---|
| 80:20 | 4.7 | 350 |
| 90:10 | 3.6 | 440 |

Table 8.1: Properties of the gas mixtures of Ar-$C_2H_6$ in the drift field of 0.4kV/cm. Diffusion means the standard deviation for 1cm drift.

The performance of the $\mu$-TPC was tested using high energy protons of 0.3-2.0GeV/c with Ar/$C_2H_6$ (80/20) gas mixture. A photograph of the experimental setup is shown in Fig. 8.9. The energy of incident particles from the right of this figure is varied by the magnet. The Cherenkov counter and the time of flight (TOF) counters were not used in this experiments. Two plastic scintillators were used as trigger counters. The incident particles were identified using pulse height information from the trigger counters. The $\mu$-PIC used in this experiment was the previous type.

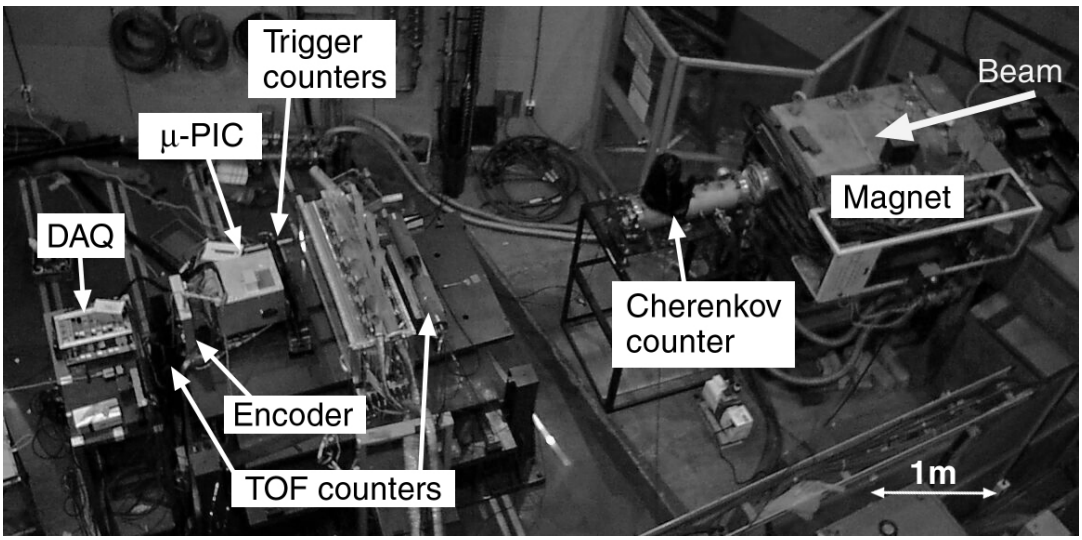


Figure 8.9: Setup photograph of the beam test.

In this experiment, three-dimensional spatial resolution was measured using tracks of heavy charged particles such as protons. These particles are hardly deflected by multiple

scatterings. Therefore the tracks of the heavy charged particles are regarded as straight lines. Fig. 8.10 shows a typical three-dimensional image of a proton of 0.8GeV/c. The average sampling interval was about 1.5mm for the projection on the anode-cathode plane and 2.6mm for three-dimensional tracks. Each obtained track was fitted with a three-dimensional linear function. The position resolution is defined as the root mean square of the residual distribution. The residual distribution of the proton tracks is shown in Fig. 8.11 by a solid line. The obtained three-dimensional position resolution was 320$\mu$m for $Ar/C_2H_6$ (80/20) gas mixture. This resolution is limited by the DAQ system clock of 20MHz. Drift velocity of electrons in the gas is 4.7cm/$\mu$sec, then the primary electrons drift about 2mm during 1 clock time (50nsec). Although, two-dimensional spatial resolution of 250$\mu$m was obtained, the three-dimensional resolution was somewhat degraded by the resolution of the drift direction.

A similar experiment was performed for argon and ethane gas mixture with the mixture ratio of 90:10. The position resolution was measured using recoil protons (0.5-1.0MeV) due to fast neutrons from a radioactive source of $^{252}$Cf. The residual distribution is also shown in Fig. 8.11 by a doted line. The obtained position resolution was 260$\mu$m. The difference between these two results is proportional to the difference of the drift velocity of the gas mixtures. The three-dimensional position resolution is restricted by the DAQ clock of 20MHz. We are now improving a rate of clocks in the DAQ system to 50MHz, by which a position resolution of about 210$\mu$m for an $Ar/C_2H_6$ (90/10) gas mixture is expected.

### 8.2.3 Minimum ionizing particles

Electron tracks were detected using Compton scattering of 662keV gamma-ray from a $^{137}$Cs source. The energy of the recoil electrons are estimated to be several hundred keV. In this experiment, the $\mu$-PIC worked as a $\mu$-TPC for gamma-ray imaging (Ref [60, 61] and Sec. 9.3.1). The $\mu$-TPC was triggered by scatter gamma-rays detected by a NaI scintillator behind the $\mu$-TPC. One of the typical three-dimensional tracks of recoil electron is shown in Fig. 8.12. A winding track was clearly detected like a “electric cloud chamber”. In this figure, the direction of the electron was upward. The gas gain of the $\mu$-PIC in this test was about 3000.

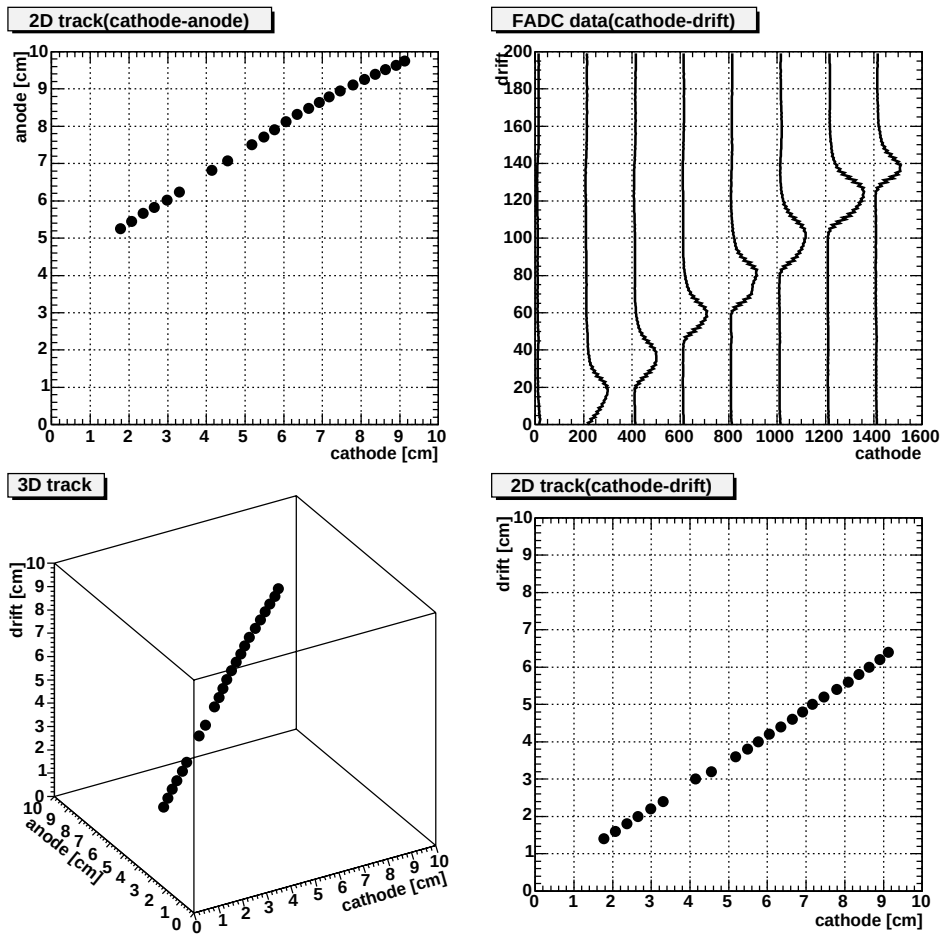


Figure 8.10: A three-dimensional track image of a proton (0.8GeV). The upper-left and lower-right images are two-dimensional projection onto the cathode-anode plane and the cathode-drift plane. The upper right graph is pulse heights obtained each cathode pre-amplifier.

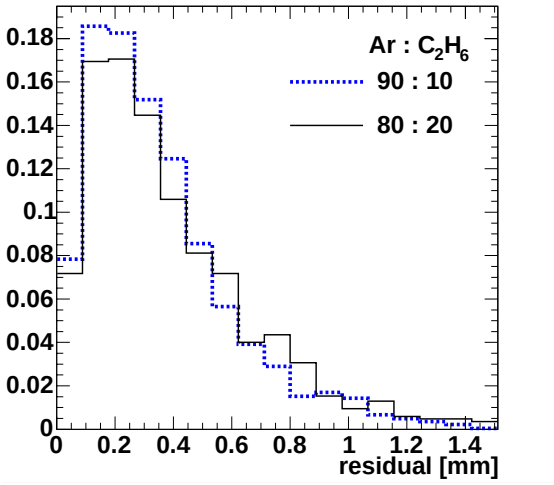


Figure 8.11: Residual distributions of the proton tracks.

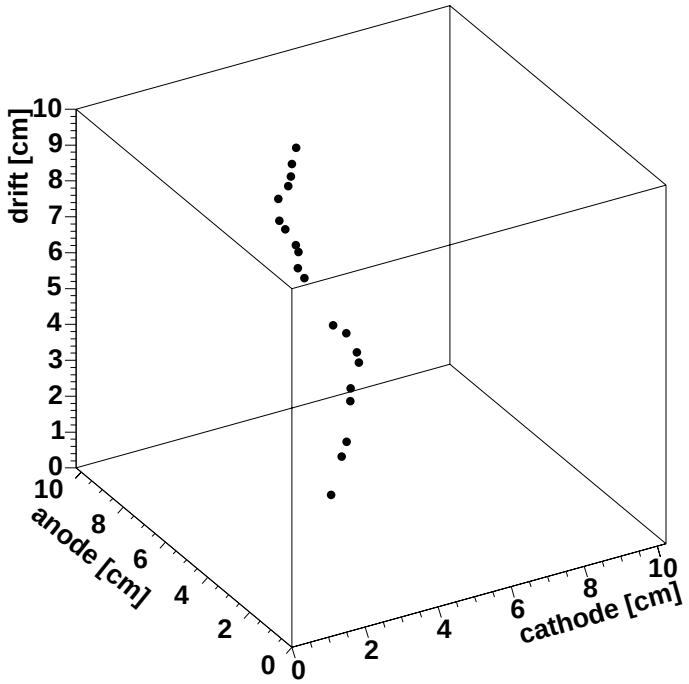


Figure 8.12: A three-dimensional image of an electron track originated in a Compton scattering of a 662keV gamma-ray from a $^{137}$Cs source.

Tracks of cosmic-ray muons were also detected as shown in Fig. 8.13. The $\mu$-TPC was triggered by the coincidence of two plastic scintillators placed on both sides of the $\mu$-TPC. In this experiment, intervals of obtained plot was rather coarse. The tracking efficiency ($>$ 3 points) was about 20% for the gas gain of 3000-5000. This result means that the sufficient gas gain has not been obtained for the previous $\mu$-PIC. Actually, the energy deposition of MIPs is about 2MeV/(g/cm$^2$). About 4 electron-ion pairs are produced in the length of one electrode (400$\mu$m) by an MIP in an Ar/$C_2H_6$ (80/20) gas mixture of the atmospheric pressure. The required gas gain to detect dense tracks of MIP is $\sim 10^4$, which has been obtained in the new $\mu$-PIC.

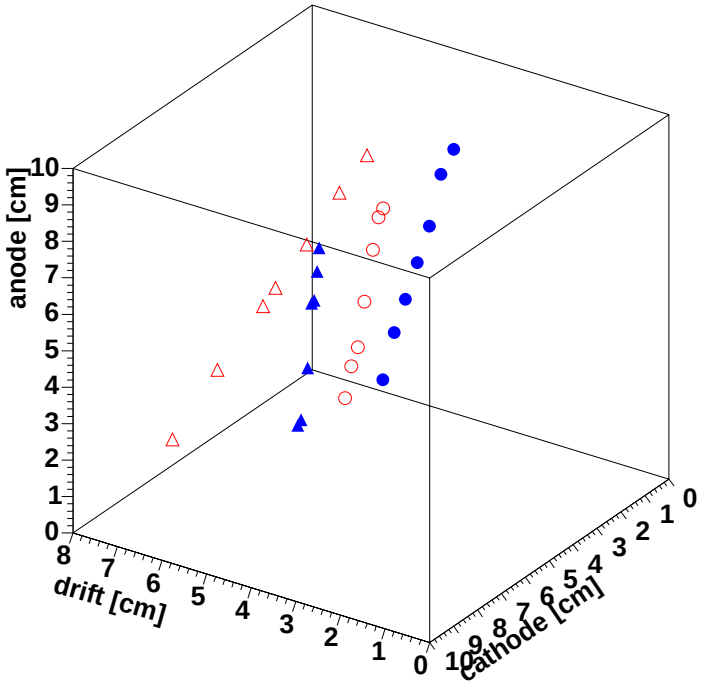


Figure 8.13: Three-dimensional track of cosmic-ray muons.

# Chapter 9

# Application of $\mu$-PIC

Because of the imaging performance and fine timing resolution, the $\mu$-PIC is a promising detector for many fields of science, i.e. X-ray and gamma-ray astrophysics, X-ray crystallography, high energy particle physic etc. The development of the $\mu$-PIC for several applications being done by our group are briefly described in this chapter.

## 9.1 X-ray polarimetry

### Principle

The narrow spacing of the electrodes of the $\mu$-PIC allows us to detect the polarization of the incident X-ray. Incident X-rays kick out an orbital electrons of an atom via the photoelectric effect. The range of the emitted electrons (photoelectrons) in argon gas is $\sim$1mm for 8keV X-ray and $\sim$5mm for 20keV X-ray, which are sufficiently longer than the electrode pitch of the $\mu$-PIC. Thus, the photoelectrons are expected to run over several electrodes. The differential cross section of the scattering angle of a photoelectron is given by

$$\frac{d\sigma}{d\Omega} \propto \frac{\sin^2\theta\cos^2\phi}{(1-\beta\cos\theta)^4}, \tag{9.1}$$

where $\theta$ and $\phi$ are polar and azimuth angle of the photoelectron, respectively. $\beta = v/c$ means the velocity of the photoelectron, which corresponds to the energy of incident X-ray. If the incident X-ray is fully polarized, the angular distribution of the emission become

maximum at the direction of the electric field of the incident X-ray as shown in Fig. 9.1. While the range of photoelectrons is long, large asymmetry of the vertical and horizontal width is obtained. Therefore, light gases such as argon and neon are rather suitable than heavy gases such as xenon, because a long range of photoelectrons is obtained for the light gases as mentioned in Sec. 2.3.

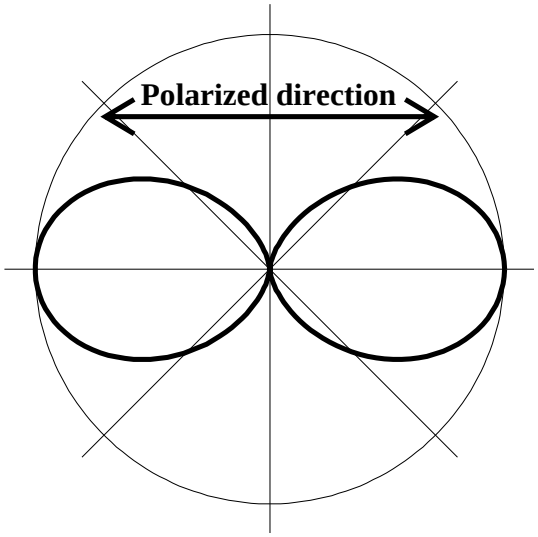


Figure 9.1: The angular distribution of the photoelectrons for fully polarized X-ray.

The direction of X-ray polarization is measured by counting the hit electrodes horizontally and vertically as shown in Fig. 9.2.

**Experiment**

The photograph of the experimental setup is shown in Fig. 9.3. The polarized X-ray was produced using perpendicular Thomson scattering on a polyethylene block. The scattered X-ray is fully polarized theoretically. As the X-ray source, we used an X-ray generator same as that described in chapter 6 again. The $\mu$-PIC was filled with the $Ar/C_2H_6$ (80/20) or $Ne/C_2H_6$ (80/20) gas mixture of atmospheric pressure, and the drift field of 500V/cm was applied in a 12mm thick gas volume.

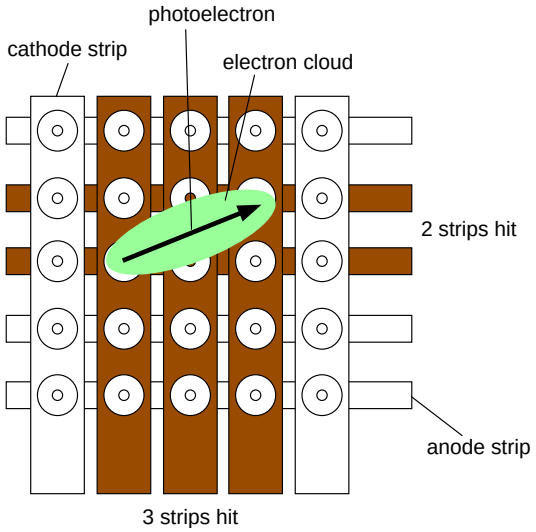


Figure 9.2: Measurement of the "hit width" of electrodes.

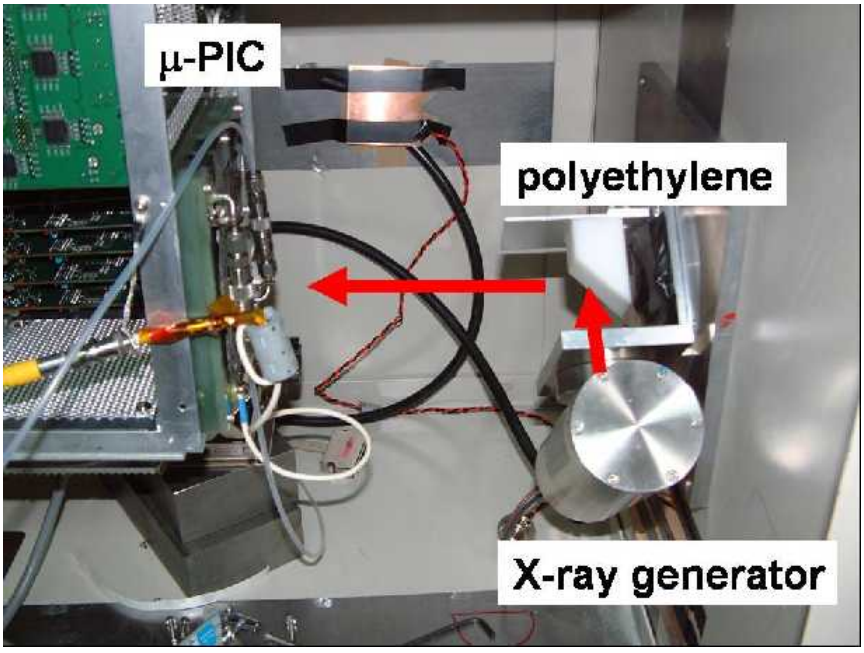


Figure 9.3: Experimental setup of X-ray polarization detection.

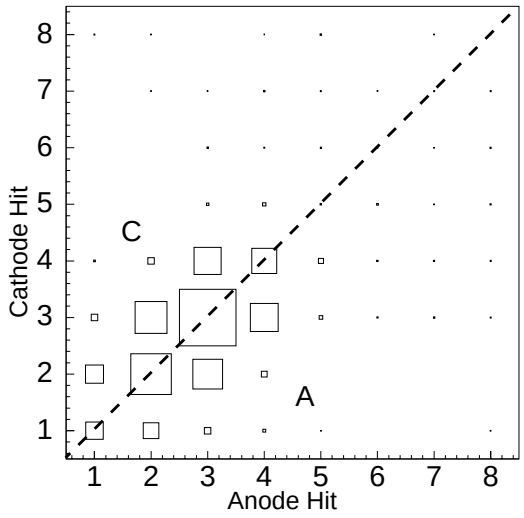


Figure 9.4: A typical distribution pattern of the hit number of anode and cathode electrodes for the X-ray energy of ∼8keV. The size of each square indicates the number of events.

**Result**

Fig. 9.4 shows an example of the distribution of the hit number of anode and cathode electrode for the X-ray energy of ∼8keV. In this figure, the size of each square indicates the number of events. We define $A$ as the number of events whose hit number of anode strips are larger than that of cathode strips, and $C$ as vice versa. If $A$ is larger than $C$, we regarded the direction of polarization as the direction of the anode strips. Here, we define a degree of bias, or "difference factor" $D$ as

$$D = \frac{A - C}{A + C}. \tag{9.2}$$

The difference factor varies with the rotation angle of the polyethylene scatterer. Although the maximum difference factor of 1.0 is expected from fully polarized X-ray, obtained difference factor is less than 1.0 because the tracks of photoelectrons are intricately straggled. The range of photoelectrons become longer with the energy of incident X-ray. Therefore, high difference factor was obtained from high energy X-ray as shown in Fig. 9.6. The consistent result was obtained from a Monte Carlo simulation [62] using the EGS4

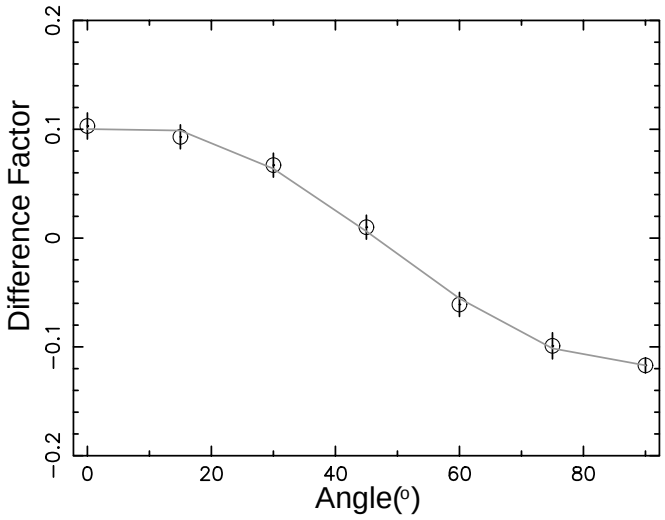


Figure 9.5: Variation of the difference factor as a function of the rotation angle of polyethylene scatterer.

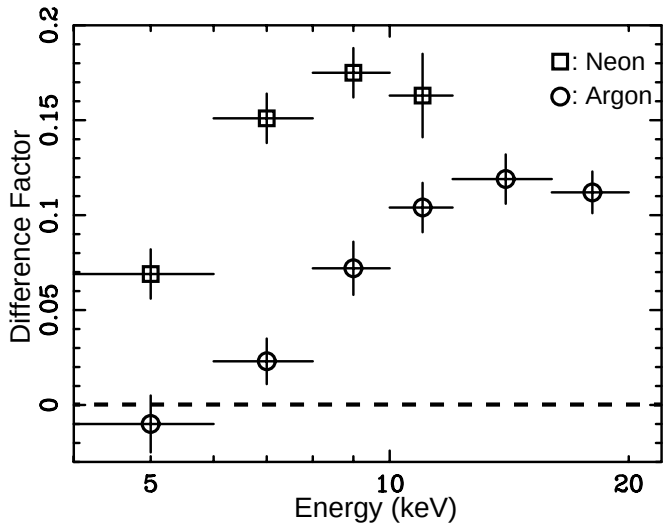


Figure 9.6: Dependence of the modulation factor as a function of the X-ray energy.

code [63].

**Future prospect**

In the case of a strip-readout detector such as $\mu$-PIC, the degree of polarization is derived as the variation of the difference factor. Therefore, the observation have to be done at least two rotating angle. In contrast, the image of a photoelectrons would obtain by a pixel-readout detector. In this case, the degree of polarization can be obtained without a rotation of the detector. We are developing a new $\mu$-PIC with pixel-readout. The schematic drawing is shown in Figs. 9.7. The thin electrode is formed on a ceramic substrate with the pitch of 600$\mu$m. The surface of the ceramic substrate is covered by thin polyimide layer in order to avoid the attachment of materials on the ceramic substrate.

This $\mu$-PIC with pixel-readout is developed as a focal plane detector of a X-ray telescope. Until now, the only source from which X-ray polarization was detected was the Crab Nebula [64], although the polarization has important information in astrophysics i.e. magnetic field around Supernova remnants.

## 9.2 X-ray crystallography

X-ray diffraction study is one of the most expected fields for $\mu$-PICs. In this field, a integrating area detector such as an Imaging Plate (IP) [65] or CCD had been commonly used. However, timing and energy information are not obtained by the integrating detector. Today, the main device for the X-ray crystallography is a 4-axis diffractometer using a zero-dimensional pulse counting detector such as a scintillator. In this case, the detector observe all diffraction spots. Therefore, it takes very long time (more than 1 day). On the other hand, an MPGD is a pulse counting area detector, hence rapid crystal analysis is available. In particular, for an MSGC, the wide dynamic range of $10^6$ was obtained [66]. Therefore, the MPGDs are suitable device for X-ray crystallography.

A new analyzing method, "Continuous Rotation Photograph (CRP) method" had been developed for a MSGC [3], in which all diffraction peaks can be obtained within one continuous rotation of a crystal. Using the CRP method, the measurement time of 2.1sec was achieved for an ammonium bitartrate (ABT) crystal by using a commercially-available

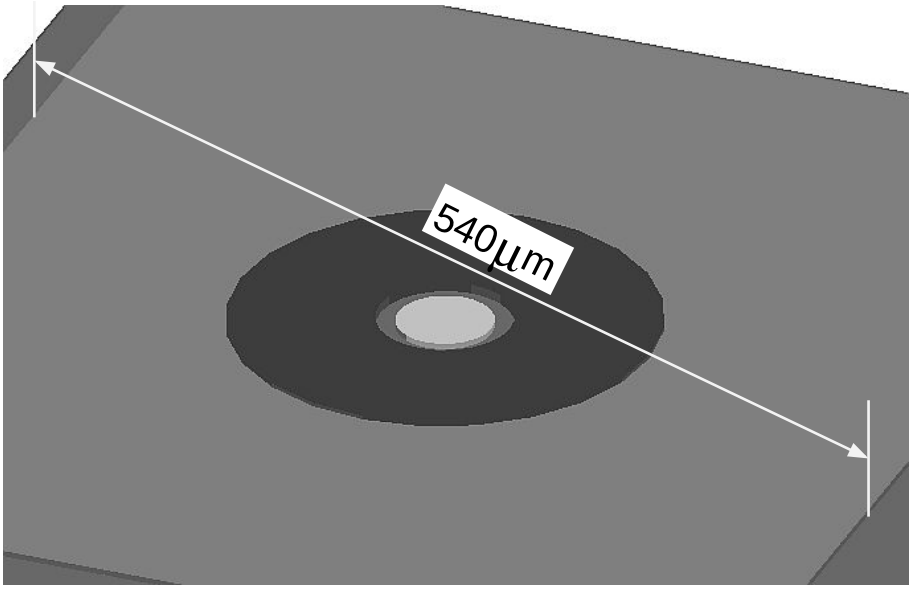


(a)

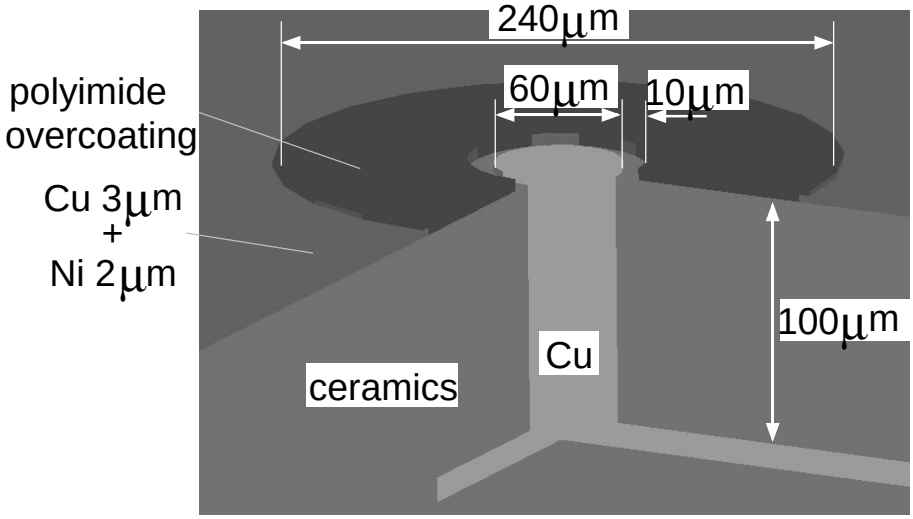


(b)

Figure 9.7: Schematic drawing of the pixel readout $\mu$-PIC. (a) is a top view of the detector, and (b) shows a cross-sectional view of the detector.

X-ray generator in the laboratory [67]. Rotational photograph image and the directly reconstructed reciprocal lattice of an ABT crystal using the CRP method is shown in Figs. 9.8 and 9.9, respectively [3]. Both results were taken using a two-dimensional MSGC. Because long term sequential operation is possible for the $\mu$-PIC, and then statistically

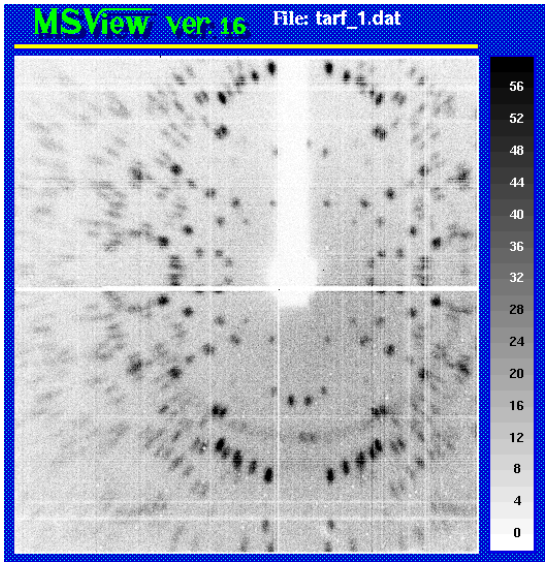


Figure 9.8: Rotational photograph image of an ABT crystal [3].

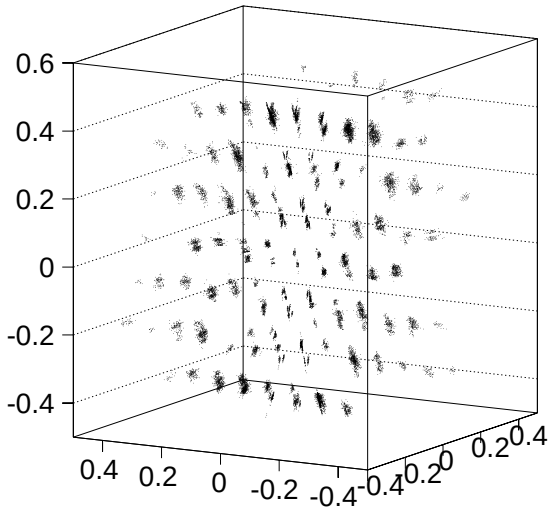


Figure 9.9: Directly reconstructed reciprocal lattice using the CRP method. The unit of length is 1/Å [3].

good data is expected, the quality will be comparable to the IP or the CCD.

A preliminary experiment of the X-ray crystallography was performed at Ohashi-Uekusa Laboratory of Tokyo Institute of Technology. The experimental setup is shown in Fig. 9.10. The sample was a crystal of ylide, which was set at 10cm from the detector surface. This sample was irradiated by a collimated X-ray from an X-ray generator with a molybdenum target. The acceleration voltage and tube current were set to be 50kV and 250mA, respectively. The continuous component was reduced by a monochromator, and the sample was irradiated by the Mo K-$\alpha$ line (17.5keV). The $\mu$-PIC was filled with the argon-based gas of atmospheric pressure, and the drift field of 600V/cm in a 1mm thick gas volume. The gas gain of the $\mu$-PIC was set to be 3200 in order to avoid discharges.

Fig. 9.11 shows a rotational image of a ylide crystal observed by the $\mu$-PIC with the

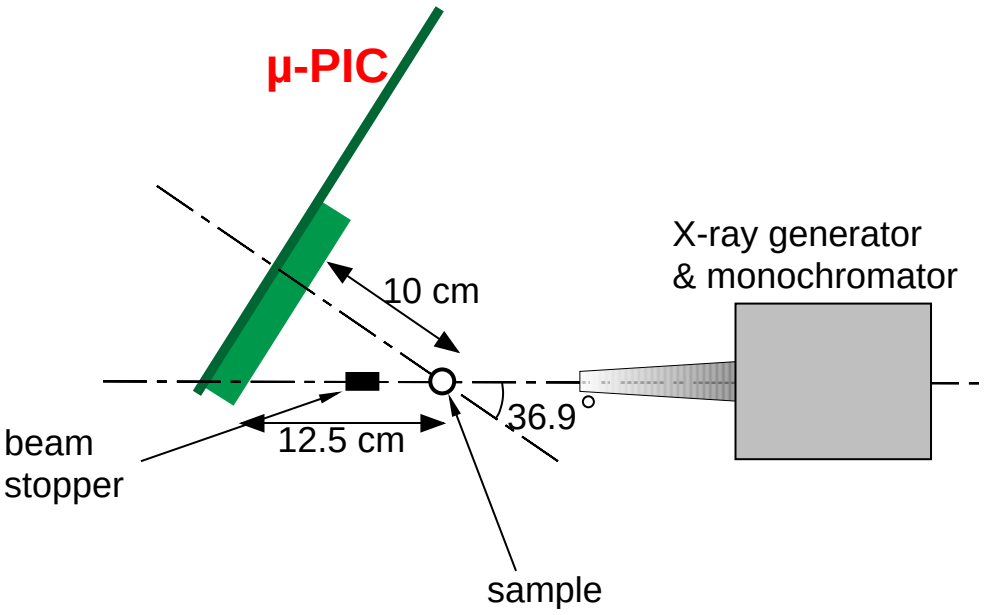


Figure 9.10: Setup of the X-ray diffraction experiment.

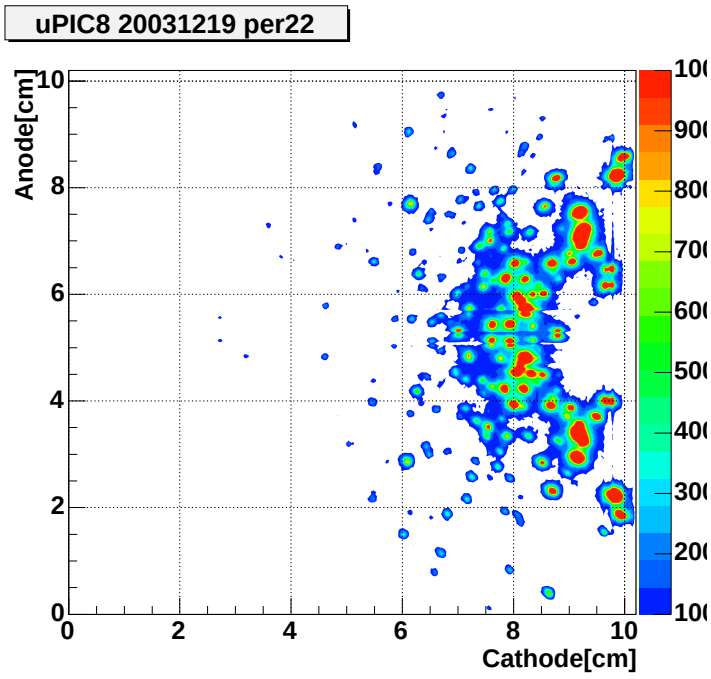


Figure 9.11: Rotational image of a ylide crystal observed by the $\mu$-PIC.

irradiation time of 30min, where the rate of the crystal rotation was 0.1/min. Because of the long irradiation time, statistically good data was obtained. Although we used the argon-based gas in this experiment due to its easy-handling, in order to obtain more precise diffraction spots, we would perform this experiment using the xenon-based gas in near future.

## 9.3 Application of $\mu$-TPC

### 9.3.1 Gamma-ray imaging

#### Principle

In astrophysics, gamma-ray observation have become a very promising field. However, the detection of gamma-rays in MeV region is still uncultivated, although this region would surely show us new aspects of high energy phenomena in the universe. This is almost due to the nonexistence of the practical detector for this energy region after COMPTEL [68] aboard Compton Gamma-Ray Observatory (CGRO).

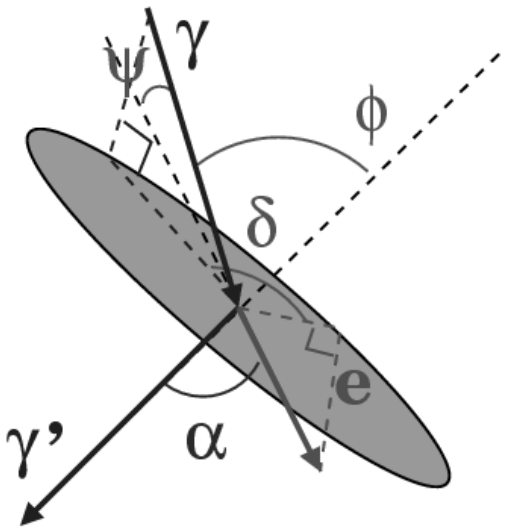


Figure 9.12: Description of axes used for the event reconstruction.

In this energy region, the incident gamma-ray is detected via a Compton scattering.

Fig. 9.12 shows the description of axes used for the gamma-ray imaging. The angle $\phi$ is defined as the angle between the scattered gamma-ray and the incident gamma-ray, which is derived from the kinematics of the Compton scattering as follows:

$$\cos\phi = m_e c^2 \left( \frac{1}{E_{\gamma'}} - \frac{1}{E_0} \right), \quad E_0 = E_{\gamma'} + K_e, \tag{9.3}$$

where $E_0$ is the energy of the incident gamma-ray, and $E_{\gamma'}$ and $K_e$ are the energies of the scattered gamma-ray and the recoil electron, respectively. The conventional detectors such as COMPTEL consist of two position sensitive gamma-ray detectors: the scatterer and the absorber. If the scattered gamma-ray deposit the whole energy in the absorber, as shown in Figs. 9.13, an "event circle" of the incident gamma-ray is determined using the positions of the absorption point and the scattering point, and the energies of the scattered gamma-ray and the recoil electron. The incident direction is obtained as an intersection of at least three event circles.

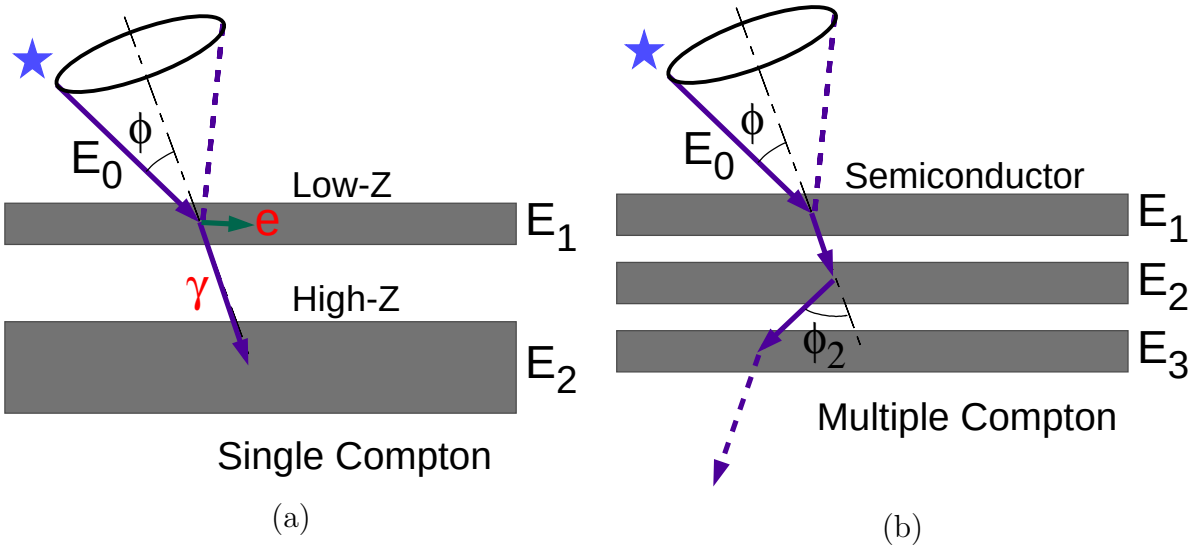


Figure 9.13: Principles of gamma-ray detector using the Compton scattering.

In the classical Compton type detectors, it is difficult to reconstruct diffused gamma-ray sources, because all event circles do not cross at one point.

Recently several detectors are developed [69]. These detectors, which are called multiple Compton detector (Fig. 9.13 (b)), consist of a number of scintillator or semiconductor

detectors. Each detector works as both scatterer and absorber. In these detectors, however, at least three event circles to obtain the incident direction of gamma-ray. Therefore, they have the same problem as the single Compton detectors. In order to completely reconstruct the incident gamma-ray by one event, the track of recoil electrons have to be detected. This is quite difficult for Compton detectors using solid state detectors.

**Advanced Compton method**

In order to obtain the incident direction by one Compton event, one additional information is required. If the recoil angle of the electron is measured, we can define the angle $\delta$ which is the angle between projected vectors of the recoil electron and the incident gamma-ray on the normal plane to the scattered gamma-ray (See Fig. 9.12). The original direction of the incident gamma-ray can be reconstructed as a small segment of a Compton event circle. In order to measure the recoil angle of an electron, the recoil electron have to be tracked accurately. For this purpose, the gas is suitable material as the scatterer.

In order to obtain a fine three-dimensional track of a recoil electron, we have developed the $\mu$-TPC, which consists of the detection volume of $10 \times 10 \times 8\text{cm}^3$ and the $10 \times 10\text{cm}^2$ $\mu$-PIC readout. This $\mu$-TPC works as both the scatterer for incident gamma-rays and the tracker for recoil electrons. The observed track of the recoil electron provide the recoil angle, and the energy deposit provide the kinetic energy $K_\text{e}$ of the recoil electron. As the absorber, an Anger camera consisting of a $10 \times 10 \times 2.5\text{cm}^3$ NaI(Tl) scintillator is used. Scattered gamma-rays are detected by the scintillator and the energy and the absorption point are measured with $5 \times 5$ 3/4-inch PMTs. This Anger camera is set in front of the $\mu$-TPC (Fig. 9.14). The timing information which is obtained from the scintillator is also used as a trigger signal for the $\mu$-TPC. A three-dimensional track of an electron is reconstructed using the position and the relative timing information of an electron and the trigger timing obtained by the scintillator. This is the first detector which can reconstruct the incident gamma-ray by one event.

Furthermore, the opening angle $\alpha$ between the recoil electron and the scattered gamma-ray can be used for background rejection. The $\alpha$ angle is derived by two method: geometrical and kinematical method. First, $\alpha$ is geometrically measured using the detected electron track and the absorption point of the scattered gamma-ray. On the other hand,

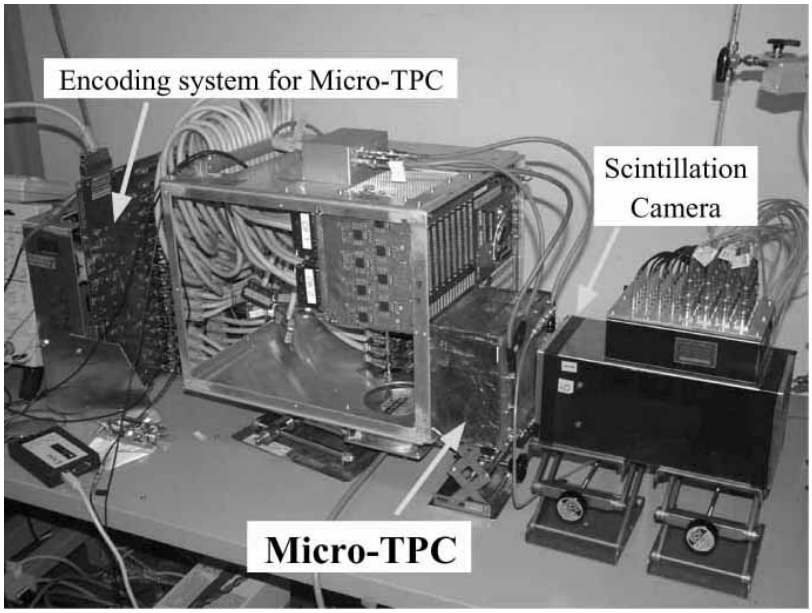


Figure 9.14: Gamma-ray imaging detector.

$\alpha$ is derived by the kinematics of Compton scattering as follows:

$$\cos\alpha = \frac{K_{\rm e}(E_{\gamma'} - m_{\rm e}c^2)}{E_{\gamma'}\sqrt{K_{\rm e}^2 + 2K_{\rm e}\, m_{\rm e}c^2}}. \tag{9.4}$$

If the scattered gamma-ray does not deposit all energy in the scintillation detector (Compton escape event), the gamma-ray is not reconstructed correctly. In this case, the $\alpha$ measured geometrically is inconsistent with that derived from the Compton kinematics. This background rejection method is named "kinematical cut". As well as Compton escape events, other background such as charged particles can be rejected using the kinematical cut. Thus no veto detector is needed for this $\mu$-TPC based gamma-ray detector.

**Experimental result**

The imaging characteristic of the detector was examined using the $^{137}$Cs radioactive source which emits 662keV gamma-ray. The source was placed behind the mother board of the $\mu$-PIC. The distance between the source and the $\mu$-PIC was 5cm. The scintillator was set in front of the $\mu$-TPC. Fig. 9.15 shows a typical Compton event. The direction of the

incident gamma-ray was correctly reconstructed from one event.

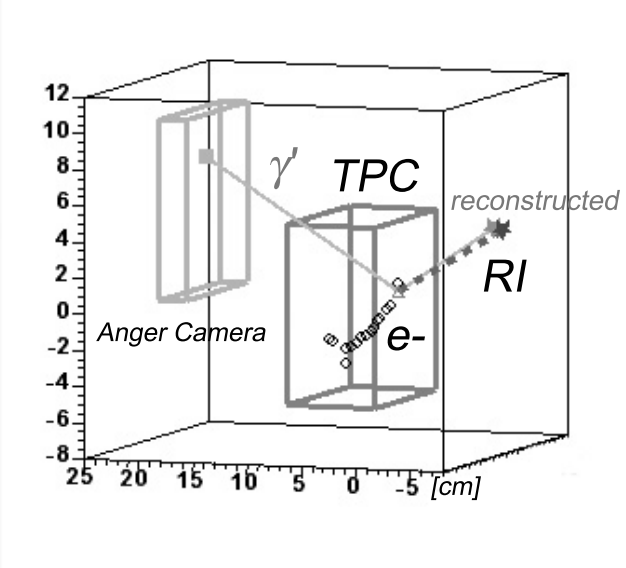


Figure 9.15: Typical reconstructed event.

It is difficult to resolve two gamma-ray sources with a conventional Compton detector in particular when these two sources emit same energy gamma-rays. However, clearly separated image was obtained by the $\mu$-TPC based detector as shown in Fig. 9.16. The angular resolution were 11.5 degrees for $\phi$ direction and 22.3 degrees for $\delta$ direction. The angular resolution is restricted by the spatial resolutions of the $\mu$-TPC and the Anger camera. As mentioned in section 8.2, the spatial resolution of the $\mu$-TPC will increase when a DAQ system with a clock of 50MHz will be completed. In order to improve the spatial resolution of the scintillation camera, we are developing a pixellated CsI(Tl) scintillator instead of an Anger camera, and a Si PIN photodiode array is being developed as a readout device of the scintillation camera [70].

**Future prospect**

As the next step, we are planning to develop the larger (more than $30 \times 30 \times 30\text{cm}^3$) $\mu$-TPC which is surrounded by scintillation camera (Fig. 9.17). In the near future, this detector will be mounted on a balloon. This detector cover the energy region of 0.1-

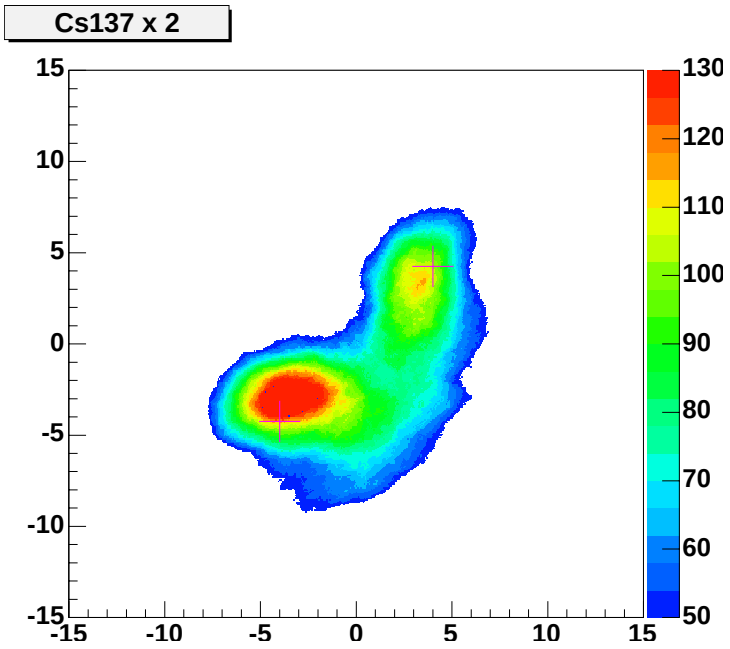


Figure 9.16: Reconstructed image of two $^{137}$Cs sources. The real position of the gamma-ray sources are indicated as two crosses.

30MeV. In the low energy region (0.1-2MeV), the incident gamma-ray is reconstructed using Compton scattering as described above. In the high energy region (1-30MeV), the pair creation process is used for the reconstruction of the incident gamma-ray. According to a simulation work, the position resolution of less than 1 degree is expected at the energy of 20MeV [60].

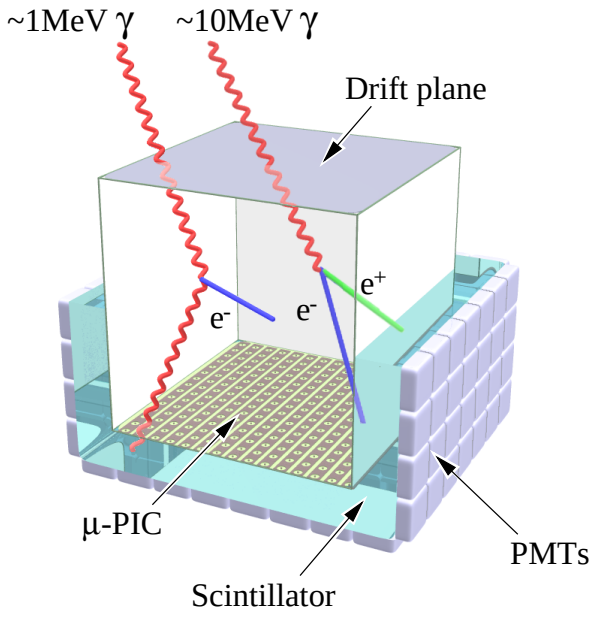


Figure 9.17: Schematic structure of the MeV gamma-ray detector based on μ-TPC.

### 9.3.2 Neutron imaging

#### Principle

Now neutron time-resolved imaging becomes important technique. In the X-ray crystallography, the material containing heavy atoms can be well analyzed. However, X-ray have poor sensitivity for light atoms such as hydrogen, carbon, oxygen, and nitrogen. In contrast, the cross section of a neutron become large for these light atoms. These elements constitute biomolecule such as protein. Thus, neutron diffraction study is becoming a powerful tool for bioscience. Neutron position sensitive detectors (PSDs) with a large

detection area is necessary for this purpose.

Additionally, excellent timing resolution ($\ll$ msec) is required for pulsed neutron source, because energies of thermal neutrons is measured using time-of-flight method. In particular, a capacity for operation in high counting rate are indispensable for use at a neutron beams of the next generation [71]. Gas-filled neutron detectors have an advantage of the large detection area.

For gaseous neutron detectors, $^3$He is commonly used, where a following interaction occurs:

$$\mathrm{n} + {}^3\mathrm{He} \rightarrow \mathrm{p}\,(578\mathrm{keV}) + {}^3\mathrm{H}\,(193\mathrm{keV}).$$

This interaction has a large cross section for thermal neutrons of about 25meV, and the energy loss of the emitted nuclei in gas is quite large. The range of the emitted nuclei are about 10mm for the proton and about 3mm for the triton in argon gas of atmospheric pressure. These range are long enough for tracking by a $\mu$-PIC. Furthermore, the large energy losses provide a dense sampling of the tracks.

### Neutron detection using $\mu$-TPC

As a preliminary experiment, we verified the principle of the neutron detection using our $\mu$-TPC. The $\mu$-TPC was filled with the $Ar/C_2H_6$ (90/10) gas mixture of atmospheric pressure. In this experiment, the $\mu$-TPC was irradiated with fast neutron from a $^{252}$Cf radioactive source, the neutron energy of which peaks between 500keV and 1MeV. The neutrons kick the hydrogen nuclei in $C_2H_6$, and part of the kinetic energy of the neutron is transferred to the recoil nucleus, i.e. the proton. The tracks and the energy loss of the proton in the gas is detected by the $\mu$-TPC. One fission of a $^{252}$Cf emits 3.8 neutrons and 9.7 gamma-rays on average. These gamma-rays were detected by a YAP scintillator (1inch $\times$ 1inch$\phi$) and used for the trigger of the $\mu$-TPC.

The $\mu$-PIC was operated with the gas gain of 3000. This gas gain is high enough to detect dense tracks of protons. Fig. 9.18 shows the detected tracks of protons. The spatial resolution of the track was 260$\mu$m, which is discussed in section 8.2.2. The energy loss of the protons was measured by a FADC (REPIC RPV160). The measured energy losses are shown in Fig. 9.19. The waveforms show that the $\mu$-TPC has sufficient performance to detect tracks and Bragg curves of protons with energies of around 1MeV.

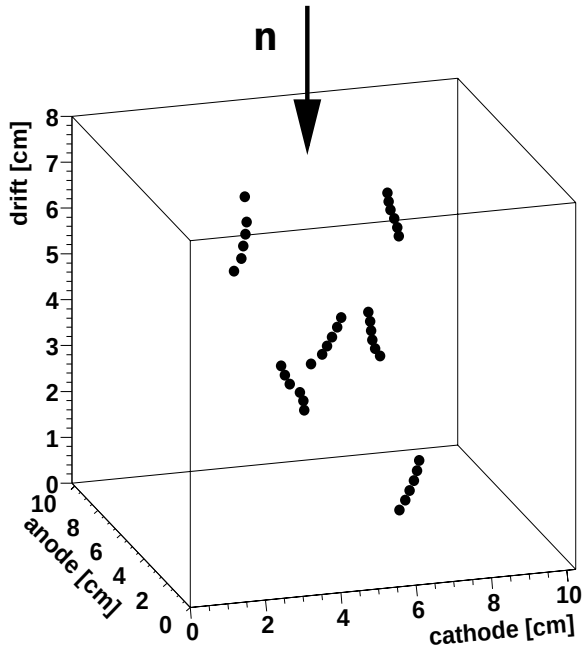


Figure 9.18: Several three-dimensional proton tracks.

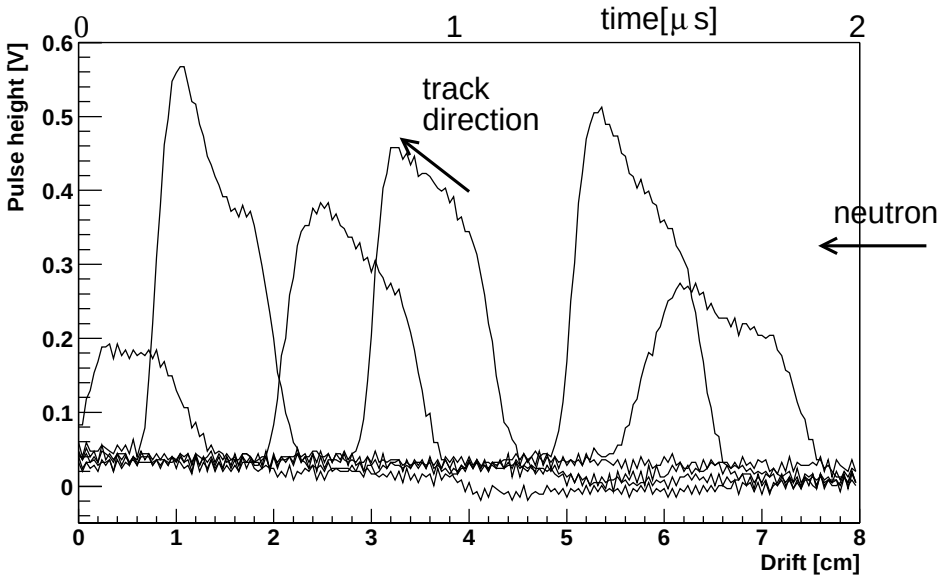


Figure 9.19: Energy loss of the protons. The direction of the tracks are recognized from the shape of the Bragg curve.

### Background rejection

Since the neutron generation process utilize nuclear reactions, large number of gamma-rays are emitted in the process, which become a serious background source. A gamma-ray kicks a electron from an atom via Compton scattering. Therefore, when electron tracks are detected, it can be regarded as gamma-ray events. In order to discriminate neutron events from gamma-ray events, energy losses and straggling of each particle are used. The energy loss of proton is much larger than that of electrons. Furthermore, the straggling of the protons is also smaller than that of electrons. The discrimination power was tested using a gamma-ray source ($^{22}$Na). Annihilated back-to-back gamma-rays of 511keV were emitted from the source. One gamma-ray is detected by the $\mu$-TPC and another is detected by YAP scintillator and used as a trigger. The energy of gamma-ray is close to the $Q$ value (764keV) of the $^3$He(n, p)$^3$H reaction. The straggling of a track is characterized using $\chi^2$ defined by

$$\chi^2 = \sum_{i=1,2,n-1,n} \frac{\Delta_i}{\sigma}, \tag{9.5}$$

where $n$ is the number of detected points, $\delta_i$ is the distance between the $i$th detected point and the best-fit straight line, and $\sigma = 260\mu$m is the measured spatial resolution of the $\mu$-TPC. The degree of freedom (d.o.f) was three for all of the tracks, because we used the first two and the last two points to calculate $\chi^2$. Figs. 9.20 show the plots of $\chi^2$/d.o.f against d$E$/d$x$ for the events from $^{252}$Cf and the events from $^{22}$Na. We defined thresholds of neutron events for d$E$/d$x$ ($> 50$keV/cm) and $\chi^2$/d.o.f ($> 3$). More than 90% of gamma-ray events are rejected by this threshold.

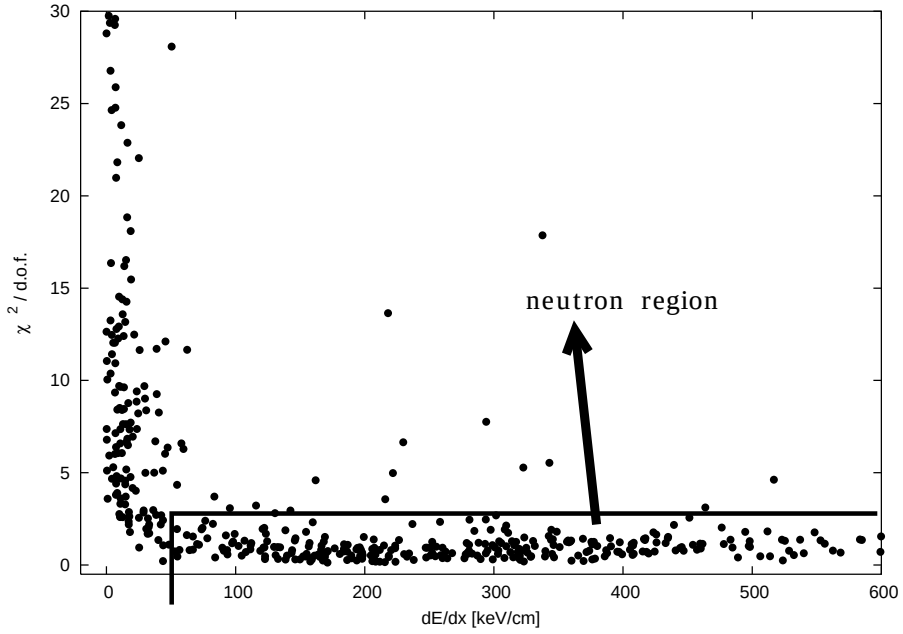


(a)

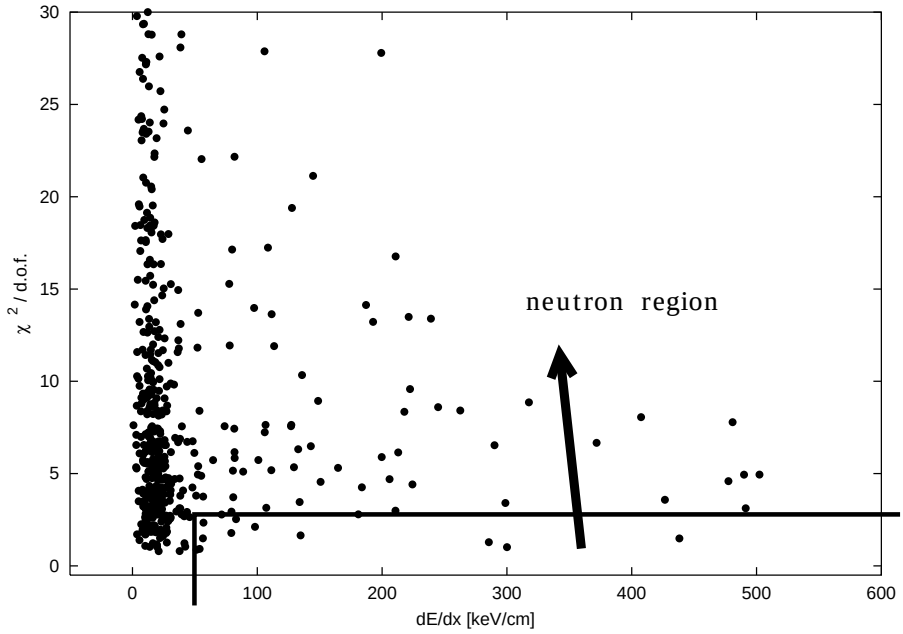


(b)

Figure 9.20: $\chi^2$/d.o.f vs. d$E$/d$x$ of the (a): $^{252}$Cf events, and (b): $^{22}$Na events. The neutron regions are superimposed.

# Chapter 10

# Summary and conclusion

A novel gaseous micro-pattern detector "Micro Pixel Chamber ($\mu$-PIC)" has been developed, and its performances have been examined. Because the $\mu$-PIC was manufactured based on the Printed Circuit Board (PCB) technology, it has the features of a large detection area ($10 \times 10\text{cm}^2$) and mechanical robustness.

From the early development using the small prototype detector having $3 \times 3\text{cm}^2$ detection area, the $\mu$-PIC indicated the promising abilities as a radiation detector. The gas gain exceeded 5000 and it also had a robustness for discharges. In addition, the PCB technology made it possible to produce a large two-dimensional $\mu$-PIC with a detection area of $10 \times 10\text{cm}^2$. Within one year we developed two type of $\mu$-PIC.

However, there have been serious problem for $\mu$-PICs to be overcome. That is the lower anode electrodes below the substrate. The effect of the lower anode was intensively investigated by the computer simulation study using MAXWELL and GARFIELD. This simulation study shows that the drift of primary electrons are prevented by the substrate edge near the anode top and 2/3 of primary electrons did not reach the anode but the surface of the substrate. It means that the gas gain would increase three times higher if the anode top is higher than the surface of the substrate. In Addition, we found that thicker substrate improves the absolute gas multiplication factor as well as the electron collection efficiency, because the thick substrate shield the electric field due to the anode readout buses placed on the rear side of the substrate. The attainable gas gain was estimated from the simulation and the previous experimental data. If the substrate thickness exceed

150$\mu$m, the attainable gas gain to avoid discharges would exceed $10^5$.

Based on this study, we have reproduced the higher anode electrodes using a new manufacturing technology. The new $\mu$-PIC have a 100$\mu$m thick substrate with higher and uniform anode electrodes. The gas gain of more than $1.5 \times 10^4$ was obtained for the new $\mu$-PIC. This new method also provided us the uniformity of the gas gain within 7% in the whole detection area of $10 \times 10\text{cm}^2$. Furthermore, a long term continuous operation over 1000 hours was achieved with the gas gain of more than 6000, which looks close to the required gas gain to detect Minimum Ionizing Particles. The attained gas gain was consistent with the simulation. It means that we can design the structure of $\mu$-PIC based on the quantitative prospect by the simulation. In near future, the $\mu$-PIC having the detection area of $30 \times 30\text{cm}^2$ will be completed based on this improved method.

A compact data acquisition (DAQ) system was developed for multi-channel and high-rate readout of $\mu$-PIC. It consists of five Field Programmable Gate Arrays (FPGAs) and operates with the clock of 20-40MHz. The maximum data acquisition rate of 7.1MHz was obtained using an X-ray generator.

The imaging performances of the $\mu$-PIC were examined using the DAQ system with the clock of 20MHz. As a result of X-ray imaging test, the position resolution of 120$\mu$m (r.m.s.) was obtained, which value is very close to the limitation determined by the electrode pitch. The uniformity of the image was within 6% for the whole detection area.

The $\mu$-PIC was applied to the TPC, which is named "$\mu$-TPC". The track of protons were successfully detected with the sampling pitch of 2.6mm at 20MHz. Recently the 1mm sampling has been obtained by a DAQ system with 50MHz clock. The three-dimensional tracking resolution was 260$\mu$m for $Ar/C_2H_6$ (90/10) gas mixture for each sampling points for 20MHz sampling.

In order to explore the capability of $\mu$-PIC for various science fields, we have carried out following preliminary experiments. At first, we measured X-ray polarization using Thomson scattering of a polyethylene block. The asymmetric parameter of 0.15 was observed for 10keV X-ray using neon-based gas [62]. X-ray crystallography using the Continuous Rotation Photograph method was also performed using a ylide crystal. One of the most important applications of the $\mu$-TPC is the gamma-ray imaging of MeV energy region. We have developed a prototype of the MeV gamma-ray imaging detector

based on the advanced Compton method. The first gamma-ray image was successfully obtained using two $^{137}$Cs (662keV) sources. The detail of MeV imaging was already published elsewhere [60, 61]. Another important application of the $\mu$-TPC is thermal neutron imaging. The detection principle was verified with $Ar/C_2H_6$ gas mixture and a $^{252}$Cf source [72].

As mentioned before simulation, $\mu$-PIC has a much potential to innovate gas gains by small improvements,and we will soon try to develop the new perfect radiation detector. The $\mu$-PIC will soon establish a new imaging method using X-ray, gamma-ray, charged particles, and neutrons.

# Bibliography


[1] A. Oed, Nucl. Instr. Meth. A **263** (1988) 351.

[2] A. Ochi, Ph.D thesis, Tokyo Institute of technology, 1998.

[3] A. Ochi, et al., Proc SPIE **3774** (1999) 76.

[4] B. Gebauer, et al., Nucl. Instr. Meth. A **409** 56.

[5] Y. Nishi, et al., Proc SPIE **3774** (1999) 87.

[6] T. Tanimori, et al., Nucl. Instr. Meth. A **436** (1999) 188.

[7] F. Sauli, Nucl. Instr. Meth. A **386** (1997) 531.

[8] F. Giomataris, et al., Nucl. Instr. Meth. A **376** (1996) 29.

[9] E. Nappi, Nucl. Instr. Meth. A **504** (2003) 70.

[10] B. Ketzer, Nucl. Instr. Meth. A **494** (2002) 142.

[11] B. Morgan, Nucl. Instr. Meth. A **513** (2003) 226.

[12] Y. Nishi, Ph.D thesis, Tokyo Institute of technology, 2000.

[13] D. Mörmann, et al., Nucl. Instr. Meth. A **504** (2003) 93.

[14] D. Mattern, et al., Nucl. Instr. Meth. A **300** (1991) 275.

[15] S. F. Biagi, et al., Nucl. Instr. Meth. A **366** (1995) 76.

[16] R. Bellazzini, et al., Nucl. Instr. Meth. A **424** (1999) 444.

[17] R. Bellazzini, et al., Nucl. Instr. Meth. A **423** (1999) 125.

[18] W. K. Pitts, et al., Nucl. Instr. Meth. A **438** (1999) 277.

[19] B. Adeva, et al., Nucl. Instr. Meth. A **435** (1999) 402.

[20] A. Ochi, et al., Nucl. Instr. Meth. A **471** (2001) 264.

[21] A. Ochi, et al., Nucl. Instr. Meth. A **478** (2002) 196.

[22] T. Nagayoshi, Master's thesis, Tokyo Institute of Technology, 2001.

[23] W. R. Leo, "Techniques for Nuclear and Particle Physics Experiment", Second Revised Edition, Springer-Verlag, Berlin, 1994.

[24] A. Peisert, et al., CERN Report 84-08 (1984).

[25] F. Sauli, CERN Report 77-09 (1977).

[26] H. A. Bethe, Phys. Rev. **89** (1953) 1256.

[27] G. R. Lynch, et al., Nucl. Instr. Meth. B **58** (1991) 6.

[28] S. F. Biagi, MAGBOLTZ, program to compute gas transport parameters, Version 2.2, CERN.

[29] A. Sharma, SLAC-Journal-ICFA **16** (1998) 3.

[30] G. Charpak, et al., Nucl. Instr. Meth. **62** (1968) 262.

[31] `http://gdd.web.cern.ch/GDD/`

[32] J. Benlloch, et al., Nucl. Instr. Meth. A **419** (1998) 410.

[33] H. Sakurai, et al., Nucl. Instr. Meth. A **374** (1996) 341.

[34] S. F. Biagi, et al., Nucl. Instr. Meth. A **392** (1997) 131.

[35] S. F. Biagi, et al., Nucl. Instr. Meth. A **323** (1992) 258.

[36] T. Tanimori, et al., Nucl. Instr. Meth. A **381** (1996) 280.

[37] O. Bouianov et al., in prep.

[38] A. Bressan, et al., Nucl. Instr. Meth. A **424** (1999) 321.

[39] L. W. Nordheim, Proc. Roy. Soc. Sci. (London) **A 121** (1928) 626.

[40] J. M. Howston, Phys. Rev. **88** (1952) 349.
R. E. Burgess, et al., Phys. Rev. **90** (1953) 515.

[41] O. Yamamoto, et al., IEEJ Trans. FM., **123** (2003) 370.

[42] J. Va'vra, Nucl. Instr. Meth. A **252** (1986) 547.

[43] L. Malter, Phys. Rev. **50** (1936) 48.

[44] K. Berkhan, et al., Nucl. Instr. Meth. A **515** (2003) 185.

[45] C. Iacobaeus, et al., IEEE Trans. Nucl. Sci. **49** (2002) 1622.

[46] T. Beckers, et al., Nucl. Instr. Meth. A **346** (1994) 95.

[47] T. Nagae, et al., Nucl. Instr. Meth. A **323** (1992) 236.

[48] O. Sasaki, et al., IEEE Trans. Nucl. Sci. **46** (1999) 1871.

[49] R. Orito, et al., to appear in IEEE Trans. Nucl. Sci.

[50] M. Ueno, Master's thesis, Kyoto University, 2002.

[51] Y. Amemiya, et al., Rev. Sci. Instrum. **66** (1995) 2290.

[52] H. Wagner, et al., physics/0310137.

[53] MAXWELL 3D Field Simulator, Ansoft Corporation,
`http://www.ansoft.com`

[54] R. Veenhof, Nucl. Instr. Meth. A **419** (1998) 726.

[55] S. H. Han, et al., IEEE Trans. Nucl. Sci. **47** (2000) 1416.

[56] Yu. N. Pestov et al., Nucl. Instr. Meth. A **338** (1994) 368.

[57] D. Fancher, et al., Nucl. Instr. Meth. **161** (1979) 383.

[58] P. Némethy et al., Nucl. Instr. Meth. **212** (1983) 273.

[59] F. Sauli, CERN-EP-TA1 Internal Report, (1999).

[60] R. Orito, et al., Nucl. Instr. Meth. A **513** (2003) 408.

[61] T. Tanimori, et al., Proceedings of Astronomy with Radioactivities IV and Filling the Sensitivity Gap in MeV Astronomy, Bavaria, Germany, May, 2003, submitted for New Astronomy.
R. Orito, et al., Proceedings of the International Conference on Imaging Techniques in Subatomic Physics, Astrophysics, Medicine, Biology and Industry (IMAGING2003), Stockholm, Sweden, July, 2003, submitted for Nucl. Instr. Meth. A.

[62] M. Ueno, et al., Proceedings of the International Conference on Imaging Techniques in Subatomic Physics, Astrophysics, Medicine, Biology and Industry (IMAGING2003), Stockholm, Sweden, July, 2003, submitted for Nucl. Instr. Meth. A.

[63] W. R. Nelson, et al., SLAC-265 (1985).

[64] W. C. Weisskopf et al., Astrophys. J. **208** (1976) L125.

[65] Y. Amemiya, et al., Nucl. Instr. Meth. A **266** (1988) 645.

[66] H. Toyokawa, et al., Nucl. Instr. Meth. A **467-468** (2001) 1144.

[67] A. Ochi, et al., Nucl. Instr. Meth. A **467-468** (2001) 1148.

[68] V. Schönfelder, et al., Astrophys. J. Suppl. **86** (1993) 657.

[69] J. D. Kurfess, et al., Proceedings of the 5th Compton Symposium, Portsmouth, New Hampshire, September 15-17, 1999.

[70] R. Orito, et al., Proceedings of "International School and mini-Workshop for Scintillating Crystals and their Applications in Particle and Nuclear Physics", KEK, Tsukuba, Japan, 17-18 ,November, 2003, in preparation.

[71] Carel W.E. van Eijk, Nucl. Instr. Meth. A **477** (2002) 383.

[72] K. Miuchi, et al., Nucl. Instr. Meth. A, in press.

# Acknowledgments

I am deeply grateful to Professor Toru Tanimori for his guidance and encouragements in this work. This thesis would not be completed without his support. I would like to thank my collaborators: Professor Takeshi Tsuru, Dr. Hidetoshi Kubo, Dr. Kentaro Miuchi, Dr. Atsushi Takeda, Masaru Ueno, Reiko Orito, Yoko Okada, Atsushi Takada (Kyoto Univ.), Dr. Oleg Bouianov (Espoo-Vantaa Institute of technology) and Dr. Marina Bouianov (CSC-Scientific Computing Ltd.). I am grateful for all the member of the cosmic ray laboratory in Kyoto University for their continuous discussions and encouragements.

I sincerely thank Dr. Atsuhiko Ochi (Kobe Univ.) and Yasuro Nishi (Rigaku) for the helpful advice of the development of the detector and the DAQ system. I also thank Dr. Yuji Nishi (RIKEN) for his kind guidance of detector physics. I appreciate Tomohisa Motomura (D.T. Circuit Technology Co., Ltd.), Dr. Akira Yunoki (TOSHIBA), and the staffs of D.T. Circuit Technology and TOSHIBA who manufactured the detectors and gave me several technical informations about the manufacturing process.

I thank Professor Tomofumi Nagae (KEK) and members of his laboratory, who helped the experiment at T1 beam line in the Proton Synchrotron at KEK. I also thank Dr. Hidenori Toyokawa, Dr. Masayo Suzuki (JASRI), and Dr. Tetsuro Fujisawa (RIKEN), who helped the MSGC experiment at SPring-8. I appreciate Professor Yuji Ohashi and Professor Hidehiro Uekusa (Tokyo Inst. of Tech.) for providing the experimental space.

This work was supported by a Grand-in-Aid for the 21st Century COE "Center for Diversity and Universality in Physics", and the Japan Society for Promotion of Science for Young Scientists.

Finally, I thank my family for their kind support and encouragement.